2007

# Study of a compact energy absorber

Muhammad Ali
*Iowa State University*

# Study of a compact energy absorber

by

Muhammad Ali

A dissertation submitted to the graduate faculty

in partial fulfillment of the requirements for the degree of

DOCTOR OF PHILOSOPHY

Major: Mechanical Engineering

Program of Study Committee
Abir Qamhiyah, Co – major Professor
Donald Flugrad, Co – major Professor
Greg Luecke, Co – major Professor
Carolyn Heising
Gloria Starns

Iowa State University
Ames, Iowa
2007

DEDICATION

Dedicated to my father **Muhammad Murtaza**

All I know and all I have

Is by the making of his hand

To the memory of my grand father **Muhammad Rasool**

To my Mother for her loving guidance and sacrifice

and

To my Family for their endless love and support

# TABLE OF CONTENTS

LIST OF FIGURES ……... vii

LIST OF TABLES …… xii

ACKNOWLEDGEMENTS …….. xiii

ABSTRACT …….. xv

CHAPTER 1 INTRODUCTION……..... 1

1.1 Characteristics of an energy absorber…….. 1

1.1.1 Irreversible energy conversion…….. 1

1.1.2 Restricted and constant reactive force……... 2

1.1.3 Long stroke…… 3

1.1.4 Stable and repeatable deformation mode…….. 4

1.1.5 Light weight and high specific energy absorption capacity….. 4

1.1.6 Cost effective and easy installation……... 5

1.2 Idealized material models…… 5

1.3 Effect of large deformation……. 7

1.4 Dynamic effects……... 7

1.4.1 Stress wave propagation and its effects on energy absorption.. 8

1.4.2 Strain rate effects……... 12

CHAPTER 2 HYPOTHESIS……... 13

2.1 Energy absorbing issues and nature ……... 13

2.2 Banana cross-section……... 15

CHAPTER 3 FINITE ELEMENT ANALYSIS……... 18

3.1 Background...……..... 18

3.2 Modeling……. 19

3.3 Analysis……...…… 20

3.4 Results……. 21

3.4.1 Energy……... 26

3.4.2 Simulations…… 27

CHAPTER 4 THEORETICAL ANALYSIS……..……. 33

4.1 The mechanics of honeycombs....……... 34

4.1.1 Upper bound collapse stress……..... 36

4.1.2 Lower bound collapse stress…….. 37

4.1.3 Locking strain ……... 38

4.2 Finite element analysis of GHS…...…… 40

4.2.1 Modeling……... 40

4.2.2 Results……... 41

CHAPTER 5 STUDY OF GRADED HONEYCOMB STRUCTURES (GHS) 44

UNDER IMPACT…….....

5.1 Deformation modes of GHS under dynamic loading…….. 45

5.2 Stress strain curve…….……... 45

5.3 GHS modes under high loading rates…….. 47

5.4 Stress strain curves for high impact velocity……... 50

5.5 Mathematical model for high velocity impact……. 52

5.6 Energy absorption performance of GHS w.r.t regular honeycombs…….. 59

5.7 Cell shape……..... 65

CHAPTER 6 CONCLUSIONS AND FUTURE WORK...…… 67

6.2 Conclusions……. 67

6.1 Future Work ……. 69

APPENDIX A ……..…… 70

A.1 Classical theory of plasticity ……. 70

APPENDIX B……... 75

B.1 Propagation velocity……... 75

B.2 Particle velocity…….. 77

APPENDIX C...…… 78

C.1 Effect of size on stiffness…… 78

C.2 MATLAB Code…….. 80

APPENDIX D…….. 91

D.1 Explicit method…….. 91

D.2 Central difference method…….. 91

APPENDIX E……... 94

E.1 Contact pair……. 94

E.2 Constraint enforcement method…….. 95

E.2.1 Kinematic contact constraints……... 95

E.2.2 Penalty contact constraints…… 96

APPENDIX F……..... 98

F.1 C38DR Element…….. 115

APPENDIX G…….. 100

G.1 Young's modulus of hexagonal honeycombs……. 100

G.2 Shear modulus of hexagonal honeycombs……. 102

REFERENCES…… 105

# LIST OF FIGURES


| | | |
|---|---|---|
| Figure 1.1 | Uniaxial true stress-strain curve …..……. | 3 |
| Figure 1.2 | Impact response of an object from two different materials...…… | 4 |
| Figure 1.3 | Idealized stress-strain curves of elastic materials under tension ...……... | 6 |
| Figure 1.4 | Idealized stress-strain curves of rigid materials under tension ……..… | 6 |
| Figure 1.5 | Stress waves in decreasingly strain hardening materials ……...……... | 9 |
| Figure 1.6 | Stress waves in increasingly strain hardening materials ……... | 9 |
| Figure 2.1 | The cellular structure in a human femur ……..... | 13 |
| Figure 2.2 | The compressive response of cellular structure in human femur ……... | 14 |
| Figure 2.3 | The stress-strain curves of wood under compression …….…… | 14 |
| Figure 2.4 | The compressive behavior of plastic and elastomeric honeycombs ...….. | 15 |
| Figure 2.5 | Cross section of a banana peel……..……. | 16 |
| Figure 3.1 | Rigid plate hitting the solid aluminum plate……..…….……... | 19 |
| Figure 3.2 | Replication of cell shape from a banana peel ……...… | 20 |
| Figure 3.3 | Aluminum with different cell packing……... | 21 |
| Figure 3.4 | Dynamic Force-Displacement curve of a honeycomb structure……... | 22 |
| Figure 3.5 | Force-Displacement curves at 3 m/s impact velocity…… | 22 |
| Figure 3.6 | Energy-Displacement curves at 3 m/s impact velocity ……. | 23 |
| Figure 3.7 | Deformed solid plate at the end of the stroke ..……..... | 29 |
| Figure 3.8 | Deformed plate containing one layer of cells, at the end of the stroke .. | 29 |
| Figure 3.9 | Deformed plate containing two layers of cells, at the end of the stroke. | 29 |

Figure 3.10 Deformed plate containing two graded layers of cells, at the end of the stroke ……. 30

Figure 3.11 Deformed plate containing three layers of cells, at the end of the stroke.. 30

Figure 3.12 Deformed plate containing three graded layers of cells, at the end of the stroke……..... 30

Figure 3.13 Deformed plate containing modified design 1 structure, at the end of the stroke…….. 31

Figure 3.14 Deformed plate containing modified design 2 structure, at the end of the stroke…….. 31

Figure 3.15 Deformed plate containing modified design 3 structure, at the end of the stroke…….. 31

Figure 3.16 Deformed plate containing modified design 4 structure, at the end of the stroke ……. 32

Figure 3.17 Model containing cells filled with crushable foam....…… 32

Figure 3.18 Composite graded section…….. 32

Figure 4.1 The regular two dimensional honeycomb structure ...……... 33

Figure 4.2 A unit cell of a regular honeycomb…… 35

Figure 4.3 Plastic collapse of inclined walls in the Y direction……..... 37

Figure 4.4 Internal and external bending moment on the inclined wall……..... 38

Figure 4.5 The modified peel structure……... 39

Figure 4.6 The theoretical response of the GHS in the Y direction using equation 4.10.…… 40

| | | |
|---|---|---|
| Figure 4.7 | The shell model of graded honeycomb structure (GHS)……..... | 41 |
| Figure 4.8 | The superimposed theoretical and finite element output …….. | 42 |
| Figure 4.9 | The comparison of the theoretical and modified theoretical response of GHS with respect to the finite element analysis ……... | 43 |
| Figure 5.1 | Deformation of the GHS in the end of the dynamic analysis…… | 46 |
| Figure 5.2 | Dynamic stress-strain response of the GHS in the Y direction at different impact velocities.……. | 47 |
| Figure 5.3 | Deformation of the GHS at 30 m/s impact velocity…….. | 48 |
| Figure 5.4 | Deformation of the GHS at 60 m/s impact velocity…….. | 48 |
| Figure 5.5 | Deformation of the GHS at 100 m/s impact velocity ……... | 49 |
| Figure 5.6 | The stress-strain response of the GHS at 30, 60, and 100 m/s impact velocity ……...……... | 50 |
| Figure 5.7 | Propagation of precursor elastic and successor plastic wave……. | 51 |
| Figure 5.8 | Typical stress-strain curve which is idealized into rigid, perfectly plastic, behavior followed by complete locking…… | 53 |
| Figure 5.9 | Sketch of a mass M impacting an initially stationary GHS……... | 54 |
| Figure 5.10 | Comparison between theory and FE analysis at 30 m/s impact velocity... | 56 |
| Figure 5.11 | Comparison between theory and FE analysis at 60 m/s impact velocity... | 56 |
| Figure 5.12 | Comparison between theory and FE analysis at 100 m/s impact velocity. | 57 |
| Figure 5.13 | Comparison between theory and FE analysis at 200 m/s impact velocity. | 57 |
| Figure 5.14 | Comparison between theory and FE analysis at 340 m/s impact velocity. | 57 |

Figure 5.15 Total energy absorbed by the GHS at different impact velocities……. 28

Figure 5.16 Comparison of the dynamic response of GHS and RHS in the Y direction……. 59

Figure 5.17 Energy curves of RHS at 1 m/s impact velocity ……... 62

Figure 5.18 Energy curves of GHS at 1 m/s impact velocity…… 62

Figure 5.19 Velocity variation of the rigid plate 'A' in deforming the GHS and the RHS ……... 63

Figure 5.20 Utilization of stroke for different impact velocities…….. 64

Figure 5.21 Stress on the rigid plate, A, of the GHS …… 65

Figure 5.22 Transformation of the hexagonal honeycomb cell shape into a banana peel cell shape…… 66

Figure 5.23 Variation of the plateau stress for different wall thickness with the wall angle……... 66

Figure 5.24 Variation of the locking strain for different wall thickness with the wall angle……..... 66

Figure A.1 Uniaxial true stress-strain curve ……..... 73

Figure B.1 Propagation of a stress wave in a solid bar ……..…. 75

Figure B.2 Stress wavefront causing particle velocity increment…… 77

Figure C.1 Variation of cell stiffness w.r.t. cell size…… 79

Figure C.2 $10^{th}$ order polynomial approximating stiffness vs. size curve …….. 79

Figure C.3 Variation in nodal displacement w.r.t. cell size ……..….. 80

Figure C.4 Cell stiffness within permissible cell size range ……..….. 80

Figure E.1 Methodology of finding the contact node on the slave surface……. 94

Figure F.1 C3D8R Element……. 98

Figure F.2 Deformation (dashed lines) in element but the integration point (cross) is not moving……..... 98

Figure G.1 Unit cell under compression in the Y direction.……..... 100

Figure G.2 Forces and bending moments on inclined walls…… 101

Figure G.3 Unit cell loaded in shear …… 103

Figure G.4 Forces acting on point B ……... 103

# LIST OF TABLES

Table 3.1 Maximum force and percentage reduction in contact force at different velocities. …… 25

Table 3.2 Energy comparison of structures at different velocities…….. 28

Table 5.1 Rebound velocity and plastic energy of the RHS and the GHS for different impact velocities……... 64

## ACKNOWLEDGEMENTS

My utmost thanks should go to ALLAH for His guidance and love for me throughout my life. I am indebted to many individuals for their assistance during my doctoral studies. First of all, I would like to express my deep appreciation and gratitude to Professor Abir Qamhiyah. As my adviser, she provided me constant encouragement, insightful comments, and invaluable suggestions that benefited me not only on the completion of this thesis, but also my professional career in a long time to come. Professor Abir always inspired me from her exotic dimensions of thinking and acute sense of exploring and seeking research solutions. Her paramount benevolence during tough times of my personal life is a reflection of her unconditional care for students. Her efforts to accomplish this research work in few occasions were beyond the call of duty. Professor Abir is one of the best advisers I have had pleasure and honor to work with during my six years of graduate studies.

I would like to take this opportunity to extend my special acknowledgement to my co – mentors Professor Don Flugrad and Professor Greg Luecke. Their continuous guidance and tireless assistance made this project a success. I am indebted to my committee members, Dr. Bruce Thomson, Dr. Carolyn Heising, and Dr. Gloria Starns who provided extensive personal and professional guidance and taught me a great deal about both scientific research and life in general. I would, in particular, appreciate Dr. Gloria Starns for her precious help and indispensable contributions in reviewing research papers. Despite her tight schedule she made herself available and assisted me in editing, formatting and improving grammar of papers. Also, I would like to offer my gratitude to the staff members of Mechanical Engineering Department and Graduate College for providing me the facilities and resources

during the research, especially John Dickerson and Hap Steed for keeping ABAQUS running in Hoover Linux lab.

In the last but not least I acknowledge my gratefulness to my family who endured this long process with me, always offering sheer support and love. I am indebted to my parents for everything they have given to me. They have stood by me in everything I have done so far, providing constant support, encouragement, and love.

# ABSTRACT

Deformable energy absorbers play a vital role in crash protection systems. However, prevailing stringent design requirements to mitigate impact damage in a limited space have advocated a need for superior energy absorbing materials and versatile and compact structures. In this thesis, an intelligent compact energy absorbing structure is presented that alleviates the impact by distributing load over finite displacement (stroke). The structure's geometry is observed in the cross-section of a banana peel that has a specific graded cellular packing in a confined space. This packing enables the thin peel to protect the internal soft core from external impact loads. The cellular pattern observed in a banana peel is used to construct a finite element analysis model of the structure. The energy absorbing characteristics of the structure are evaluated and compared to the energy absorbing characteristics of a solid section by means of finite element simulations using ABAQUS. The structure was found to reduce the static and dynamic reactive forces up to 83 percent in comparison to a solid section provided the thickness and contact area are kept constant. The energy absorbing characteristics of peel structure were also compared to regular hexagonally shaped cellular honeycombs. The peel structure resulted in lower impacts and severity of deceleration-acceleration phase over regular honeycombs for higher velocity range under the same space/stroke constraints. Analytical models for low and high impact velocities were also developed to calculate the crushing strength and stroke of the graded structure.

# CHAPTER 1. INTRODUCTION

Energy absorbers are devices that convert kinetic energy into another form (e.g. pressure energy in fluids, elastic energy in solids, and plastics energy in deformable solids). The main purpose is to reduce the impact load by disturbing the load over a finite time period.

## 1.1. Characteristics of an energy absorber

The general characteristics of an energy absorber can be outlined as follows

### *1.1.1. Irreversible energy conversion*

The irreversible energy conversion is a function of plastic strain. When load is applied, the structure undergoes deformation. If the load is lower than the yield strength of the material, the structure would restore its original shape after the removal of load. Otherwise the structure would undergo elasto-plastic deformation. Figure 1.1 shows a typical uniaxial true stress-strain curve of the material having a pronounced yield point. OABC is a loading and CD is an unloading path. The total strain of the material is OE ($\varepsilon$) which is a sum of elastic strain DE ($\varepsilon_e$) and plastic strain OD ($\varepsilon_P$). Classic theory of plasticity (Appendix A) explains that the plastic deformation is associated with the irreversible energy dissipation. In Figure 1.1, the total energy density (energy per unit volume) stored by the material is represented by the shaded area; where area OABCD represents the permanent energy and the triangle CDE represents the recovered energy density. Sometimes, the elastic portion of the dissipated energy is not fully recoverable, that portion is called the entrapped elastic energy. The energy dissipated in elastic deformation dictates how much an object would rebound

from the structure. The higher the elastic energy, the greater the rebound and vice versa. High rebound imparts more damage to the impacting object or structure. Figure 1.2 shows a rebound of an object from two different materials with the same initial conditions. Curve 'A' shows an object experiencing higher retardation followed by higher rebound acceleration. On the other hand, curve 'B' shows a gentle arresting force and the rebound. If the total energy remains constant, increasing plastic energy fraction results in lower rebound. Entrapped elastic energy also contributes to reducing the rebound.

*1.1.2. Restricted and constant reactive force*

While providing the energy-absorption capacity during a large deformation process, the maximum value of the reaction force must be kept below the value that could cause damage or injury [1]. Reaction force should be kept constant to avoid an excessively high rate of retardation. By the method of variation it can be proved that the Gadd severity index (GSI) is a minimum if the force is constant. GSI was first presented by Charles Gasdd in 1966 for use in the automobile industry. By correlating duration of impact and retardation upon impact, he was able to develop an expression that could describe the onset of head injury. He called that index of survivability as GSI. Numerically, GSI is defined as

$$I = \int a^{2.5} dt \tag{1.1}$$

The index (I) is a function of retardation upon impact (a) and the time of deceleration (t). The exponent is based upon the experimental work. In his original paper, Gadd suggested a value of 2.5. I = 1000 was considered as the threshold for serious/fatal head injury; any number higher than that would result in a loss of life [2].

*1.1.3. Long stroke*

Dissipation of kinetic energy is as important factor as impact force (F) in analyzing crashworthy situations. For a given amount of kinetic energy, the longer the time, the smaller is the force. This leads to a notion of 'buying distance at the cost of time'. For a constant force, the distance required to bring an object, moving with velocity 'v', to zero is vt/2, and it is this distance the force travels to dissipate the damaging kinetic energy.

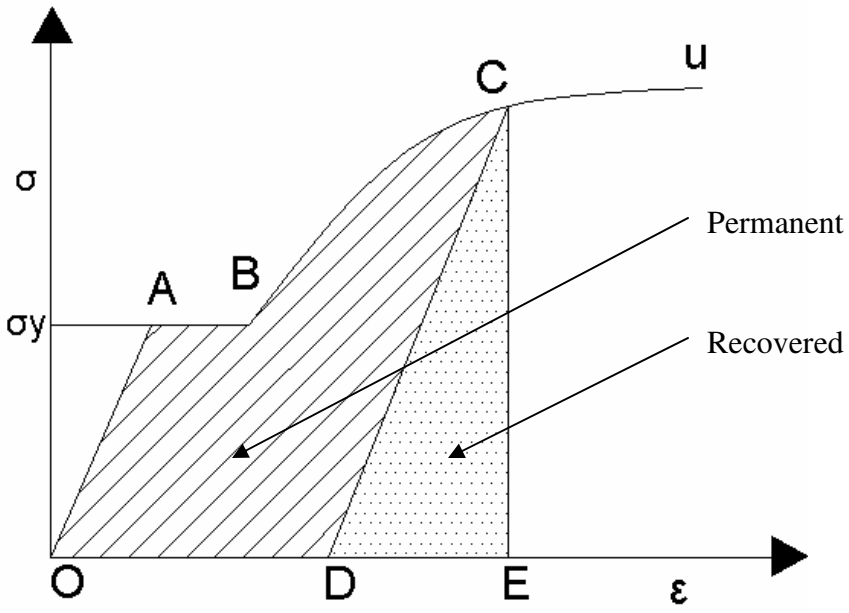


Figure 1.1: Uniaxial true stress-strain curve

In selection of energy-absorbing materials, the ratio of stroke to overall original dimension of materials is very important. Solid materials or structures cannot achieve high values of Δ/L, where 'Δ' is the stroke and 'L' is the original thickness of the material or the structure. The cellular materials/structures, because of being porous, are good in giving high 'Δ/L' ratio

The design of energy absorbers can either be load limited or stroke limited based upon the overall structure and the direction of impact. For example, in the case of tubes (provided the length to diameter ratio is greater than 1), the design is load limited in the axial loading direction and stroke limited in the transverse loading direction.

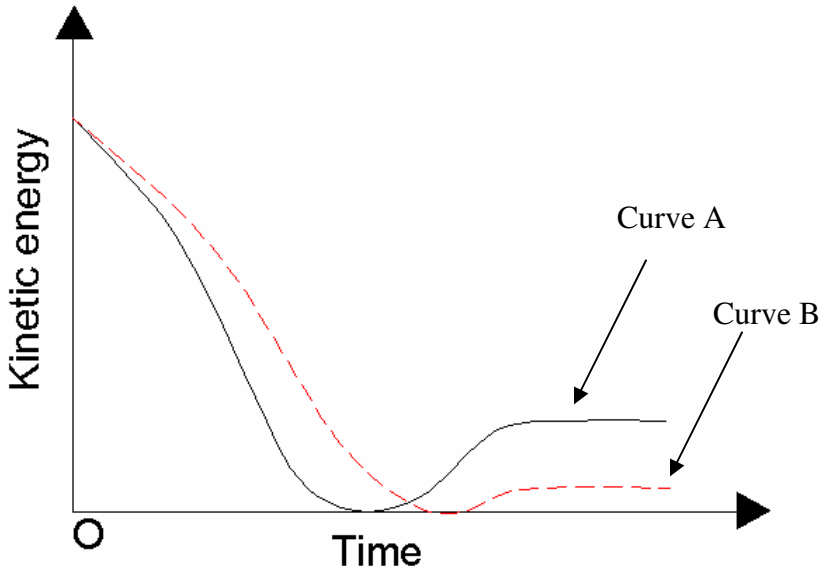


Figure1.2: Impact response of an object from two different materials

*1.1.4. Stable and repeatable deformation mode*

Deformation modes of an energy absorber should be stable, repeatable, and insensitive to the variations in the load magnitude, pulse shape, direction and distribution. [2]

*1.1.5. Light weight and high specific energy absorption capacity*

A structure having high specific energy absorption capacity (i.e., energy absorbed per unit weight) when used in the automobile industry would reduce the fuel consumption. Users would like to buy light helmets with the same or better safety features. The cellular structures provide an edge over solid materials by absorbing a considerably higher amount of energy

per unit weight. Therefore, with slightly lower stiffness and strength, the cellular structures are mostly better in per unit weight terms with respect to their base materials [2].

*1.1.6. Cost effective and easy installation*

The manufacturing, installation and maintenance of an energy absorber should be easy and inexpensive. This is an important factor in the sense that energy absorbers are mostly one- shot devices i.e., if they are deformed, they have to be replaced.

## 1.2. Idealized material models

Materials used to analyze the capacities of energy-absorbers, are divided into three models:

1) Elastic, perfectly plastic material model,
2) Elastic, linear hardening material model (also referred to as bilinear material model), and
3) Elastic, power hardening material model.

Figure 1.3 depicts these models. The tensile test gives a better prediction of which model describes the behavior of the given material in the real world. For example, mild steel shows a distinct yield point and after that its yield strength stays the same for some elasto-plastic deformation. Therefore, an elastic perfectly plastic material model can be used to analyze the behavior of the material for a certain range of stress/strains [3]. On the other hand, if aluminum is the material under consideration, no pronounced yield point is observed and the stress required to yield the material would continue to increase with the strain. This phenomenon is termed as strain hardening. In that situation, either elastic, linear hardening or

elastic, power hardening material models can be used to describe the behavior of the material in an analysis.

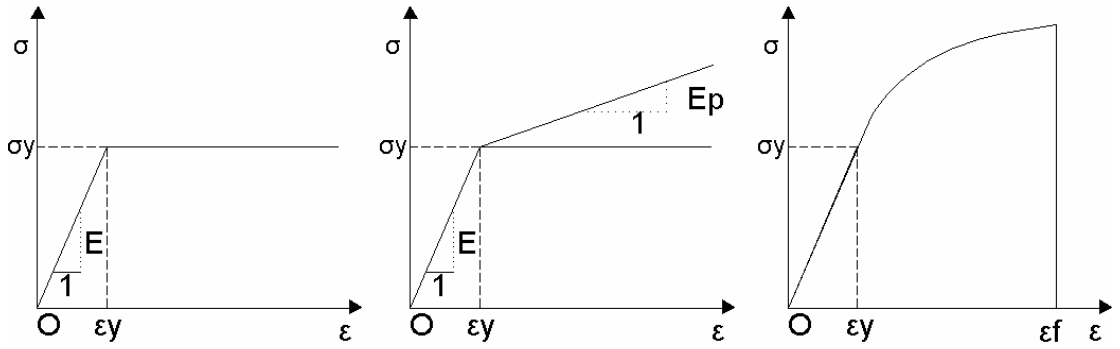


(a) (b) (c)

Figure 1.3: Idealized stress-strain curves of elastic materials under tension: (a) elastic, perfectly plastic; (b) elastic, linear hardening; and (c) elastic, power hardening

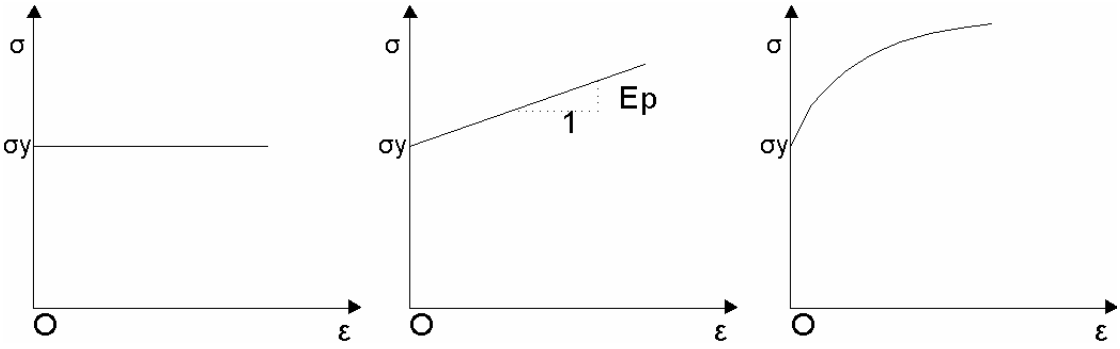


(a) (b) (c)

Figure 1.4: Idealized stress-strain curves of rigid materials under tension: (a) rigid, perfectly plastic; (b) rigid, linear hardening; and (c) rigid, power hardening

When used for energy absorption purposes, materials, structural components and devices undergo large plastic deformation. In that case, elastic strain is very small as compared to the plastic strain and assumed to be zero. Under this scenario, the material models described above are changed into:

1) Rigid, perfectly plastic material model,
2) Rigid, linear hardening material model,
3) Rigid, power hardening material model.

In these models, the elastic modulus is assumed infinity, and the materials behave rigidly before yielding. Figure 1.4 shows the rigid material models.

### 1.3. Effect of large deformation

Since the energy-absorbing structures undergo large deformation, the collapse load and 'collapse mechanism' is very different from what is expected from the limit analysis and the bound theorems where the deformation is assumed to be small.

Hence, while analyzing energy-absorption structures, all the geometric relationships and the equation of equilibrium should be formulated from the current (instantaneous) configuration rather than the original (unreformed) configuration. The point of application and direction of the load may also vary with the large deformation process and must be taken into account. The effect of moving plastic hinges and the axial forces in structural members should be considered too.

### 1.4 Dynamic effects

Dynamic effects can change the quasi-static response of an energy absorbing structure drastically. Thus, impact absorbers should be carefully analyzed in terms of the dynamic effects.

### 1.4.1 Stress wave propagation and its effects on energy absorption

When load is suddenly applied on a structure (having length much longer than the width), a stress wave is developed that travels away from the point of application of load. If the value of the normal applied stress is lower than the yield strength of the material, an elastic wave is generated and propagates at a speed of

$$C_L = \sqrt{\frac{E}{\rho}} \tag{1.2}$$

where '$C_L$' denotes the speed of the longitudinal elastic stress wave, while '$E$' and '$\rho$' are the Young's modulus of elasticity and the density of the material respectively (Appendix B). The particle velocity which is far less than the wave propagation velocity is

$$v = \frac{\sigma}{\sqrt{E\rho}} \tag{1.3}$$

where '$v$' is the particle velocity and '$\sigma$' is the intensity of the stress wave.

The relationship between the propagating stress wave and the particle velocity can be expressed as

$$\sigma = \sqrt{E\rho}v = \rho C_L v = \frac{E}{C_L}v \tag{1.4}$$

where, the ratio 'σ/v', is called the stress wave impedance. Therefore, a yield velocity can be expressed as a function of a material's properties as follows

$$v_y = \frac{Y}{\sqrt{E\rho}} = \frac{Y}{\rho C_L} = \frac{Y}{E}C_L \tag{1.5}$$

When particle velocity under impact loading is lower than the yield velocity, the stress generated in the structure is elastic.

If normal applied stress is higher than the yield strength of the material, then in addition to an elastic wave propagating with velocity '$C_L$' a plastic stress wave is initiated. The velocity of the plastic stress wave propagation depends upon the material's tangent modulus/plastic modulus.

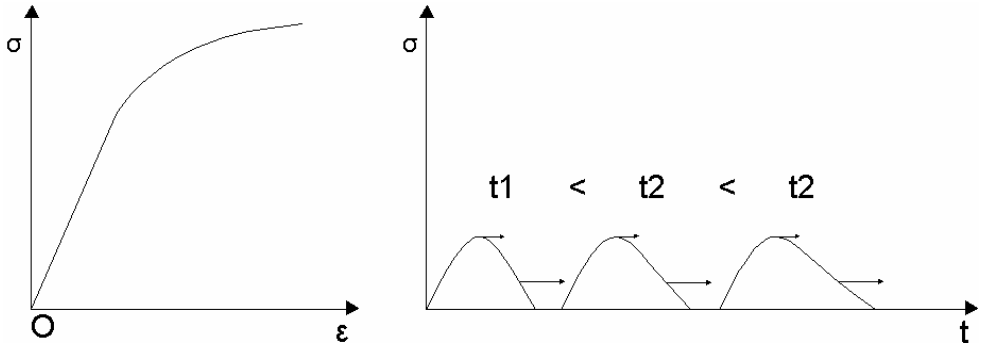


(a) (b)

Figure 1.5: Stress waves in decreasingly strain hardening materials: (a) the tangential modulus reduces with increasing strain; (b) change in wave shape during propagation

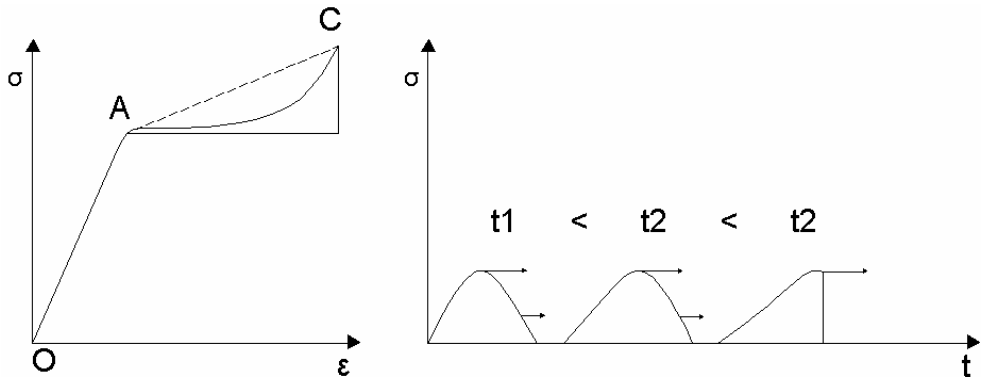


(a) (b)

Figure 1.6: Stress waves in increasingly strain hardening materials: (a) the tangential modulus increases with increasing strain; (b) The change in wave shape during propagation

If the material displays linear strain hardening behavior as shown in Figure 1.3, then the longitudinal plastic wave will propagate with the speed of

$$C_p = \sqrt{\frac{E_p}{\rho}} \tag{1.6}$$

where '$E_P$' is the stiffness modulus in the plastic region. Generally '$E_p$' is lower than '$E$' which means that the plastic wave travels slower than the elastic wave.

For strain hardening materials obeying a stress-stain relation, '$\sigma = \sigma(\varepsilon)$', in the plastic region, the propagation velocity is expressed as

$$C_p = \sqrt{\frac{d\sigma / d\varepsilon}{\rho}} \tag{1.7}$$

where '$d\sigma/d\varepsilon$' represents the instantaneous tangential modulus of the material. If the tangent modulus is decreasing with the increasing strain, the longitudinal plastic wave that brings about a higher stress will travel with a lower speed. As a result, the plastic wave will be scattered as shown in Figure 1.5.

For increasing strain hardening materials, the longitudinal plastic wave propagates faster than the elastic wave. Consequently, the plastic wave front is convergent and forms a shock wave as shown in Figure 1.6.

The elastic and the plastic wave may affect the energy absorption of the materials in many complex ways, depending upon the dynamic loading, configuration of the structure and the material properties. Below are some examples:

- Upon the application of a dynamic load on a structure, the stress brought about by the strong compressive plastic waves may cause a local plastic collapse at the loading end. For example, when the honeycomb structure undergoes dynamic loading, after a

certain value of impact velocity, the plastic collapse commences from the loading end. The minimum value of velocity at which honeycomb structures start behaving in that manner (the plastic collapse at the loading end) is called the critical velocity.

- When a compressive elastic wave reaches the distal end, it will reflect from the surface. If the surface is free, the reflected wave will be tensile which will propagate back from the free end. If the material is brittle, some portion of the material will tear off because brittle materials are usually weaker in tension than in compression. The tearing of material from the distal end is called spalling. The torn material will take a considerable amount of input energy away in the form of kinetic energy.
- When a compressive elastic wave reaches a fixed distal surface, the reflected wave is also compressive and this reflection doubles the stress magnitude that may cause some portion of the stress wave to be plastic. Consequently, plastic collapse will start at the distal end. In cellular structures, cells may plastically collapse first at the fixed distal end.
- When a compressive elastic wave reaches an interface between two different materials (e.g., honeycomb and casing), then some portion of the wave is reflected, and the rest is transmitted to the other material. The intensity of the reflected and the transmitted waves depends on the stiffness moduli of materials at the interface. The change in the cross-sectional area also affects the transmission and reflection of the stress waves. In fact, bulletproof windows made of laminated composites use the reflection/ transmission properties to reduce or eliminate spalling. In such a structure, wave propagation could be very complex, and X, T diagrams are constructed to portray the position and intensity of waves at any time interval [4].

### 1.4.2 Strain rate effects

The application of a 'rapidly varying dynamic load' causes a structure to deform rapidly, resulting in high strain rates. Materials like mild steels and some polymers exhibit very high dynamic yield strength and high strain rates with a reduction in ductility. The increase in yield strength affects the energy absorption capacity.

Cowper and Symonds presented a relationship among the dynamic yield strength *($Y^d$),* the static yield strength *(Y)* and the strain rate ( $\dot{\varepsilon}$ ) as

$$\frac{Y^d}{Y} = 1 + \left(\frac{\dot{\varepsilon}}{B}\right)^{1/q} \qquad \dot{\varepsilon} > 0 \tag{1.8}$$

where '*B*' represents the value of strain rate at which $Y^d = 2Y$, and $q$ is a material rate sensitivity. Cowper and Symonds relations are widely used in structural impact problems.

# CHAPTER 2. HYPOTHESIS

## 2.1 Energy absorbing issues and nature

Many examples have been discovered where nature is addressing energy absorbing issues e.g., the presence of the cellular structure in a human femur (a cancellous bone) assists in reducing bearing stresses and impact at the joint [5]. Figure 2.1 depicts the cross section of a human femur.

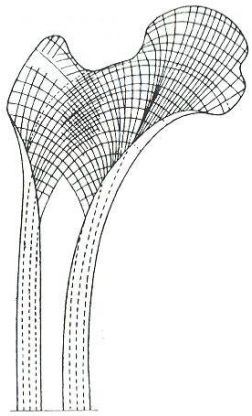

Figure 2.1: The cellular structure in a human femur

When two surfaces come in contact, the cellular structure undergoes a gross deformation, and the overall effect is a larger contact area, lower contact stresses and, consequently, low impact. Figure 2.2 shows the mechanical behavior of a human femur when it is subjected to a compressive load. The load is limited by the row wise collapse of the cellular structure. Furthermore, the plastic collapse load increases with the 'relative density'.

The cellular structure of wood has excellent energy absorbing properties in axial, radial and tangential directions [6] as shown by the stress-strain curves in Figure 2.3. Cork is

a classical example that has been in use in shoe-making industries for a long time to make impact proof soles.

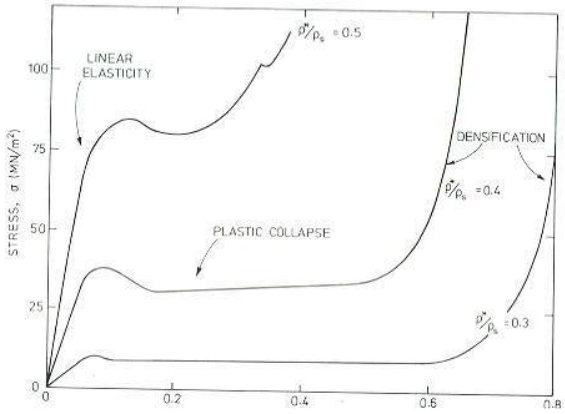


Figure 2.2: The compressive response of cellular structure in human femur [40]

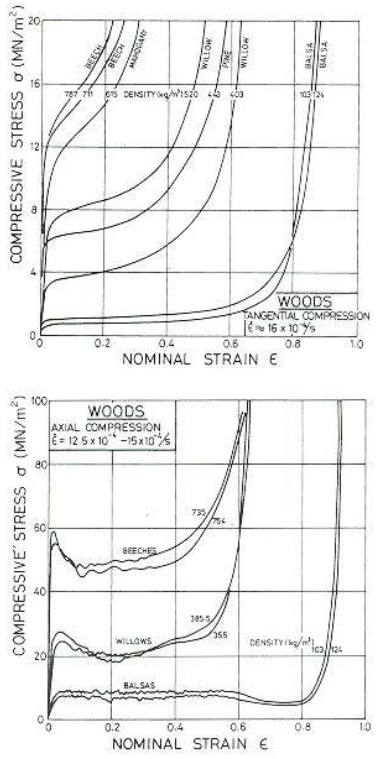


Figure 2.3: The stress-strain curves of wood under compression [40]

The structures replicated from honeycombs are one of the prime candidates for reducing the impact in automobile, aerospace and packaging industries [7]. The behavior of honeycombs made of different material is schematically explained in Figure 2.4. It may be noted that in compression, honeycombs show a typical energy absorbing curve that consists of an elastic, plateau and densification regimes.

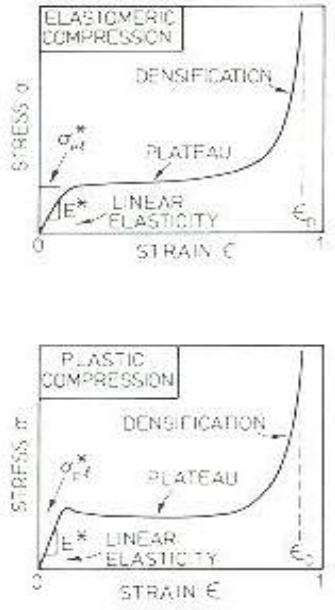


Figure 2.4: The compressive behavior of plastic and elastomeric honeycombs [40]

**2.1 Banana cross-section**

Figure 2.5 shows the cross sections of different banana peels. In technical terms, such kinds of materials are called Functionally Graded Materials (FGM). In FGM, the composition and structure gradually vary with depth, resulting in corresponding changes in the properties of the material. Observations show that such types of functionally graded structures are highly adaptive to all boundary and loading conditions defined by their environment. For example, the interior structure of a bone has an optimized shape with

respect to the direction of principal stress and the magnitude of shear stress [8]. The structure found in bamboo gives a high strength to weight ratio [5]. Studies have shown that these biological systems have a sensing mechanism (e.g. piezoelectric effects in bone) that allows them to undergo modeling and remodeling to adopt the most favorable structure that meets all the functional requirements under intense environment and energy conditions [9-12]. In a banana peel, one of the main objectives is to protect the internal soft core from external impacts.

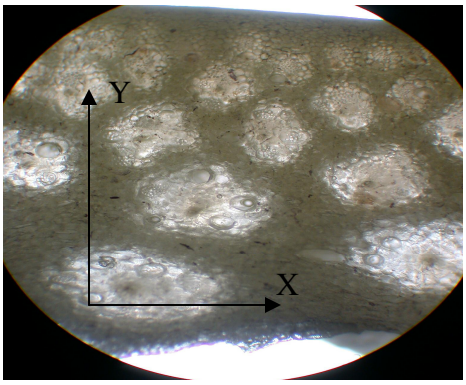


(a)

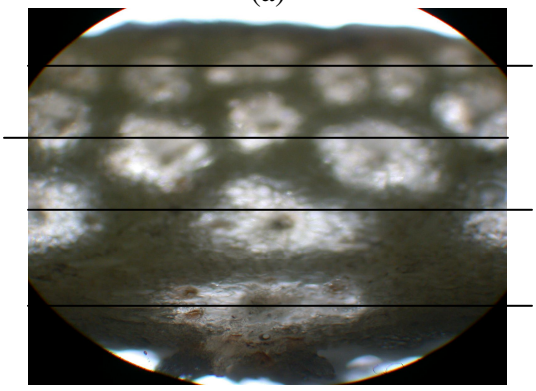

(b)

Figure 2.5: Cross section of a banana peel

The arrangement of cells can be broken down into layers in the X direction and the grading (variation in size) in the Y direction (see Figure 2.5). Four layers are easily identifiable. These layers are indicated by horizontal lines. The 1st layer from top is composed of closely packed cells. The 2nd layer is composed of bigger cells with more spacing among them. This variation in the pattern continues until the last layer, where cells are widely dispersed. The graded structure shows that the stiffness changes with thickness. According to structural mechanics, two different sized cross sections with the same shape factor have different stiffness. The bigger the cross section is, the lower the stiffness [13]. This structural property was verified by developing a 2D hexagonal truss model in MATLAB and running code for different sizes. (Appendix C).

The composition of the material also changes over volume. Material around the inner big cells is spongy and soft as compared to that around the top closely packed cells. This means if a foreign object hits a banana peel from the top (or a banana falls on another object), the inner cells would collapse first to protect the soft-core. This 'collapse mechanism' would flow up, and layers would continue crushing until the whole structure is compromised. It is evident that such a 'collapse mechanism' allows structures to reduce the kinetic energy of the object over a finite period of time, and the overall effect is a reduction in the impact load. Observation also shows that the presence of fluid in the cells enhances the integrity of the structure, and widely dispersed cells in the bottom layer do not communicate structurally with one another. This information leads to the hypothesis that the structure in a banana peel acts as a compact energy absorber. To verify the validity of this hypothesis, finite element analysis was executed in ABAQUS.

# CHAPTER 3. FINITE ELEMENT ANALYSIS

## 3.1 Background

Problems encountered in engineering mechanics are mostly represented by differential equations, and usually they are too complicated to be solved by classical analytical methods. Finite Element Analysis (FEA) is a numerical approach that seeks the approximate solution of differential equations.

The differential equations describing the problem may have a one, two or three dimensional domain (region). The FEA divides the whole region into smaller parts called the elements and approximates the solution sought for every element. The elements may be of the same size or all different depending upon the complexity of the geometry. The collection of all elements is called a finite element mesh. The elements are connected only at nodes. Each node defines the local degrees of freedom (DOF), and, the number of elements times the local DOF per node defines the global DOF of the model.

Once the type of approximation is selected, and mechanical behavior of the material is defined, the corresponding mechanical behavior of each element can be determined. Having determined the behavior of all elements, these elements are patched together using some specific rules to form the entire region that eventually enables an approximate solution for the entire body [14-20].

In order to investigate the impact response of a banana peel structure, a finite element analysis was executed in ABAQUS. The process was divided into three steps: modeling, analysis and collection and study of results.

### 3.2 Modeling

The base model has a 5 mm thick, 50 mm square solid plate. The material assigned is strain hardened Aluminum 1100-O. The true stress-true stain curve is approximated by the equation

$$\sigma = K.\varepsilon^{n} \qquad (3.1)$$

Where the strength coefficient,'K', is 180 MPa, and the strain-hardening exponent '*n*' is 0.2 [21].

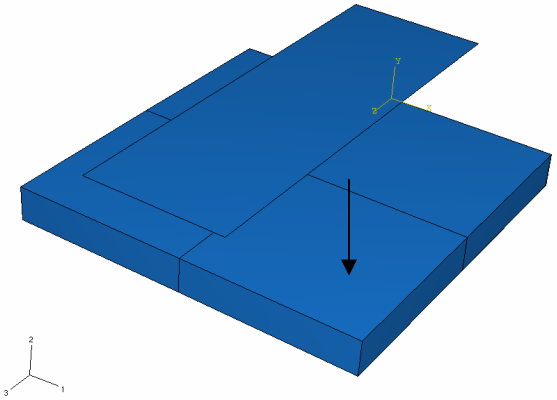

Figure 3.1: Rigid plate hitting the solid aluminum plate

The boundary conditions are defined by fixing the base of the plate and hitting it from the top with a rigid plate at different velocities in the Y plane as shown in Figure 3.1. The kinematic contact (Appendix E) is defined between the element based master rigid plate surface and the slave solid plate surface with the rough interaction property. The solid plate is meshed by using reduced integration, hourglass controlled, eight node, hexahedral elements; code name C3D8R (Appendix F). The cell shape is reverse engineered by utilizing the raster image capability of AUTOCAD as shown in Figure 3.2. The modification of the base model is carried out by incorporating the regular arrangement of the cells, i.e., one layer, two layers,

two graded layers etc as shown in Figure 3.3. The element based cell surfaces are used to define less stringent penalty contact properties with the rough interaction. These models are analyzed with the same boundary conditions. Based on the results of these models additional models are built that represent the actual structure more closely. These structures are named as modified design 1, 2, 3 and 4, respectively, as shown in Figure 3.3.

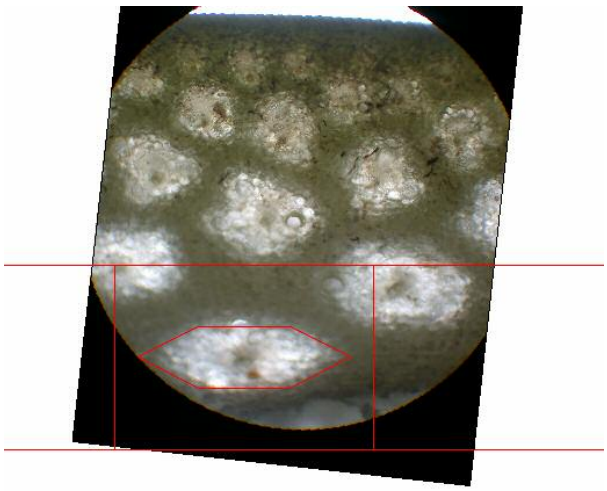

Figure 3.2: Replication of cell shape from a banana peel

### 3.3 Analysis

The ABAQUS Explicit module was used to execute the dynamic nonlinear structural analysis. The Explicit/Dynamics option employs a method of central-difference time integration to solve ordinary differential equations. The explicit central-difference operator satisfies the dynamic equilibrium equations at the beginning of the increment; the accelerations calculated at time 't' are used to advance the velocity solution to time $t+(\Delta t/2)$ and the displacement solution to time $(t+\Delta t)$ [22]. Since the solution is conditionally stable, a great amount of care was taken to define the time period of the analysis as well as the time increment scale factor (Appendix D).

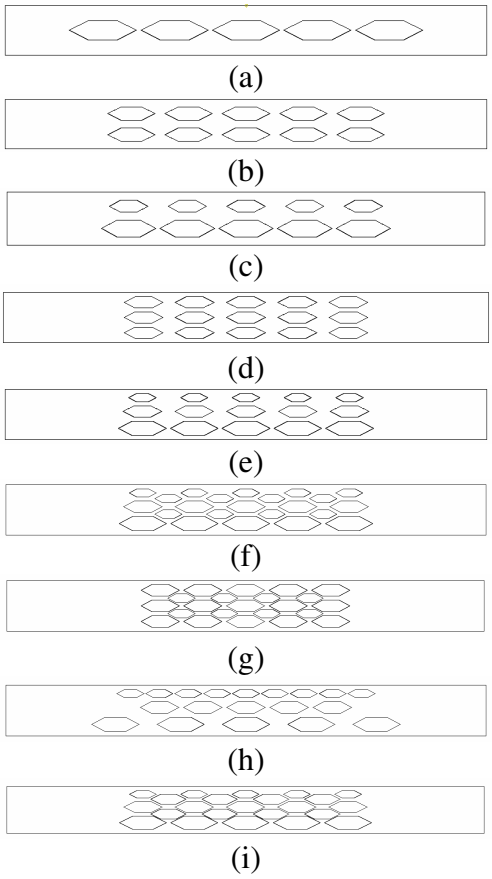


Figure 3.3: Aluminum with different cell packing (a) One layer model; (b) Two layer model; (c) Two graded layer model; (d) Three layer model; (e) Three graded layer model; (f) Modified design 1; (g) Modified deign 2; (h) Modified design 3; (i) Modified design 4

### 3.4 Results

Force vs. Displacement and Energy vs. Displacement curves at an impact velocity of 3 m/s are shown in Figures 3.5 and 3.6. These curves show that the modified designs are in agreement with the characteristics of energy absorbers presented in section 1.1 of Chapter 1. Below is a detailed review of these curves:

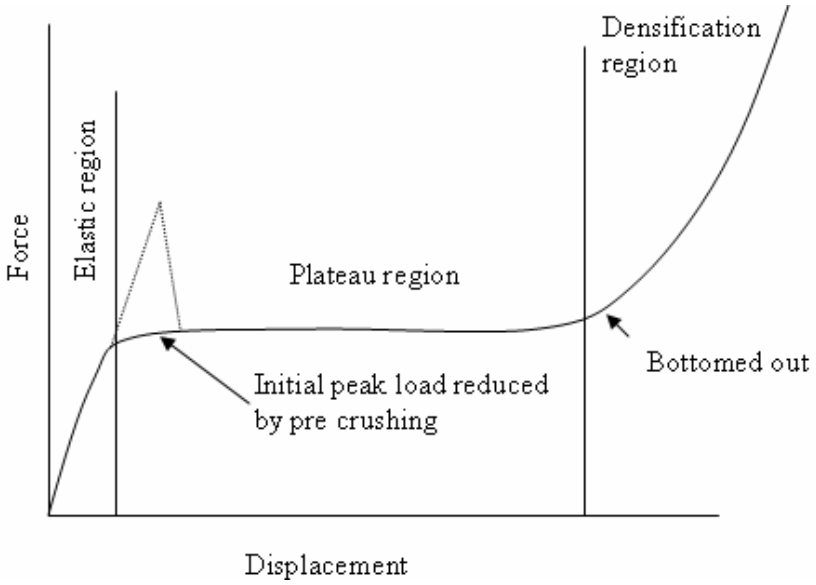


Figure 3.4: Dynamic Force-Displacement curve of a honeycomb structure

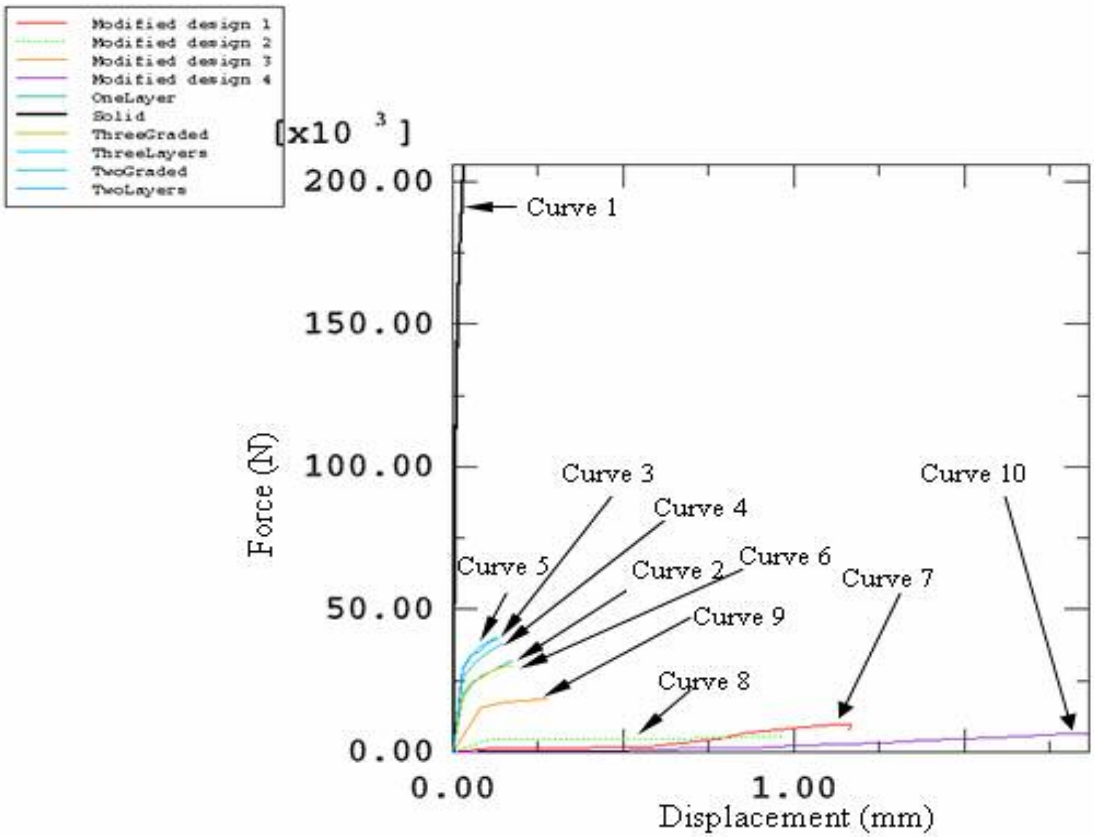


Figure 3.5: Force-Displacement curves at 3 m/s impact velocity

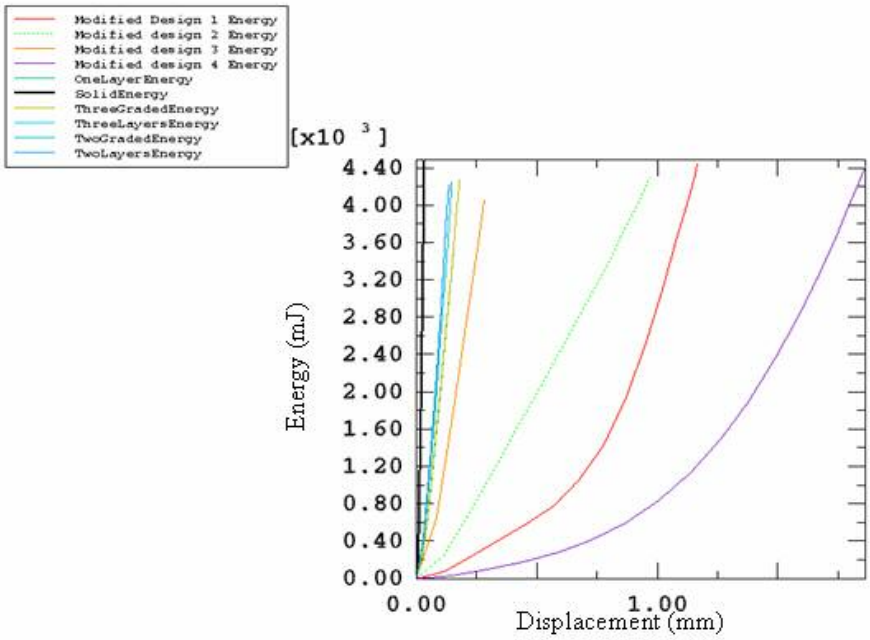


Figure 3.6: Energy-Displacement curves at 3 m/s impact velocity

Force displacement curves are a handy tool to visualize the variation of force with respect to the displacement. The area under the curve represents the external work or the energy absorbed by the energy absorber. Figure 3.4 shows a typical force-displacement curve of a honeycomb structure. The curve is divided into three parts: the elastic part where the cell walls deform elastically, the plateau region where cell walls start collapsing plastically, and the densification region where the cell walls start touching each other i.e., a condition of self contact [2, 22].

The force-displacement curves obtained from the analysis approximately follow the same pattern. As shown in Figure 3.5, the curve 1 represents the contact force experienced by the rigid plate when it hits the solid plate. The peak value of this force is 205,278N. The curve is very steep, showing that the rigid plate experiences high impact. Curve 2 represents the contact force of the rigid plate hitting the plate containing one layer of cells with the same

velocity. The force in this case is 31,720N. Deviation of the curve in the rightward direction favors conversion of kinetic energy into internal energy (Plastic energy + strain energy etc.) for both a longer period of time and displacement. This results in the reduction of contact force. Curves 3-6 represent the contact forces experienced by the rigid plate when it hits the aluminum plate having two layers, two graded layers, three layers and three graded layers respectively. The structure containing three graded layers exerts the lowest contact force in its family (i.e., among regular cell structures). Better results, in terms of lower contact force, can be obtained by modifying the three layer structure (by increasing cell density). From these results, two structures qualify for further improvement. These are the three layer and three graded layer models. Curve 7 represents the improved form of the three graded layer structure (modified design1) where cell density is increased by incorporating additional small cells among the graded cell columns as shown in Figure 3.3. The maximum contact force on the rigid plate in this case is 7,476N. This shows a considerable reduction of the contact force, almost 96.4% lower than the one experienced on the solid plate. A long stroke should be noted in this case. It is almost 97.33% greater than the one obtained in the solid plate case. Curve 8 illustrates the force experienced by the rigid plate when it hits the improved form of the three layer structure (Modified design 2). Equal sized cell columns are brought closer, and small cells are introduced among the regular columns. This structure is closer (shape and pattern are different; regular honeycomb structures have equal sized hexagonal cells) to the regular honeycomb structure and gives almost constant force (6,205N) over a stroke shorter than the modified design 1. It may me noted that some applications may benefit from such a pattern of force for example, the GSI (Gadd Severity Index), a number used to describe head injury in car crash, is minimum if acceleration remains constant along the stroke [23-26].

This design gives the lowest contact force among all the structures. Curve 9 shows the force when a rigid plate hits the modified design 3. This design is inferior to modified designs 1 and 2. However, it acts better than the regular layer designs. Curve 10 represents force displacement characteristics of the modified design 4. This design exhibits the longest stroke and minimum force with respect to the modified deigns 1, 2 and 3. The transfer of kinetic energy goes smoothly for a longer period of time, which reduces the contact force on the rigid plate for a good part of the stroke. The rigid plate experiences a force slightly higher (8.34 %) than the modified design 2.

Table 3.1 lists the percentage reduction in force with respect to the solid plate, and the maximum forces experienced by the rigid plate at different impact velocities. It can be seen that as the velocity increases, the reduction in the contact force with respect to the solid plate decreases. The reason is that the increase in velocity causes the structure to utilize more stroke. The complete utilization of stroke ends in a densification region where contact force increases rapidly.

Table 3.1: Maximum force and percentage reduction in contact force at different velocities

| Impact velocity (m/sec) | 3 | | 5 | | 8 | | 10 | | 12 | |
|---|---|---|---|---|---|---|---|---|---|---|
| Structure | Fmax(N) | %reduction in force | Fmax(N) | %reduction in force | Fmax(N) | %reduction in force | Fmax(N) | %reduction in force | Fmax(N) | %reduction in force |
| Solid | 205278 | 0 | 250024 | 0.00 | 308820 | 0.00 | 340897 | 0.00 | 368792 | 0.00 |
| OneLayer | 31720 | 84.70 | 40120 | 83.95 | 77595 | 74.87 | 90359 | 73.49 | 136134 | 63.09 |
| TwoLayers | 39609 | 80.89 | 47506 | 81.00 | 65680 | 78.73 | 88369 | 74.08 | 111476 | 69.77 |
| TwoGraded | 37313 | 82.00 | 46348 | 81.46 | 70414 | 77.20 | 87335 | 74.38 | 112570 | 69.48 |
| ThreeLayers | 40571 | 80.43 | 49192 | 80.33 | 60963 | 80.26 | 76349 | 77.60 | 90101 | 75.57 |
| ThreeGraded | 30195 | 85.43 | 48943 | 80.42 | 68291 | 77.89 | 80143 | 76.49 | 102715 | 72.15 |
| Modified Design 1 | 7476.8 | 96.39 | 27060 | 89.18 | 76496 | 75.23 | 119895 | 64.83 | 158342 | 57.06 |
| Modified Design 2 | 5625 | 97.29 | 25436 | 89.83 | 22678 | 92.66 | 77008 | 77.41 | 63696 | 82.73 |
| Modified Design 3 | 18027 | 91.30 | 24113 | 90.36 | 33562 | 89.13 | 71439 | 79.04 | 124628 | 66.21 |
| Modified Design 4 | 6137 | 97.04 | 28763 | 88.50 | 93161 | 69.83 | 131464 | 61.44 | 198610 | 46.15 |

### 3.4.1 Energy

Figure 3.6 shows the energy absorbed by the aluminum plate with different structures at 3 m/s impact velocity. As mentioned in Section 1, the absorbed energy should be in irreversible form. The higher the irreversible portion of the internal energy, the lower the rebound and the better the energy absorber. In this case the internal energy is composed of the plastic energy, elastic energy, viscous dissipation energy (the energy dissipated by damping mechanisms, including bulk viscosity damping and material damping), and the artificial energy (energy stored in hourglass resistance or controlling zero energy modes). The plastic energy and the entrapped elastic energy make up the irrecoverable portion of the internal energy.

Since the plate rebounds in all cases, the area under the force-displacement curve for all the cases is constant. This means the plate having solid and regular/graded structures absorbs all the kinetic energy at the end of the stroke. However, the way it is absorbed is different in each case. The energy curves in Figure 3.6 show that the modified designs 1,2 and 4 absorbed a major portion of the kinetic energy in the latter part of the stroke (due to higher plastic deformation and strain hardening effects). Modified design 3 and the regular layer designs absorbed energy at almost a constant rate. Table 3.2 shows the amount of plastic energy, elastic energy, total absorbed (internal) energy and the entrapped elastic energy stored in the aluminum plate at the end of the stroke for 3 m/s. The maximum energy is absorbed by modified design 2, followed by the three graded layer design, modified design 3 and modified design 4 (in terms of the percentage increment in energy absorption). The difference between stored elastic and entrapped elastic energy explains how much energy is available for the aluminum plate to do negative work on the rigid plate to cause rebound. The modified design 3 gives the lowest rebound velocity of 0.442 m/s.

The absorbed energy and the rebound velocities for the rest of the cases are presented in Table 3.2. For higher velocities, the relative increase in energy absorption is less because most of the structures reach their stroke limit and start to act more like a solid plate. For example, at 12 m/s impact velocity, the percentage increase in energy absorption with respect to the solid plate is approximately 4.5 % as compared to the number 24.46 % at 3 m/s impact velocity.

### 3.4.2 Simulations

Figures 3.7-3.16 show the deformed models at the end of the stroke for a 3 m/s impact velocity. The contours represent the distribution of Von Mises stresses in the aluminum plate. It is worth noting that the cells in the center layers of the modified designs collapse first. This means that the 'collapse mechanism' starts first in the walls of the center layer cells [27]. The deformed model of modified design 4 shows that almost all the cells are crushed, and any further increase in the velocity results in a densification of structure. The values in Table 3.1 also indicate that the modified design 4 is inferior to other designs for velocities higher than 3 m/s. Deformed models of modified designs 1-3 show potential to crush further and hence act as good energy absorbers for higher velocities. This is especially true for modified design 2. For higher velocities the same crushing pattern is observed. The cells in the center layer collapse first followed by cells in the bottom layer. The top cells collapse at the end of the stroke.

Table 3.2: Energy comparison of structures at different velocities

| | Impact velocity (3 m/sec) | | | | | |
|---|---|---|---|---|---|---|
| STRUCTURE | P.E (mJ) | E.E (mJ) | I.E (mJ) | E.S.E (mJ) | R.V (m/sec) | A |
| Solid | 2965 | 1527 | 3325 | 180 | 1.53 | |
| One Layer | 4289 | 202 | 4338 | 40 | 0.57 | 23.35 |
| Two Layers | 4287 | 216 | 4333 | 45 | 0.58 | 23.26 |
| Two Graded Layers | 4296 | 199 | 4348 | 52 | 0.55 | 23.52 |
| Three Layers | 4309 | 187 | 4338 | 29 | 0.57 | 23.35 |
| Three Graded Layers | 4356 | 143 | 4388 | 32 | 0.47 | 24.22 |
| Modified Design 1 | 4343.7 | 113 | 4361 | 18 | 0.52 | 23.75 |
| Modified Design 2 | 4381 | 66 | 4402 | 21 | 0.44 | 24.46 |
| Modified Design 3 | 4364 | 117 | 4385 | 21 | 0.48 | 24.17 |
| Modified Design 4 | 4347 | 95 | 4368 | 21 | 0.5 | 23.87 |
| | Impact velocity (5 m/sec) | | | | | |
| Solid | 10099 | 2370 | 10693 | 263 | 1.9 | |
| One Layer | 12165 | 320 | 12242 | 77 | 0.71 | 12.65 |
| Two Layers | 12188 | 304 | 12260 | 72 | 0.69 | 12.78 |
| Two Graded Layers | 12183 | 299 | 12268 | 85 | 0.68 | 12.83 |
| Three Layers | 12221 | 267 | 12265 | 44 | 0.68 | 12.81 |
| Three Graded Layers | 12211 | 254 | 12261 | 50 | 0.69 | 12.78 |
| Modified Design 1 | 12189 | 181 | 12212 | 24 | 0.75 | 12.43 |
| Modified Design 2 | 12286 | 148 | 12315 | 29 | 0.6 | 13.17 |
| Modified Design 3 | 12278 | 185 | 12311 | 34 | 0.61 | 13.14 |
| Modified Design 4 | 12153 | 188 | 12173 | 21 | 0.8 | 12.15 |
| | Impact velocity (8 m/sec) | | | | | |
| Solid | 28401 | 3593 | 29303 | 376 | 2.32 | |
| One Layer | 31259 | 594 | 31381 | 122 | 1.11 | 6.62 |
| Two Layers | 31499 | 429 | 31599 | 100 | 0.89 | 7.26 |
| Two Graded Layers | 31405 | 522 | 31549 | 145 | 0.95 | 7.11 |
| Three Layers | 31611 | 359 | 31669 | 60 | 0.81 | 7.47 |
| Three Graded Layers | 31535 | 382 | 31607 | 72 | 0.88 | 7.3 |
| Modified Design 1 | 31146 | 374 | 31207 | 62 | 0.26 | 6.1 |
| Modified Design 2 | 31486 | 284 | 31545 | 60 | 0.95 | 7.1 |
| Modified Design 3 | 31610 | 301 | 31679 | 70 | 0.8 | 7.5 |
| Modified Design 4 | 30901 | 407 | 30952 | 52 | 1.45 | 5.32 |
| | Impact velocity (10 m/sec) | | | | | |
| Solid | 45531 | 4022 | 46628 | 462 | 2.6 | |
| One Layer | 49072 | 742 | 49228 | 156 | 1.24 | 5.28 |
| Two Layers | 49261 | 575 | 49387 | 128 | 1.1 | 5.58 |
| Two Graded Layers | 49190 | 678 | 49367 | 179 | 1.12 | 5.5 |
| Three Layers | 49492 | 427 | 49562 | 70 | 0.93 | 5.91 |
| Three Graded Layers | 49385 | 470 | 49474 | 91 | 1.02 | 5.75 |
| Modified Design 1 | 48613 | 539 | 48689 | 78 | 1.61 | 4.23 |
| Modified Design 2 | 49130 | 403 | 49214 | 84 | 1.25 | 5.25 |
| Modified Design 3 | 49326 | 452 | 49429 | 105 | 1.06 | 5.66 |
| Modified Design 4 | 48199 | 545 | 48282 | 84 | 1.85 | 3.42 |
| | Impact velocity (12 m/sec) | | | | | |
| Solid | 66880 | 4837 | 68200 | 715 | 2.75 | |
| One Layer | 70561 | 1071 | 70757 | 200 | 1.57 | 3.61 |
| Two Layers | 71018 | 712 | 71174 | 158 | 1.28 | 4.17 |
| Two Graded Layers | 70938 | 830 | 71154 | 219 | 1.3 | 4.15 |
| Three Layers | 71289 | 498 | 71415 | 127 | 1.08 | 4.5 |
| Three Graded Layers | 71207 | 567 | 71325 | 119 | 1.16 | 4.38 |
| Modified Design 1 | 69981 | 754 | 70080 | 101 | 1.95 | 2.68 |
| Modified Design 2 | 70562 | 582 | 70677 | 116 | 1.62 | 3.5 |
| Modified Design 3 | 70762 | 732 | 70911 | 151 | 1.47 | 3.82 |
| Modified Design 4 | 68855 | 922 | 68960 | 106 | 2.46 | 1.1 |

P.E = Plastic energy; E.E = Elastic energy; I.E = Internal energy; E.S.E = Entrapped elastic energy; R.V = Rebound velocity; A = percentage increase in absorbed energy with respect to the solid plate.

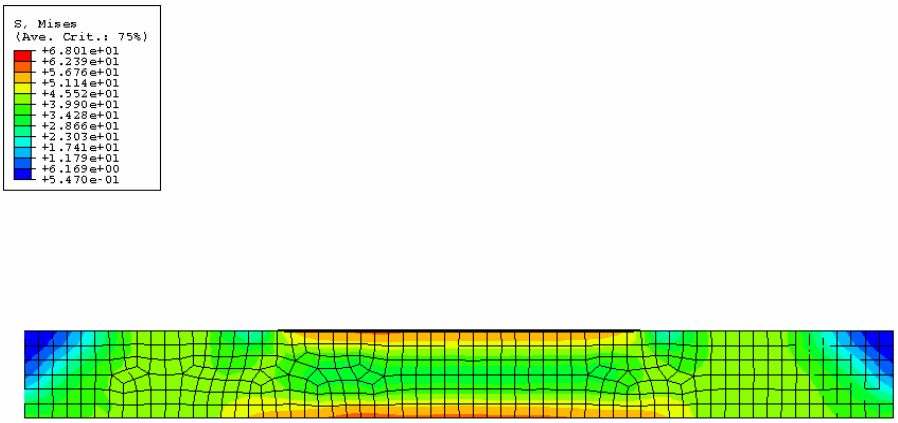


Figure 3.7: Deformed solid plate at the end of the stroke

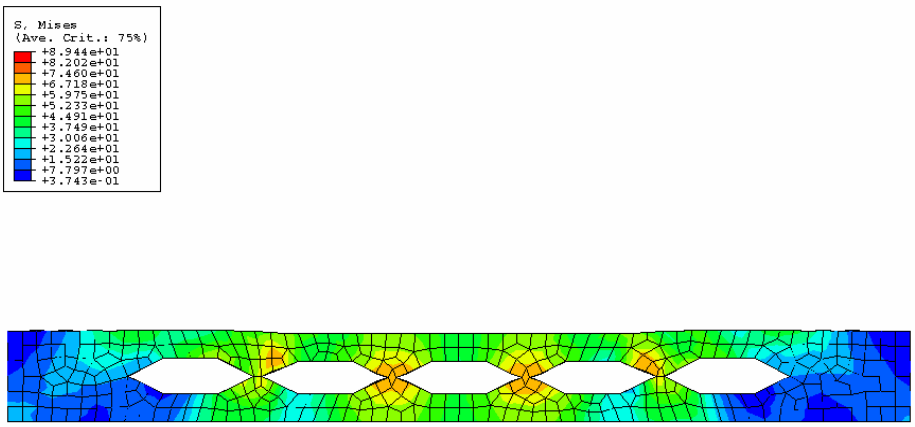


Figure 3.8: Deformed plate containing one layer of cells, at the end of the stroke

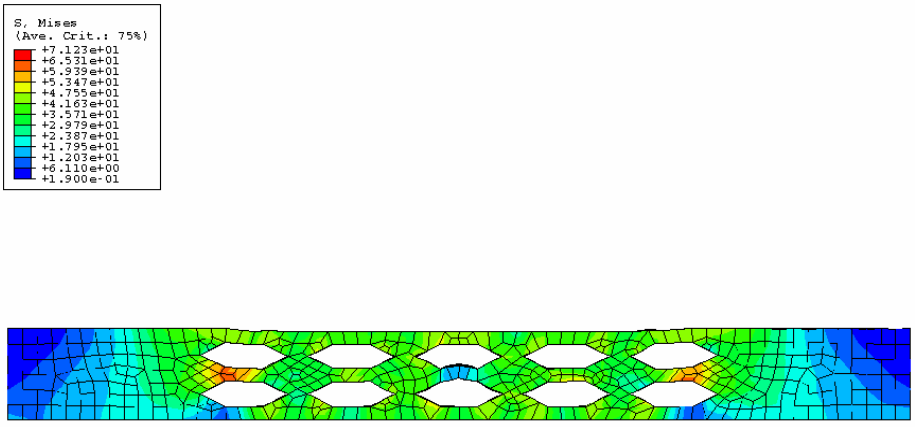


Figure 3.9: Deformed plate containing two layers of cells, at the end of the stroke

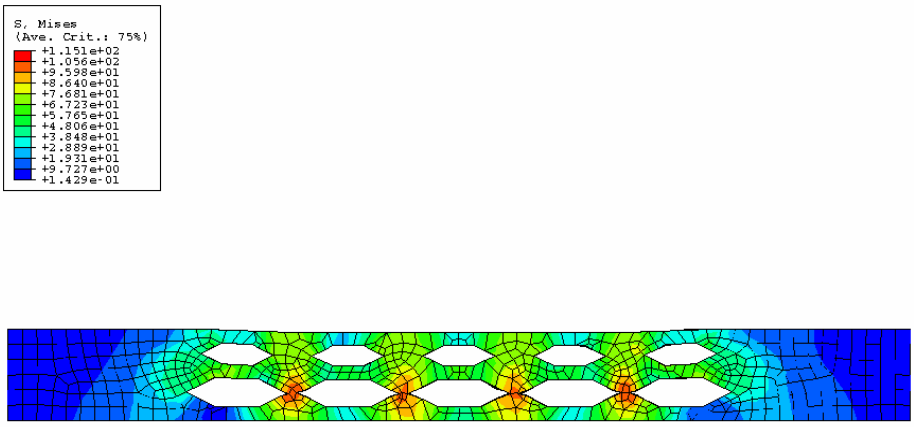


Figure 3.10: Deformed plate containing two graded layers of cells, at the end of the stroke

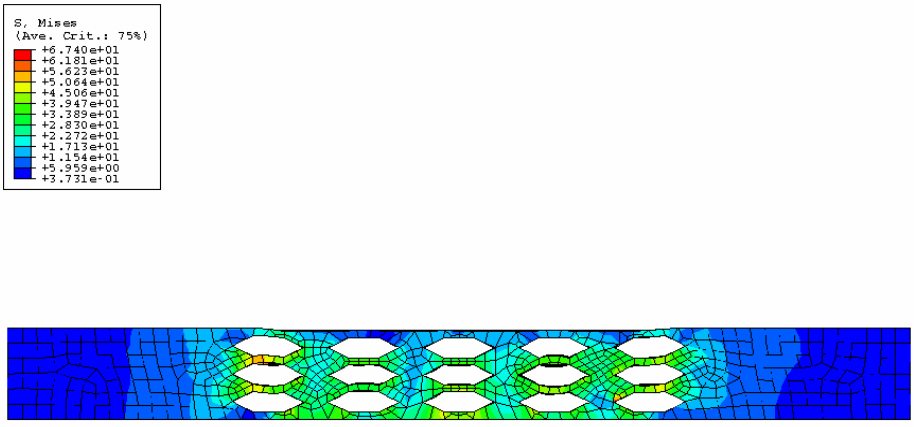


Figure 3.11: Deformed plate containing three layers of cells, at the end of the stroke

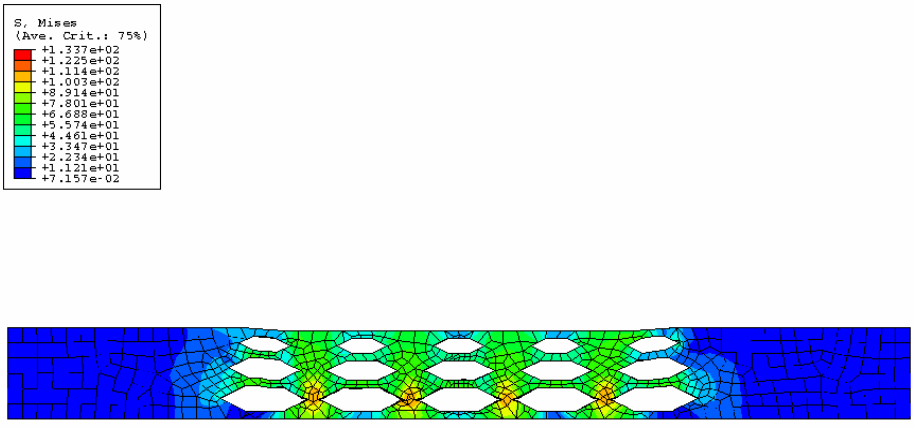


Figure 3.12: Deformed plate containing three graded layers of cells, at the end of the stroke

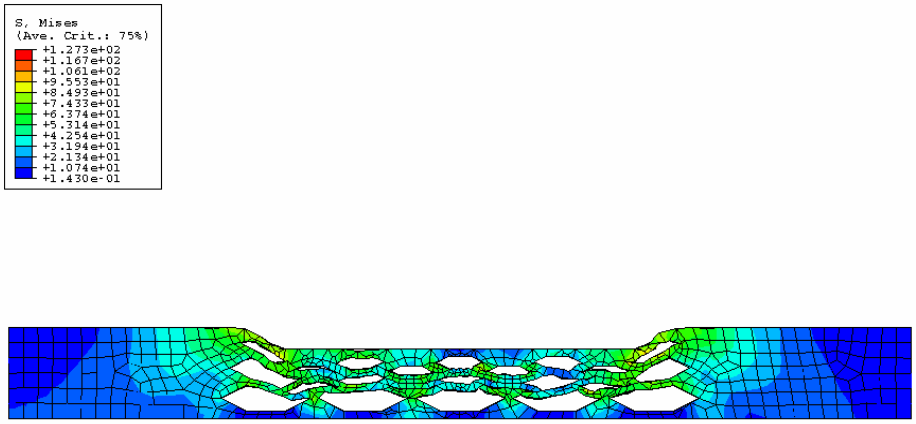


Figure 3.13: Deformed plate containing modified design 1 structure, at the end of the stroke

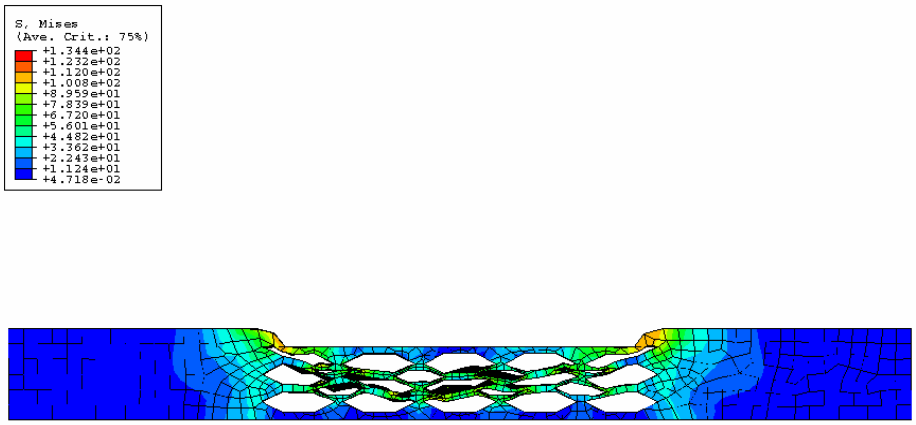


Figure 3.14: Deformed plate containing modified design 2 structure, at the end of the stroke

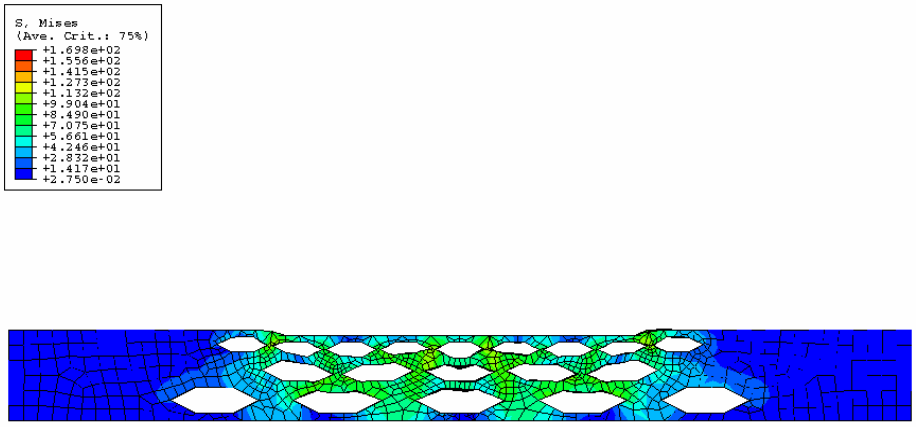


Figure 3.15: Deformed plate containing modified design 3 structure, at the end of the stroke

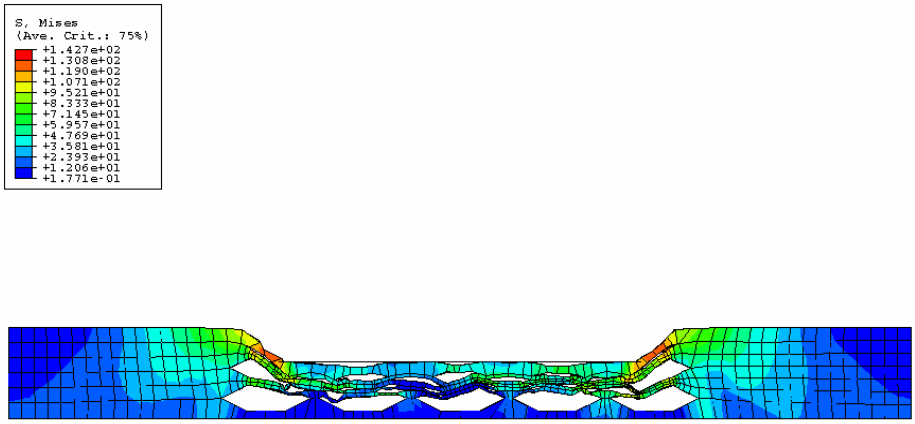


Figure 3.16: Deformed plate containing modified design 4 structure, at the end of the stroke

In order to study the effect of fluid in cells and variation in the material composition along the thickness, two additional models are constructed. Figure 3.17 shows the model containing cells filled with crushable foam material. Figure 3.18 depicts a composite graded cellular structure consisting of layers of soft, medium hard and hard crushable foam. The stress-strain and energy curves showed a significant drop in the contact force and the rebound. Furthermore, the 'collapse mechanism' initiated from the fixed base in contrast to previous models where the middle layer started to crush first [28-30].

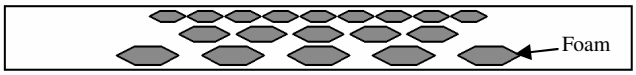


Figure 3.17: Model containing cells filled with crushable foam

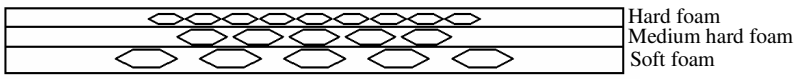


Figure 3.18: Composite graded section

# CHAPTER 4. THEORETICAL ANALYSIS

The FEA analysis presented in the previous chapter gives good insight into the failure mechanism and mechanical response of a banana peel structure under compression. However, the theoretical analysis of a banana peel structure requires the understanding of honeycombs.

Honeycombs are a typical type of cellular structure. Their structure consists of a regular two dimensional array of hexagonal cells. Other cell shapes are also possible, such as square, triangular, circular or rhombic. However, this thesis will focus only on hexagonal shaped cells in this thesis. The term "honeycomb" will be used for "regular uniform cell wall thickness hexagonal honeycombs" (unless otherwise stated). Honeycombs offer excellent strength to weight ratio, and they are considered to be one of the prime structures for cores in sandwich panel beams. They also possess good energy absorbing characteristics as described in Chapter 1. A simple two dimensional regular honeycomb structure is shown in Figure 4.1.

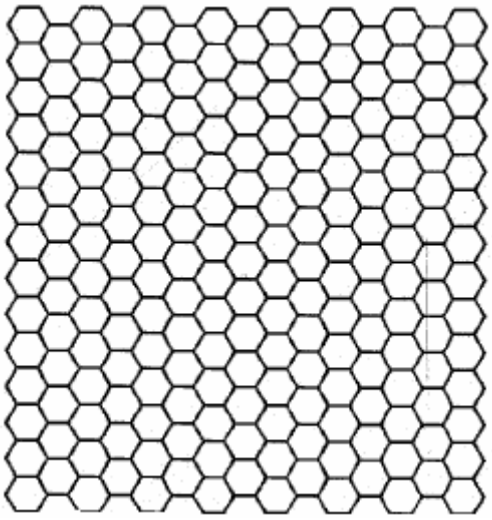

Figure 4.1: The regular two dimensional honeycomb structure

Extensive work has been done in understanding the in-plane mechanical behavior of two dimensional honeycombs. Abd El-Sayed et al [31] calculated the in-plane Young's moduli and Poisson's ratios for honeycomb sheets by estimating the bending and axial displacements of a cell under two dimensional loading. Gibson and Ashby [27] presented a more comprehensive analysis of two and three dimensional (foam) honeycombs under quasi-static loading and verified their findings by experiment. Papka and Kyriades [32-35] studied the experimental response of in-plane uniaxial and biaxial crushing of metal honeycombs and compared the results with finite element simulation. Silva, Hayes and Gibson [36-37] investigated the effects of non-periodic two-dimensional arrangements of cells on the elastic properties and strength to comprehend the crushing process of irregular honeycombs.

The analytical study carried out by Gibson and Ashby is considered to be the most accurate one in describing the deformation modes and failure mechanism of honeycombs. Therefore, their work is presented in detail. This understanding will be applied to the graded banana peel structure to develop the theoretical model.

### 4.1 The mechanics of honeycombs

Figure 4.2 shows a unit cell of a honeycomb with the definitions of parameters. The response of honeycombs under compressive loading is described by five moduli: two Young's moduli, $E_1$ and $E_2$, a shear modulus, $G_{12}$, and two Poisson's ratios, $v_{12}$ and $v_{21}$. If the hexagon is regular (i.e., all sides are equal and making $120^o$ angles with respect to each other) and the cell walls are all of the same thickness, then the in-plane properties are isotropic, i.e., they do not depend on direction, and the five moduli reduce to three.

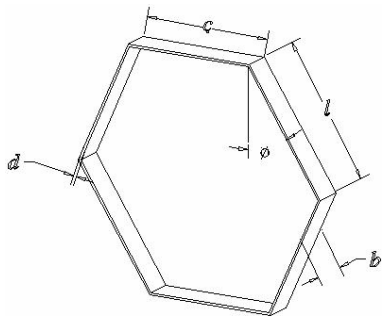


Figure 4.2: A unit cell of a regular honeycomb

Since the cells in the peel are under compressive loading in the Y direction as described in Chapter 2, therefore, only the moduli that describe the in-plane response of the honeycomb in the Y direction are considered. The Young's modulus, shear modulus and Poisson's ratio of the uniform wall thickness honeycomb in the Y direction is presented as

$$E_1 = \left(\frac{d}{l}\right)^3 \frac{\cos\phi}{\left(\frac{c}{l}+\sin\phi\right)\sin^2\phi} E \tag{4.1}$$

where E is the Young's modulus of the material of the honeycomb structure.

$$G_1 = \left(\frac{d}{l}\right)^3 \frac{\left(\frac{c}{l}+\sin\phi\right)}{\left(\frac{c}{l}\right)^2\left(1+\frac{2c}{l}\right)\cos\phi} E \tag{4.2}$$

$$v_{12} = \left(\frac{\cos^2\theta}{\left(\frac{c}{l}+\sin\theta\right)\sin\theta}\right) \tag{4.3}$$

Please refer to Appendix G for more details about the derivation of the above expressions.

The most important parameters characterizing a cellular material's energy absorption properties are the plastic collapse stress generally known as the plateau stress and the relative density.

The upper and lower bound theorems are used to determine the plateau stress. According to the upper bound theorem, an external load computed on the basis of an assumed mechanism, in which the forces are in equilibrium, is always greater than or equal to the true collapse load. The lower bound theorem says that an external load computed on the basis of an assumed distribution of internal forces, in which the forces are bounded by limit values, and the forces are in equilibrium, is less than or equal to the true collapse load [38].

### 4.1.1 Upper bound collapse stress

The compressive load in the Y direction is transferred to the inclined walls, and they bend very much like a structure. The plastic analysis shows that six plastic hinges [39] are required to define the complete 'collapse mechanism' of a cell. Figure 4.3 shows the inclined wall undergoing angular rotation, $\psi$, with respect to its original position. An upper bound on the load acting on the wall is given by

$$P = \sigma_p (c + l \sin\psi) b \tag{4.4}$$

where '$\sigma_p$' is the plateau stress. The distance moved by the load in the Y direction is

$$y = l\psi \sin\phi \tag{4.5}$$

The negative work done in four plastic hinges is equal to the plastic moment times the relative angular displacement, $\psi$, while the external work is equal to the product of the magnitude of the load times the distance traveled by the load. Therefore,

$$4M_p\psi = 2P\sigma_p(c + l\sin\phi)bl\psi\sin\phi \tag{4.6}$$

Assuming an elastic-perfectly plastic material, the plastic bending moment $M_P$ is

$$M_p = \frac{bd^2}{4}\sigma_y \tag{4.7}$$

where $\sigma_y$ is the yield strength of the cell-wall material [40]. Equation 4.6 then gives the plateau stress expression

$$\sigma_p = \left(\frac{d}{l}\right)^2 \frac{1}{2(c/l + \sin\phi)\sin\phi}\sigma_y \tag{4.8}$$

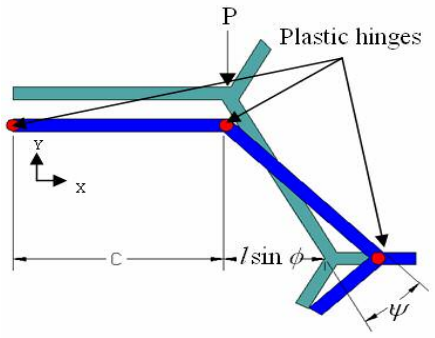


Figure 4.3: Plastic collapse of inclined walls in the Y direction

### 4.1.2 Lower bound collapse stress

A lower bound on a collapse load is calculated by equating the internal negative moment on the cell wall to the external positive moment as shown in Figure 4.4.

$$2M_p = P\sin\varphi l \tag{4.9}$$

$$2\frac{bd^2}{4}\sigma_y = \sigma_p (c + l\sin\varphi) b \sin\phi l$$

$$\sigma_p = \left(\frac{d}{l}\right)^2 \frac{1}{2\left(d/l + \sin\phi\right)\sin\phi}\sigma_y \tag{4.10}$$

Since the collapse load obtained from the lower and the upper bound theorem is the same, it is the exact solution [27].

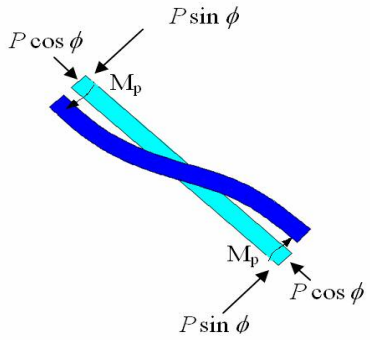


Figure 4.4: Internal and external bending moment on the inclined wall

### 4.1.3 Locking strain

The locking or densification strain is defined as the ratio of the density of the cellular material to the density of the material of the honeycomb. The relative density is usually expressed as

$$\rho = \frac{\frac{d}{l}\left(\frac{c}{l} + 2\right)}{2\cos\phi\left(\frac{c}{l} + \sin\phi\right)}\rho_s \tag{4.11}$$

Where, $\rho_s$, is the density of the material of the honeycomb. Please refer to Appendix G for the derivation of the above expression. The porosity, which in fact is the pore volume, is $(1-\frac{\rho}{\rho_s})$. The porosity is theoretically equal to the densification or locking strain $\varepsilon_d$

$$\varepsilon_d = 1-\frac{\rho^*}{\rho_s} = 1-\frac{\frac{d}{l}(2+\frac{c}{l})}{2\cos\varphi(\sin\phi+\frac{c}{l})} \tag{4.12}$$

The locking strain defines the end of the stroke.

Equations 4.1-4.12 define the in-plane behavior of a honeycomb structure. These expressions were derived and verified by Gibson [41-42]. The banana peel structure is too complex for these equations to handle. Therefore, a few assumptions are made to redefine the structure without excessive deviation from the peel structure. It is assumed that:

- the material is homogenous along the thickness.
- the cells have constant shape factor.
- the cells are arranged in a uniform order.

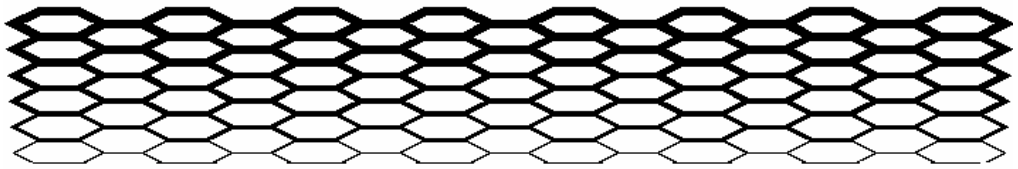

Figure 4.5: The modified peel structure

Figure 4.5 shows the modified peel structure. This structure will be called the graded honeycomb structure (GHS). Since the thickness of the cell walls is changing, the equations presented above can only capture the response of individual rows. The global response of the

structure can be achieved by summing up the local response of individual rows. Figure 4.6 depicts the global theoretical response of the GHS in terms of the stress-strain curve. In order to verify the correctness of equations 4.1-4.12, a finite element analysis was executed.

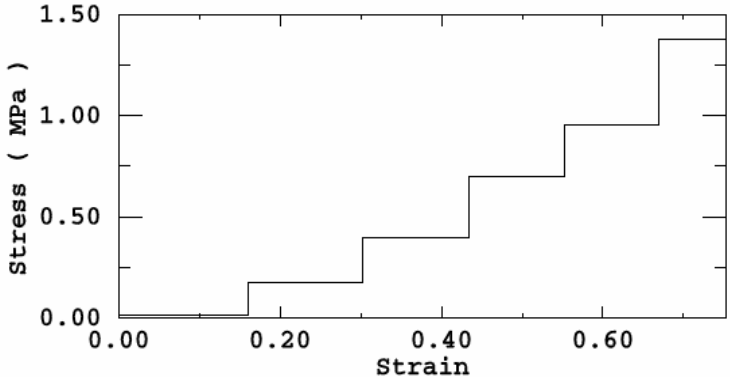


Figure 4.6: The theoretical response of GHS in the Y direction using equation 4.10

## 4.2 Finite element analysis of GHS

### 4.2.1 Modeling

The three dimensional shell model was constructed using the ABAQUS PART module. The structure is composed of 6 cells in the Y direction and 15 cells in the X direction with the unit cell dimensions of $l$ = 2.23 mm, $c$ = 3 mm, and $\phi = 62.3^0$ as shown in Figure 4.7. Hourglass controlled, 4 nodes, reduced integration shell elements (S4R) were used to mesh the structure. Eleven elements were defined along the length of the inclined walls and 5 elements along the width. The horizontal walls have the same number of elements along the width and 15 elements along the length. The boundary conditions are defined by constraining the discrete rigid plate, A, to move only in the Y plane and by fixing all the rotational and translational degrees of freedom of the discrete rigid plate, B. Both plates were discretized by using rigid bilinear quadrilateral elements (R3D4). The model has

a total of 17,910 elements. Interaction properties were imposed using a general contact condition and surface to surface kinematic contact conditions between the top element based surface of the structure and the rigid plate, A. A penalty contact condition of frictionless tangential behavior was applied between the bottom element based surface of the structure and the rigid plate, B. The cell wall material is assumed to be an elastic-perfectly plastic material with a Young's modulus of 69 MPa and yield strength of 76 MPa. The overall length and height of the model is 77 mm and 12 mm respectively. The wall thickness assigned to layers 1-6 are 0.05, 0.2, 0.3, 0.4, 0.5 and 0.6 mm respectively.

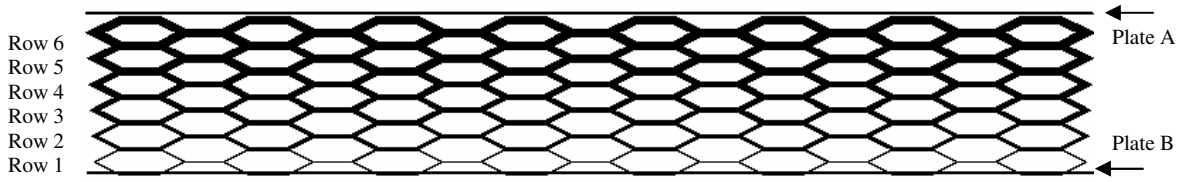


Figure 4.7: The shell model of graded honeycomb structure (GHS)

### 4.2.2 Results

Figure 4.8 displays the theoretical and finite element response of GHS under quasi-static loading. The stress-strain curve is obtained by extracting the contact force on the rigid plate, B, and the displacement of the rigid plate, A, from its original position. The theoretical results are in agreement with the FE results for rows 1 and 2, but as the cell wall thickness increases, the theoretical curve predicts lower values of the plateau stresses. This discrepancy was investigated and two possible reasons were found. First, the inclined cell walls carry shear and axial loads that cause shear and axial deflections [27]. Second, the plastic deformation occurs over a zone instead of being confined in a localized plastic hinge of zero length [2, 41-45].

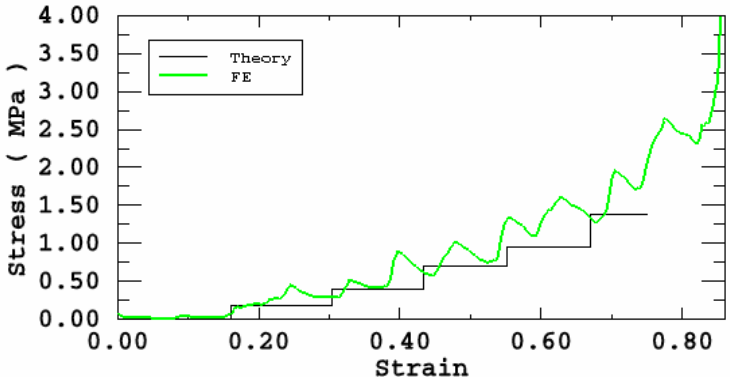


Figure 4.8: The superimposed theoretical and finite element output

For $\frac{d}{l} < 0.25$, the axial and shear deflections are small compared to bending deflections. Therefore, they do not significantly affect the plateau stress and bending moment considerably [27]. Plastic hinge length itself has little effect on the load but significantly changes the deformation geometry and hence the moment arm of the bending moment [2]. Therefore, only the plastic hinge length effect was taken into account to modify equation 4.8. The length of the plastic hinge was obtained by observing the values of bending moment, equivalent plastic strains and Von Mises stress [46-48] at the integration points of the shell elements in the FE analysis. It was found to equal half the thickness of the cell wall. The equation obtained by incorporating the plastic hinge length effect is

$$\sigma_p = \frac{d^2}{2(c + l\sin\phi)(l-d)\sin\phi}\sigma_y \qquad (4.13)$$

By incorporating the large strain effects and small angle approximation, Equation 4.13 can be rewritten as

$$\sigma_p = \frac{d^2}{2[c + l(\sin\phi + \delta\phi\cos\phi)](l-d)(\sin\phi + \delta\phi\cos\phi)}\sigma_y \qquad (4.14)$$

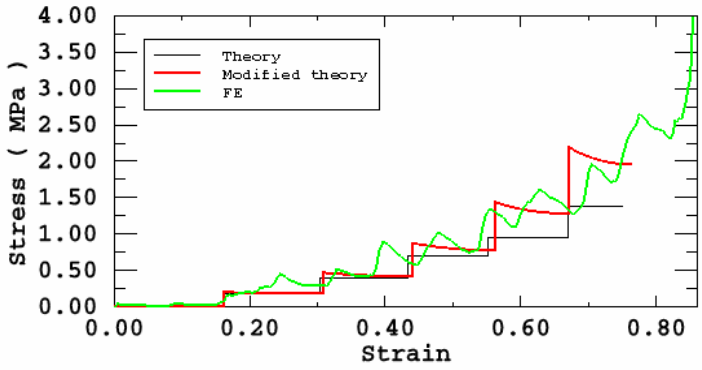


Figure 4.9: The comparison of the theoretical and modified theoretical response of GHS with respect to the finite element analysis

Where $\delta\phi$ is a small increment in $\phi$. Equation 4.14 was solved iteratively in MATLAB. Figure 4.9 displays the superimposed output of the FE analysis, Equation 4.8 (Theory) and 4.14 (Modified theory). Thus, Equation 4.14 agrees with the FE solution. Equation 4.14 was also tested for graded honeycombs of different sets of thicknesses under quasi-static loading and results were found to be consistent with the FE analysis.

# CHAPTER 5. STUDY OF GRADED HONEYCOMB STRUCTURE (GHS) UNDER IMPACT

This chapter discusses the behavior of the graded honeycomb structure under dynamic loading. Regular honeycombs exhibit two distinct phenomena for high loading rates, the increase in plateau stress and deformation modes. Hoing and Strong [49-50] analyzed the in-plane dynamic behavior of honeycombs. They studied the dynamics of crush band initiation and wave trapping under impact loading using ABAQUS. They presented expressions for critical velocity by employing the theory of wave trapping. Ruan, Lu, Wang and Yu [51] studied in-plane dynamic crushing of honeycombs and explored the influence of cell wall thickness and impact velocity on the deformation mode and plateau stresses by using ABAQUS and proposed an empirical formula for computing the dynamic plateau stresses at high impact velocities. Zhao and Gary [52] examined the in-plane and out of plane dynamic response of honeycomb structures using viscoelastic split bars. Reid *et al*. [53-55] studied the behavior of a one-dimensional ring system under end impact and expanded their results to a wood model. In these studies, the sensitivity of cellular structures to initial crushing strength and mode shapes was noted.

Similar to regular honeycomb structures (RHS), the graded honeycomb structures also show sensitivity to loading rate. However, the increase in plateau stress and the type of deformation modes are different. The rest of this chapter presents details of the analysis of the GHS at low and high impact velocities, and a simple shock model is presented to calculate the crushing stress and locking strain of the GHS.

## 5.1 Deformation modes of GHS under dynamic loading

Unlike regular honeycomb structures that undergo 'X', 'V' and 'I' mode deformation [51], the graded honeycomb structures undergo 'I' model deformation for both low and high speed impact velocities. Here, the impact velocity that causes a strain rate equal or less than 1000 $s^{-1}$ is termed low impact velocity. All the velocity values causing deformation rates higher than 1000 $s^{-1}$ will fall into the high speed category.

In order to understand the behavior of the GHS under dynamic loading, a Finite Element Analysis was executed in the ABQUS EXPLICIT module on the model described in the Chapter 4. Figure 5.1 shows the deformed structure at the end of the crushing process. At 1 m/s impact velocity, row 1 is completely crushed (see Figure 5.1a.) The displacement of the rigid plate, A, is 1.4538 mm. As the impact velocity increases, the deformation progressively shifts to other layers. At 6 m/s impact velocity and a step time of 1.134 ms, rows 1 and 2 are completely crushed, while row 3 is left partially intact as shown in Figure 5.1c. At impact velocities of 9, 13 and 16 m/s, crushing advances smoothly to row 3, 4, 5 and 6 as shown in Figures 5.1d-f. At an impact velocity of 20 m/s, the rigid plate, A, completely crushes the structure (Figure 5.1g). It may be noted that for these low range velocities, the crushing initiates from the distal end and advances to the proximal end.

## 5.2 Stress -Strain curve

Figure 5.2 depicts the stress-strain curves of model 2 at 3, 9 and 20 m/s impact velocities. The stress-strain curves are developed by extracting the contact force on the rigid plate, B. The magnitude of the total contact force dictates how much force the rigid plate, B,

experiences from the impact of the rigid plate, A, on the structure. The modified theoretical result (equation 4.14) shows good agreement with the FE results in the plateau regimes.

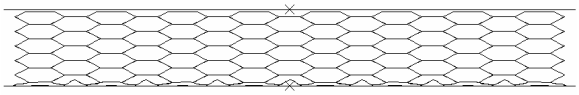

(a) Δ = 1.44mm, v = 1 m/s (t =3.15 ms)

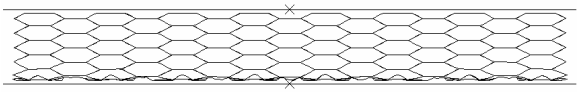

(b) Δ 2.57mm, v = 1.25 m/s (t =1.25 ms)

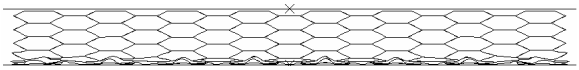

(c) Δ = 4.16mm, v = 6 m/s (t =1.134 ms)

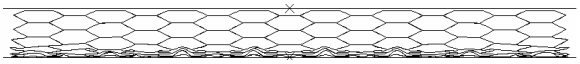

(d) Δ = 5.47mm, v = 9 m/s (t =0.97 ms)

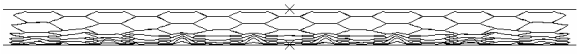

(e) Δ = 7.21mm, v =1 3 m/s (t =0.88 ms)

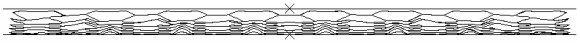

(f) Δ = 8.44mm, v = 16 m/s (t =0.833 ms)

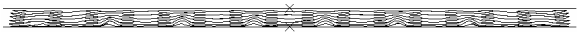

(g) Δ = 9.42mm, v = 20 m/s (t =0.7 ms)

Figure 5.1: Deformation of the GHS at the end of the dynamic analysis. (a) Δ = 1.44 mm, v = 1 m/s, t =3.15 ms; (b) Δ 2.57 mm, v = 1.25 m/s, t =1.25 ms; (c) Δ = 4.16 mm, v = 6 m/s, t =1.134 ms; (d) Δ = 5.47 mm, v = 9 m/s, t =0.97 ms; (e) Δ = 7.21 mm, v =1 3 m/s, t =0.88 ms; (f) Δ = 8.44 mm, v = 16 m/s, t =0.833 ms; (g) Δ = 9.42 mm, v = 20 m/s, t =0.7 ms

The dynamic analysis shows that the mathematical model presented in the Chapter 4 to calculate the collapse load and the locking strain for the GHS is correct and applicable to graded structures provided the maximum thickness to length ratio of cells falls under 0.25, and the impact velocities are low. In other words, equations 4.12 and 4.14 are valid for graded structures of long thin inclined cell walls under low strain rates.

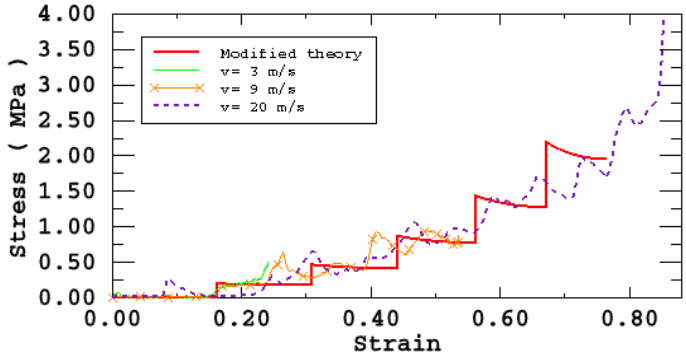


Figure 5.2: Dynamic stress-strain response of the GHS in the Y direction at different impact velocities

**5.3 GHS modes under high loading rates**

Figure 5.3 shows the deformation modes of the GHS at 30 m/s. The GHS undergoes an invariant 'I' mode for all high speed cases. However, unlike quasi static and low dynamic impact cases, deformation initiates from the proximal end followed by a new crushing front from the distal end. Figure 5.3a shows the deformation of the GHS after 24 μs . Deformation is localized in layer 6. Once the crushing is exhausted in layer 6, layers1-5 start to deform. It may be noted that deformation in this stage is homogenous in layers 1-5 as shown in Figure 5.3b. After 10 μs , deformation is completely localized in layer 1 as shown in Figure 5.3c and subsequent deformation follows the same pattern as that of quasi-static and low dynamic impact cases; the crushing front shifts from layer 1 to layer 2 and layer 2 to layer 3 and so forth.

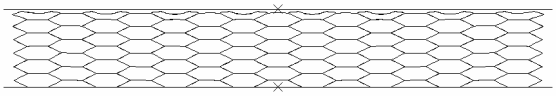

(a) Δ = 0.70 mm, (t =2.43 μs )

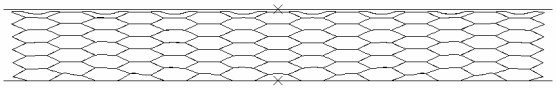

(b) Δ = 1.58 mm, (t =5.52 μs )

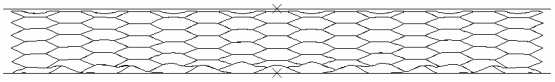

(c) Δ = 2.75 mm, (t =10.00 μs )

Figure 5.3: Deformation of the GHS at 30 m/s impact velocity. (a) Δ = 0.70 mm, (t =2.43 μs ); (b) Δ = 1.58 mm, (t =5.52 μs ); (c) Δ = 2.75 mm, (t =10.00 μs )

Figure 5.4 shows deformation modes for the GHS at 60 m/s impact velocity. Crushing initiates from the proximal end, and layers 6 and 5 are completely crushed before localized deformation enters the homogenous phase where the remaining intact layers undergo almost uniform deformation. Figure 5.4b shows the stage where crushing initiates from the distal end.

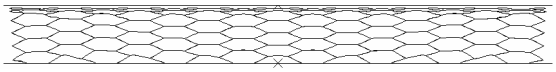

(a) Δ = 3.62 mm, (t =64.47 μs )

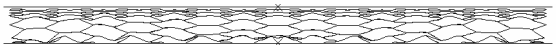

(b) Δ = 6.81 mm, (t =12.12 μs )

Figure 5.4: Deformation of the GHS at 60 m/s impact velocity. (a) Δ = 3.62 mm, (t =64.47 μs ); (b) Δ = 6.81 mm, (t =123.12 μs )

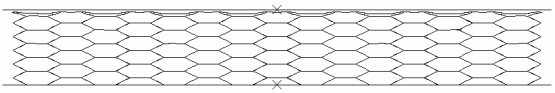

(a) Δ = 1.09 mm, (t =11.20 μs )

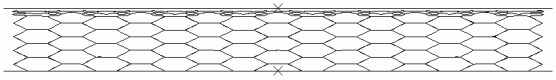

(b) Δ = 3.03 mm, (t =31.73 μs )

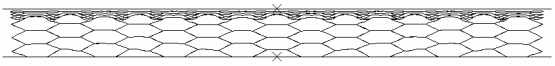

(c) Δ = 5.08 mm, (t =54.10 μs )

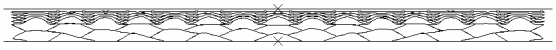

(d) Δ = 7.30 mm, (t =78.96 μs )

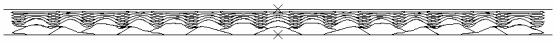

(e) Δ = 8.35 mm, (t =90.76 μs )

(f) Δ = 9.61 mm, (t =105.04 μs )

Figure 5.5: Deformation of the GHS at 100 m/s impact velocity. (a) Δ = 1.09 mm, (t =11.20 μs ); (b) Δ = 3.03 mm, (t =31.73 μs ); (c) Δ = 5.08 mm, (t =54.10 μs ); (d) Δ = 7.30 mm, (t =78.96 μs ); (e) Δ = 8.35 mm, (t =90.76 μs ); (f) Δ = 9.61 mm, (t =105.04 μs )

For impact velocities above 80 m/s, the homogeneous deformation phase and the second crushing front (at the distal end) were not observed. Figure 5.5 shows the deformation of the GHS at 100 m/s impact velocity. The GHS undergoes a completely reversed deformation

sequence. Layer 6 crushes first followed by layers 5, 4, 3, 2 and then 1, as compared to quasi-static and low dynamic impact cases.

### 5.4 Stress-strain curves for high impact velocity

Figure 5.6 shows the stress strain curves at 30, 60 and 100 m/s impact velocities for the GHS. The data is very noisy due to the fact that it was collected from the contact deceleration pulse of plate, A. The force pulse obtained from 'internal energy curve' integration, as was done in quasi-static and low dynamic impact cases, did not produce the actual force due to high artificial energy (energy consumed in hourglass control). Notwithstanding noisy data, the effect of a high loading rate in terms of a higher crushing strength is evident. Furthermore, Equation 4.14 does not hold true for these cases, and a new model needs to be developed to take into account the increase in crushing strength and a different sequence of deformation.

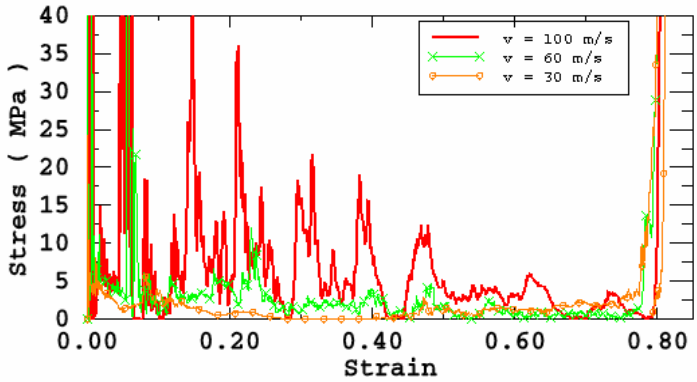


Figure 5.6: The stress-strain response of the GHS at 30, 60, and 100 m/s impact velocity

Comparing quasi-static and low dynamic impact cases with high dynamic impact cases, two important factors require explanation. First, the inertia of the GHS affects the overall response of the system, and, second, a stress wave is generated from the proximal end and propagates through the GHS. In quasi-static and low dynamic impact cases, the force on the support plate, B and the impact plate, A, is same. For high impact velocities, the force on the support plate, B, is larger than the force pulse on plate, A, by an amount equal to the mass times the acceleration of the GHS. This difference reflects the effect of the system inertia. Second, a high loading rate affects the propagation of the structural shock wave. When the stress-strain curve is convex toward the strain axis, the plastic wave travels with an increasing speed, resulting in a shock wave front. This plastic wave moves from layer to layer, deforming each layer to its final size and shape as it passes. Figure 5.7 shows the position of the precursor elastic wave and the plastic wave preceding the shock front as the deformation progresses.

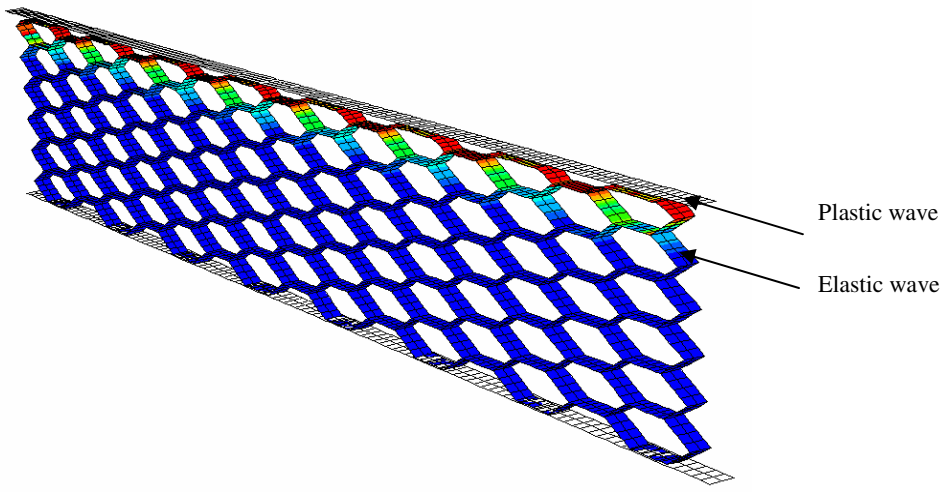


Figure 5.7: Propagation of precursor elastic and successor plastic wave

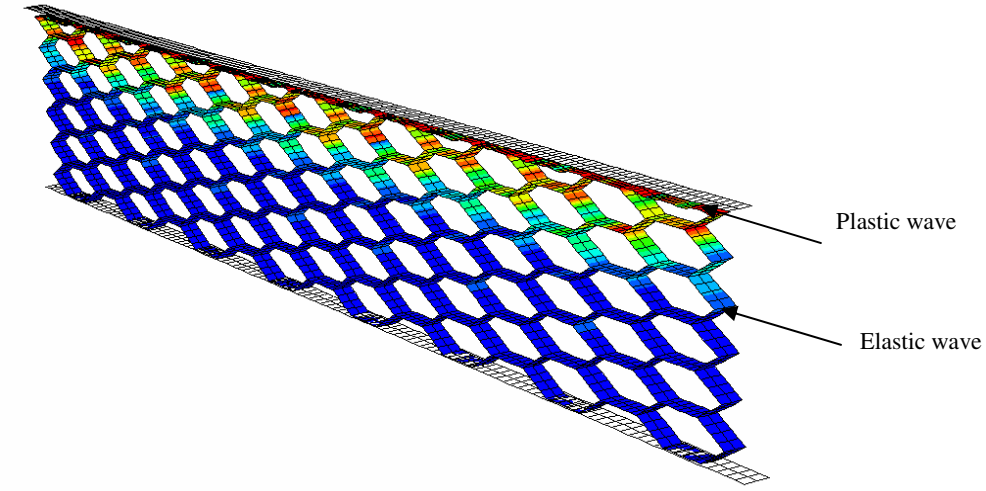


Figure 5.7 (Continued.)

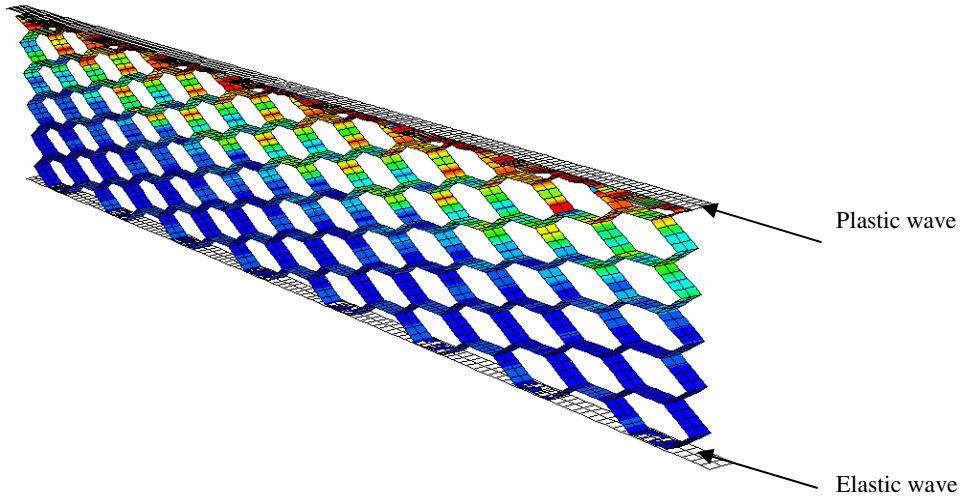


Figure 5.7 (Continued.)

### 5.5 Mathematical model for high velocity impact

As mentioned before, materials having convex stress-strain curves are prone to produce shocks under impact. Jahsman[56] used non-linear shock theory to model the behavior of synthetic foams under impact compression. Zarestsky and Ben-Dor[57] developed a model based upon a more complex theoretical stress-strain relationship for

polymeric foams. Reid et al.[53-54] analyzed a one dimensional ring system and developed an analytical model to predict the crushing strength and deflection. They used the plastic wave theory applied to the dynamic deformation of metal cylinders developed by Lee et al [58-59]. Due to the nature of the equations used in that model, a solution can only be achieved numerically [60]. Reid et al. [61], in another attempt to understand the behavior of wood, presented a model for low density cellular structures by assuming a rigid, perfectly plastic material. The model was further refined by D. Ruan et.al [51].The approach used by D. Ruan will be used as a starting point here to predict the behavior of the GHS under impact.

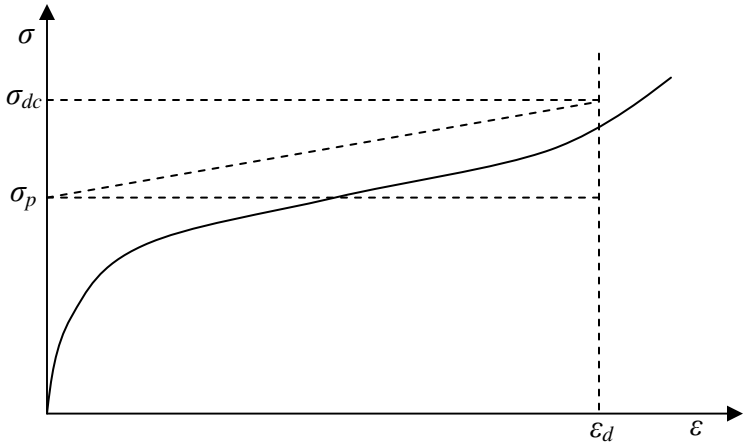


Figure 5.8: Typical stress-strain curve idealized as rigid, perfectly plastic, behavior followed by complete locking

Assume plate, A, hits the GHS of length '$l_0$' with velocity '$V_o$'. An idealized stress-strain curve is shown in Figure 5.8. As the plate hits the GHS, a shock wave is generated which travels along the 'Y' direction [62-64]. Downstream of this wave, the stress rises to '$\sigma_p$' while layers remain intact and at rest. Upstream of this wave front, the stress is '$\sigma_{dc}$' and the crushed portion moves with the instantaneous velocity of plate, A, this velocity decreases

with time as the deformation shifts to other layers. Figure 5.9 shows the stage of the crushing process at time‘t’.

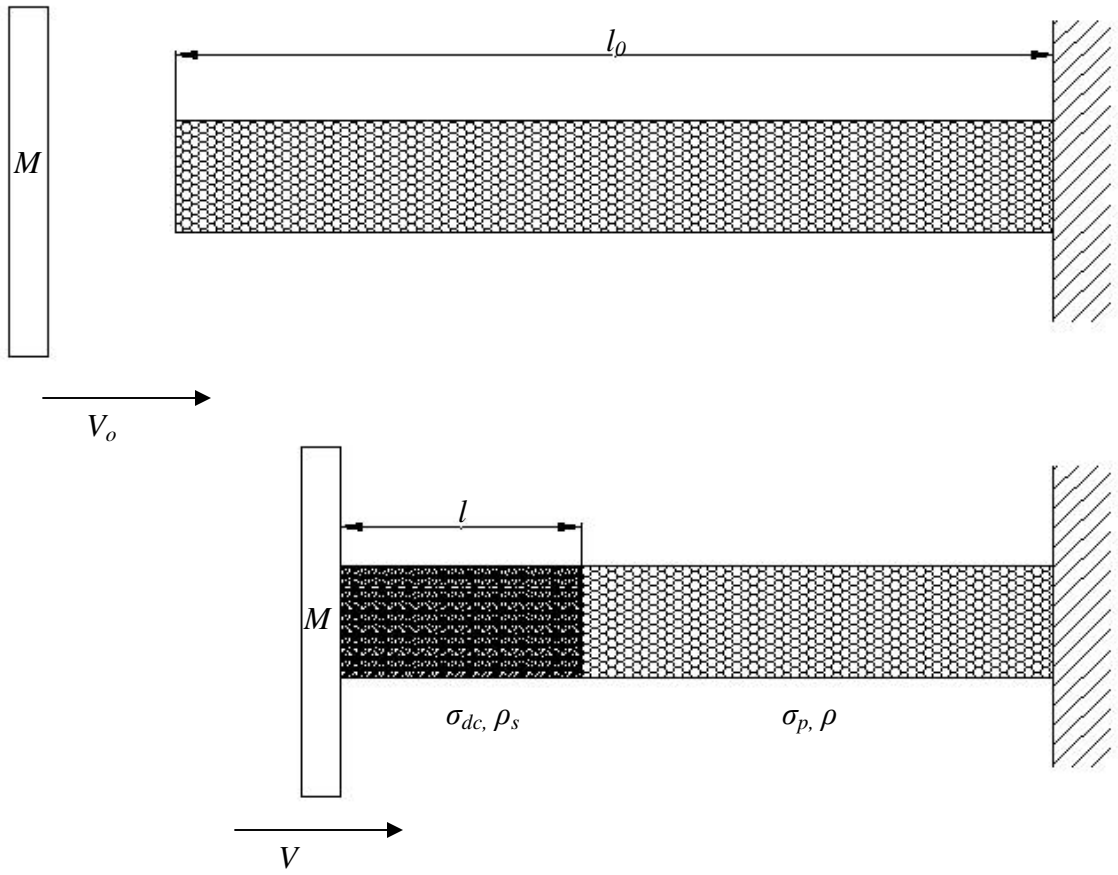


Figure 5.9: Sketch of a mass M impacting an initially stationary GHS

The energy of plate, A, just before impact is $0.5MV_0^2$.Where $M$ is the mass of the rigid plate, A. According to total energy conservation, the kinetic energy of rigid plate, A, will be equal to the kinetic energy of the rigid plate at time t plus the kinetic energy of the crushed portion of the GHS plus the energy consumed in plastic deformation.

$$0.5MV_0^2 = 0.5(\rho_s A' l + M)V^2 + \sigma_{dc} A' l \frac{\varepsilon_d}{1-\varepsilon_d} \qquad (5.1)$$

where A is the cross-sectional area of the GHS (assumed to be constant throughout the deformation process), *l* is the length of the crushed portion, *V* is the instantaneous velocity of plate, A, at time t, $\rho_s$ is the density of the material and $\varepsilon_d$ is the locking strain.

The plastic wave speed is given by

$$C_p = \sqrt{\frac{(\sigma_{dc} - \sigma_p)}{\varepsilon_d \rho}} \tag{5.2}$$

where $\rho$ is the cellular density of the GHS.

Conservation of momentum for an element at the wavefront for a time increment Δt requires that

$$(\sigma_{dc} - \sigma_p) A\Delta t = \rho_s A C_p \Delta t V$$

$$\sigma_{dc} = \sigma_p + \rho_s C_p V$$

$$\sigma_{dc} = \sigma_p + \frac{\rho_s (1-\varepsilon_d) V^2}{\varepsilon_d} \tag{5.3}$$

From equation 4.14

$$\sigma_{dc} = \sigma_p + \frac{\rho_s (1-\varepsilon_d)}{\varepsilon_d} \frac{(0.5MV_0^2 - \sigma_{dc} A' l \frac{\varepsilon_d}{1-\varepsilon_d})}{0.5(\rho_s A' l + M)} \tag{5.4}$$

The above equation shows that as *l* increases, $\sigma_{dc}$ decreases. For an initial crushing strength, *l* = 0, equation 5.4 reduces to

$$\sigma_{dc} = \sigma_p + \frac{\rho_s (1-\varepsilon_d)}{\varepsilon_d} V_0^2 \tag{5.5}$$

when $\rho_s = \frac{\rho}{1-\varepsilon_d}$ is substituted , Equation 5.5 reduces to

$$\sigma_{dc} = \sigma_p + \frac{\rho}{\varepsilon_d} V_0^2 \tag{5.6}$$

Then applying the putting plateau stress expression from equation 4.14, the above equation becomes

$$\sigma_{dc} = \frac{d^2}{2[c + l(\sin\phi + \delta\phi\cos\phi)](l-d)(\sin\phi + \delta\phi\cos\phi)} \sigma_y + \frac{\rho}{\varepsilon_d} V_0^2 \tag{5.7}$$

Hence, the crushing stress is influenced by the square of the impact velocity.

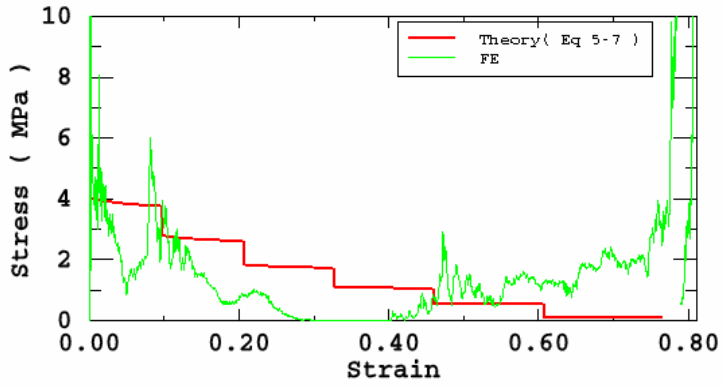


Figure 5.10 Comparison between theory and FE analysis at 30 m/s impact velocity

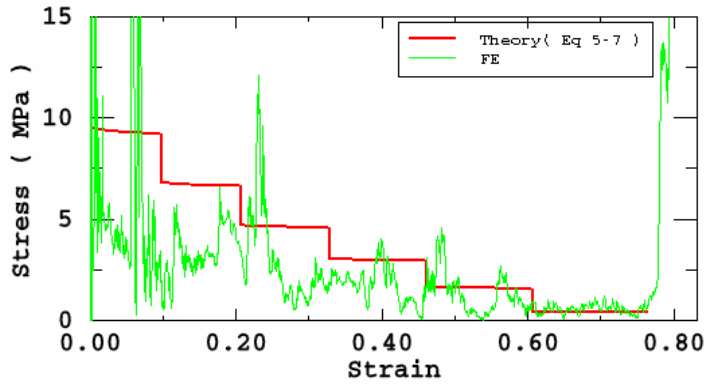


Figure 5.11 Comparison between theory and FE analysis at 60 m/s impact velocity

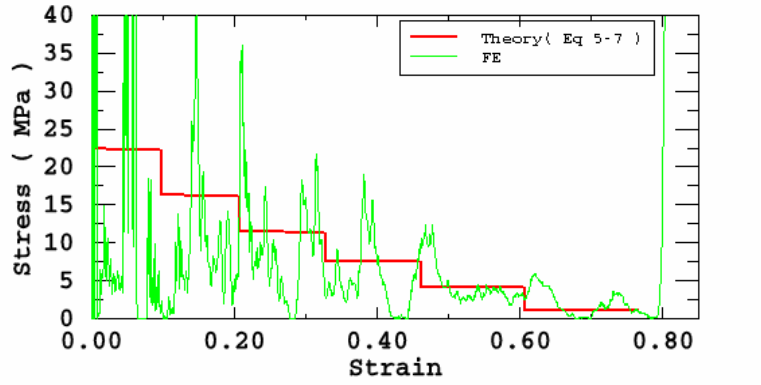


Figure 5.12 Comparison between theory and FE analysis at 100 m/s impact velocity

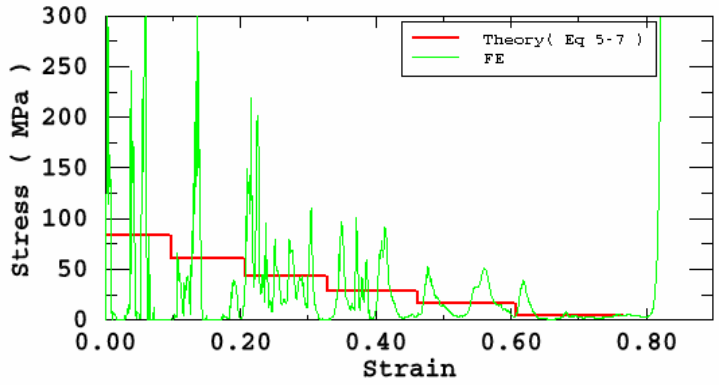


Figure 5.13 Comparison between theory and FE analysis at 200 m/s impact velocity

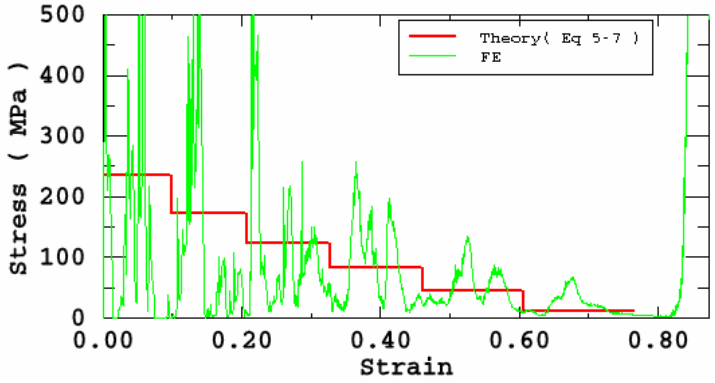


Figure 5.14 Comparison between theory and FE analysis at 340 m/s impact velocity

Figures 5.10-5.14 show the output of Equation 5.7 superimposed on the GHS stress-strain curves at 30, 60, 100, 200 and 350 m/s impact velocity, respectively. In spite of the noisy data, the plateau regimes are discernible. The increase in crushing strength and consistency of equation 5.7 for high impact velocities is also evident. The enhancement of the initial crush strength is due micro-inertial effect in which the cell walls undergo axial compression instead of bending and which, delays the primary deformation. The second phase of deformation, when the cell walls start bending and/or buckling, results in cell softening. Structures showing this type of behavior are called Type II structures [65-70]. For the medium impact velocity range where two crushing fronts appear with some degree of uniform global deformation of intact layers, Equation 5.7 requires modification. These modifications would depend on the understanding of the rationale of stress enhancement at a detailed level and the factors that cause the crushing front to shift from the distal end to the proximal end. This topic is under investigation and defines a pathway to future work.

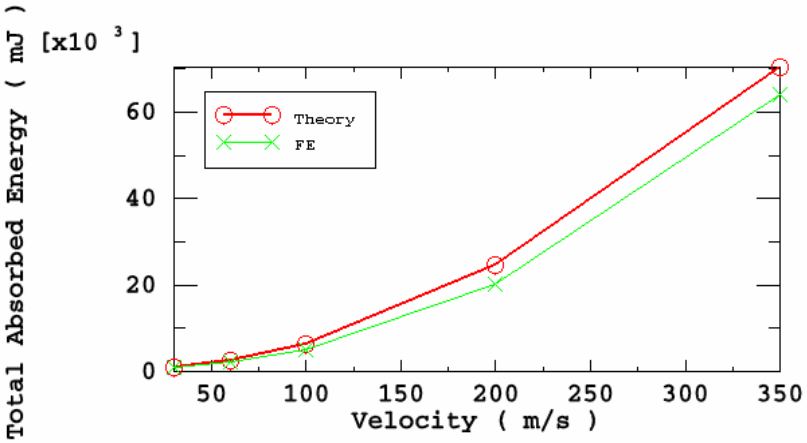


Figure 5.15: Total energy absorbed by the GHS at different impact velocities

Figure 5.15 depicts the comparison of total energy absorbed for the cases under discussion. The values are determined by integrating the 'Force vs. Displacement' curves. Shock theory overestimates the total energy as compared to the finite element simulation. However, it correctly captures the trend and pattern of the FE curve. The lower energy values in the simulation may be due to the noisy data and/or computational instability of the iteration process at the start and end of simulations.

### 5.6 Energy absorption performance of the GHS w.r.t regular honeycombs

The performance of the GHS was evaluated with respect to the regular honeycomb structure (RHS) under dynamic loading. The RHS had the same unit cell shape as that of the GHS with a constant wall thickness of 0.05 mm for all layers. The mechanical behavior of both structures is shown in Figure 5-16.

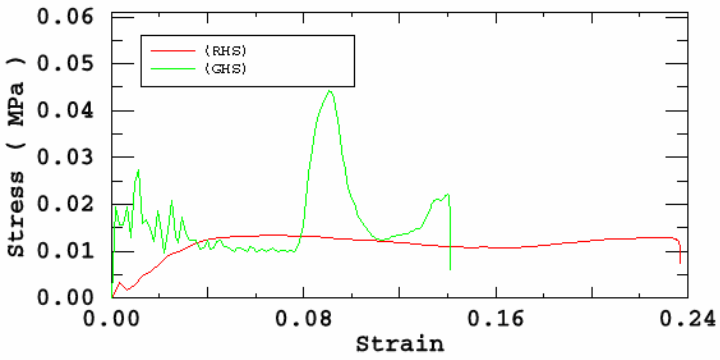


(a)

Figure 5.16: Comparison of the dynamic response of GHS and RHS in the Y direction (a) v = 1 m/s; (b) v = 3 m/s; (c) v = 6 m/s; (d) v = 9 m/s; (e) v = 20 m/s

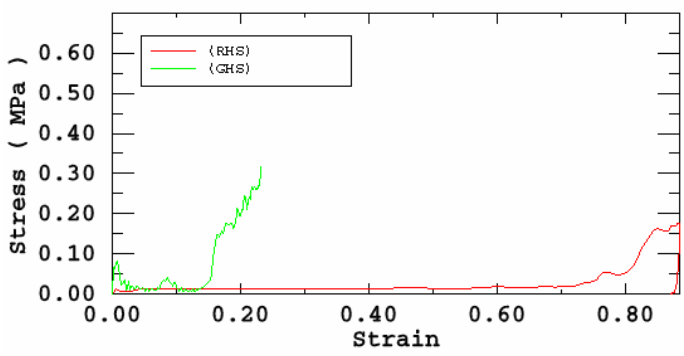


(b)

Figure 5.16 (Continued.)

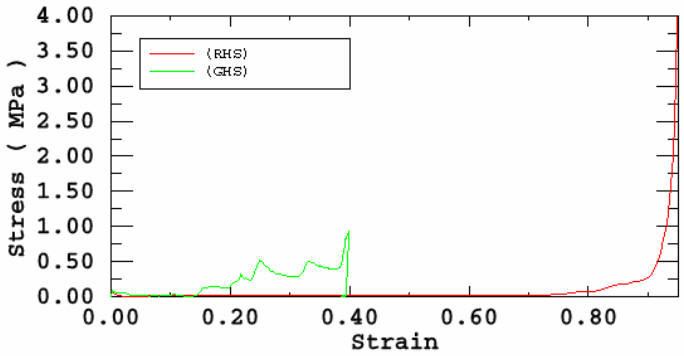


(c)

Figure 5.16 (Continued.)

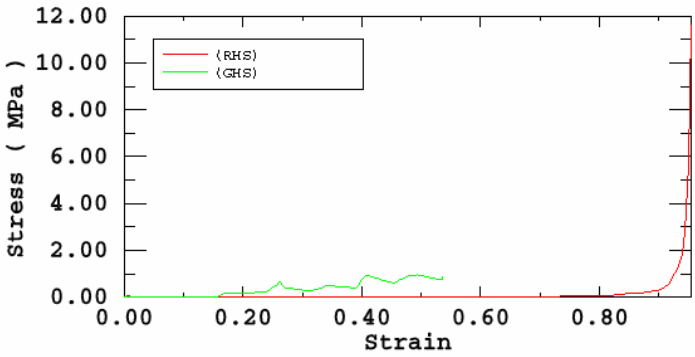


(d)

Figure 5.16 (Continued.)

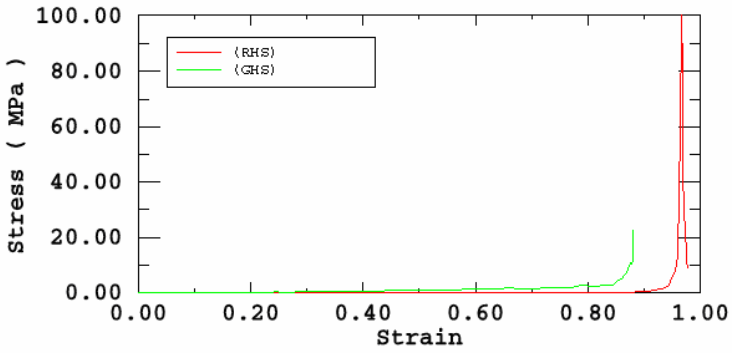


(e)

Figure 5.16 (Continued.)

At 1 m/s impact velocity, the stress on the rigid plate, B, of the RHS smoothly rises from an elastic to a plateau level of 0.012 MPa. For the GHS, the stress after an initial peak of 0.02 MPa stabilizes at roughly 0.01 MPa. At 0.08 strain, the lower inclined walls of the cells in layer 1 come in contact with rigid plate, B, and raise the stress to .044 MPa. This reduces to .013 MPa upon collapse of the upper inclined walls. At 3 m/s, the RHS is compromised at 0.85 strain, and afterwards the stress rises sharply. In the case of the GHS, an average stress of 0.02 MPa is maintained on rigid plate, B, until layer 2 starts deforming followed by layer 3. The collapse of layer 2 at 0.16 strain keeps the stress roughly at 0.2 MPa (see Figure 5.16b). As the impact velocity increases rigid plate, B, of the RHS, experiences higher and higher reactive stress at the end of the stroke. For the GHS, the stress level rises in steps. However, the rise in the stress levels remains very low as compare to the RHS (Figures 5.16c-e).

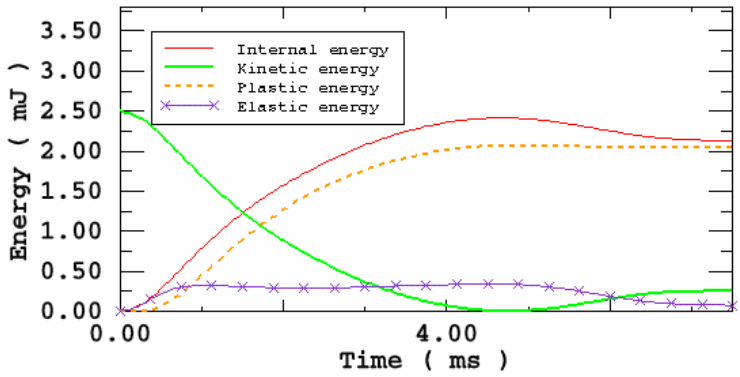


Figure 5.17: Energy curves of RHS at 1 m/s impact velocity

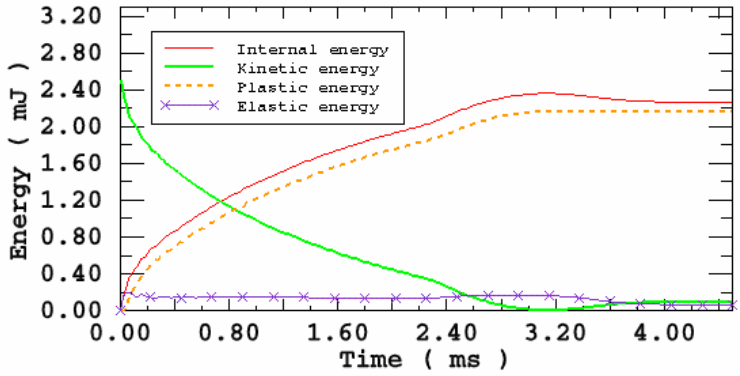


Figure 5.18: Energy curves of GHS at 1 m/s impact velocity

Figure 5.17 shows the kinetic, internal, elastic and plastic energy curves for the RHS at 1 m/s impact velocity. The structure absorbs 2.03 mJ of plastic energy and 0.34 mJ of elastic energy, of which, 77 % (0.264 mJ) is released to do negative work on the rigid plate, A, by the structure. The remaining elastic energy is trapped in the structure and reduces the rebound. The internal energy of the structure, which is equal to the sum of elastic, plastic and artificial energies, is 2.12 mJ at the end of the stroke. The rigid plate, A, comes to rest at 4.3 ms and rebounds with a velocity of 0.316 m/s (see Figure 5.19)

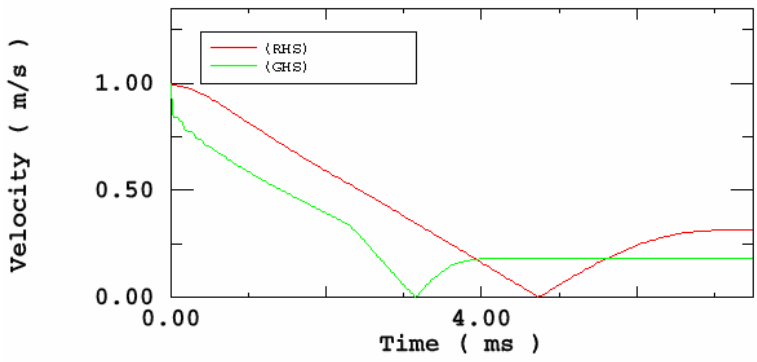


Figure 5.19: Velocity variation of the rigid plate 'A' in deforming the GHS and the RHS

The rigid plate, A, rebounds from the GHS at 3.2 ms with a velocity of 0.129 m/s, and the structure absorbs 2.32, 2.20 and 0.1 mJ of internal, plastic and elastic energies respectively as shown in Figure 5.17. In this case, 50% of the elastic energy is trapped in the structure. It can be seen that the rebound of the rigid plate, A, from GHS is almost 57% lower than from the RHS. The plastic energy absorbed by the GHS is 8% higher than the RHS whereas the elastic energy, which is directly responsible for the rebound, is almost 70% lower than the RHS. Table 5.1 lists the plastic energy and the rebound velocity of the RHS and the GHS for all the cases. Except for the 3 m/s impact velocity, the GHS absorbs more plastic energy than the RHS and produces a less severe retardation-acceleration transition phase to the rigid plate, A. Figure 5.20 shows plots relating the impact velocity and corresponding percentage of stroke utilized, for the RHS and the GHS. It can be seen that the RHS utilizes 85% stroke at a 3 m/s impact velocity. Any further increase in impact velocity produces a higher peak reactive force on the rigid plate, B, at the end of the deformation process. The GHS shows roughly a linear relationship between the impact velocity and the stroke until it reaches 20 m/s where the curve flattens out. This is because the structure has no room to deform any further.

Table 5.1: Rebound velocity and plastic energy of the RHS and the GHS for different impact velocities

| | RHS | | GHS | |
|---|---|---|---|---|
| Impact Velocity (m/s) | Plastic energy (mJ) | Rebound velocity (m/s) | Plastic energy (mJ) | Rebound velocity (m/s) |
| 1 | 2.03 | 0.316 | 2.20 | 0.183 |
| 3 | 20.84 | 0.457 | 19.98 | 0.644 |
| 6 | 85.25 | 1.083 | 84.57 | 0.798 |
| 9 | 143.00 | 4.280 | 193.00 | 1.059 |
| 13 | 368.00 | 4.640 | 410.00 | 1.174 |
| 16 | 525.00 | 6.723 | 622.00 | 1.211 |
| 20 | 769.00 | 9.570 | 956.00 | 2.792 |

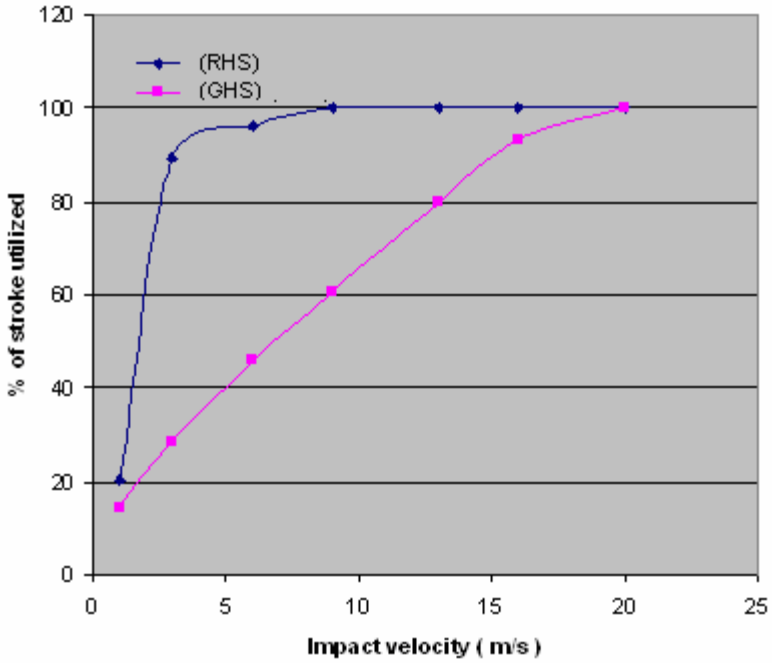


Figure 5.20: Utilization of stroke for different impact velocities

The direction of the grading is important from an application standpoint. If the GHS had to protect the rigid plate, A, then grading would have been opposite; i.e., bigger/soft cells would

have been on top (proximal end). That type of cell arrangement would eliminate the initial spike in the reactive force observed on rigid plate, A, in the FE analysis (Figure 5.21).

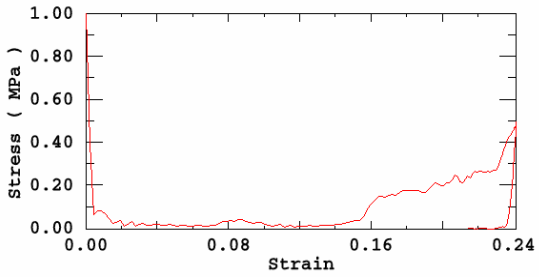


Figure 5.21: Stress on the rigid plate, A, of the GHS

**5.7 Cell shape**

To investigate the variation of the plateau stress and the locking strain with a shape change from a common hexagonal honeycomb cell to a banana peel cell, a program was written in MATLAB. The shape transformation was carried out by moving the inclined walls of a regular unit cell (l = c = 3mm, and $\phi = 30$) first in the X direction and then in the Y direction as shown in Figure 5.22. The output is presented in Figures 5.23-5.24. The curves for different wall thickness in Figure 5.23 show that as the angle, $\phi$, increases, the plateau stress decreases. However, the decrease in stress after $63^0$ is not that significant. Figure 5.24 shows the variation of the locking strain with respect to, $\phi$. The curves reveal a decrease in the locking strain with increasing, $\phi$, but the rate of decrease of locking strain with respect to '$\phi$' increases sharply after $63^0$. This short analysis shows that the cells in a banana peel collapse at lower loads without excessively sacrificing the stroke as well as the structural integrity.

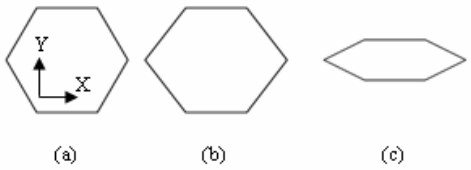


Figure 5.22: Transformation of the hexagonal honeycomb cell shape into a banana peel cell shape. (a) Regular cell; (b) Intermediate shape; (c) banana peel cell shape

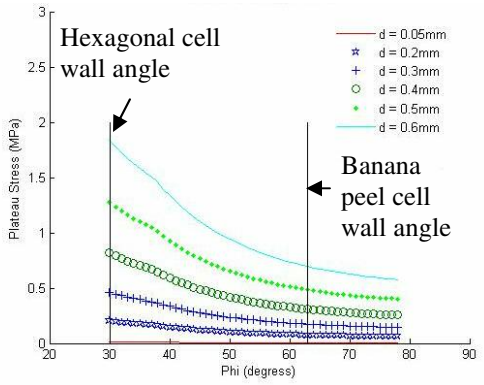


Figure 5.23: Variation of the plateau stress for different wall thickness and wall angle

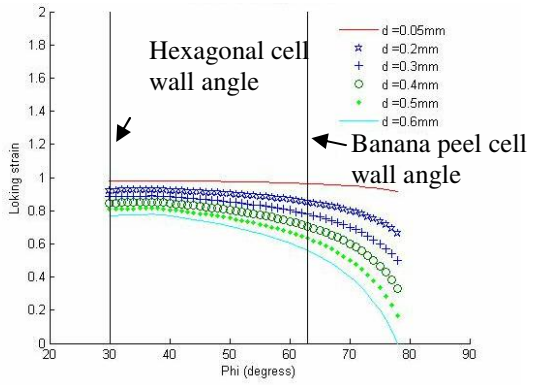


Figure 5.24: Variation of the locking strain for different wall thickness and wall angle

# CHAPTER 6. CONCLUSIONS AND FUTURE WORK

## 6.1 Conclusions

The graded structure in a banana peel acts as an energy absorber. The graded section exhibits superior energy absorption properties with respect to a solid section. The 'collapsing mechanism' of cells reduces the impact load substantially at the cost of a long stroke. The structure absorbs most of the kinetic energy in an irreversible form that results in a lower rebound and, consequently, a less severe retardation-acceleration phase. The material composition and cell size assist the 'collapse mechanism' to commence from the distal end which further mitigates collapse damages.

In comparison with regular honeycombs, the graded structure reacts to impact loads intelligently. The structure develops a balance among the stress/impact load, stroke and the structural integrity. When the foreign object (at low velocity) hits the structure, load is transferred to the least stiff layer on the distal end and 'the collapse mechanism' initiates from there. The crushing of cells keeps the stress constant. If the layer is completely crushed and the object still has energy to cause damage (to the object being protected) the next layer starts deforming. This extension of the crushing zone appears as a step rise in the plateau stress. When the second layer is collapsed completely, the crushing process shifts to the next layer and this process continues until either the object is completely stopped or the entire structure is compromised. This stepwise crushing process keeps the stress/load lower for a higher velocity range and consequently, provides a more flexible, space limited, operating environment than regular honeycombs with almost the same height. The irreversible plastic energy which is the major portion of the internal energy implicitly dictates the amount of

energy available for rebound. As the graded structure absorbs more plastic energy, the object undergoes a less severe retardation-acceleration phase as compared to regular honeycombs discussed in this research study. The linear relationship between the stroke and the impact velocity indicates that a graded structure wisely utilizes the stroke as the impact energy increases and neutralizes the impact before the end of the stroke. Furthermore, layers intact after the first hit provide protection in case of subsequent hits. This ensures reliability and repeatability. The slender cell shape in the graded packing produces a balance between functionality and compactness of the GHS. The arrangement of the inclined walls at $63^0$ results in more cells in a confined space and a lower plateau stress at the cost of little reduction in the locking strain. The theoretical expression derived for calculating crushing strength for regular honeycombs estimates lower values of the plateau stress for graded structures with respect to the FE analysis. The expression is revised by taking into account the large strain and plastic zone found in FE simulations. The modified model calculates a plateau stress which is consistent with FE results in the quasi-static analysis. It also gives a good approximation of the plateau stress for cases where dynamic effects are low.

Under high speed impact, a plastic shock wave traveling through the graded structure governs the collapsing mechanism. It passes through every layer compressing it to a final stage. The dynamic crushing strength of the graded structure is higher than the static crushing strength. The difference depends upon the impact velocity, mass of impact plate, mass and cellular density of the graded structure. A simple mathematical model based upon the findings of Reid *et al* on wood samples is presented. The model gives a good approximation for the dynamic plateau stress and correctly captures the form of the variation of total

absorbed energy with increasing dynamic effects. It, however, quantitatively overestimates the total absorbed energy.

### 6.2 Future Work

As discussed before, under medium dynamic loading two crushing fronts appear in the graded structure. One initiates from the distal end and the other from the proximal end. Furthermore, the uncrushed portion of the structure accelerates in the initial phase of crushing and decelerates as the crushing ends. An analytical model capturing this behavior of a graded structure is still under investigation. The velocity at which a graded structure changes mode (i.e., from single crushing front to two crushing fronts), and the critical velocity at which full locking is achieved are additional parameters that will be studied in future. The high speed analytical model based upon shock wave theory gives a good first order approximation of the increased crushing strength for a graded structure. However, it is not accurate enough to determine the behavior of a graded structure after full locking occurs since the rigid, perfectly plastic material model does not allow for reflection of the plastic wave from the fixed end. A bilinear or power hardening material model with the inclusion of a precursor elastic wave would likely give a better estimate of the crushing strength for the graded structure. Lastly, an experimental study of the graded structure for a range of velocities would certainly provide a useful benchmark to validate the analytical models and finite element results presented in this thesis.

# APPENDIX A

## A.1 Classical theory of plasticity (CTP)

The subject of CTP is used to explain the mathematical relationships, between stress and strain for plastically deformed materials; more generally called the constitutive equations of plastic deformation of metal and other selected engineering materials.

The four fundamental elements of CTP are given below

1) Yield strength

*The initial yield point of the material should be known since for stress values lower than this value deformation is linear and the correspondence between $\sigma$ and $\varepsilon$ is one to one. For stress values higher than the yield strength, the deformation is non-linear and history dependent. Generalized to the three-dimensional case, an initial yield surface should be known and can be written in the following form:*

$$F(\sigma,\sigma_Y^0) = 0 \qquad (a.1)$$

Where $\sigma_Y^0$ is the initial yield stress.

2) Yield surface

The growth of subsequent yield surfaces should be understood. In general, the yield strength is not a constant except for perfectly plastic materials or in the small region of plastic flow of mild steels. Thus the subsequent yield strength should be known. Generally

$$\sigma_{Y=}\sigma_Y(\alpha_i) \quad (I = 1,2,3\ldots..,n) \qquad (a.2)$$

Where $\alpha_{i,}$ I = 1, 2, 3,…,n, are all possible hardening parameters such as the equivalent plastic strain and internal variables. In one-dimensional problems, only one hardening

parameter is required to determine the stress strain curve in the plastic region. For example, the hardening parameter, $\alpha = \varepsilon_{P,}$ is enough to describe the loading case. According to the history dependent nature of the total $\varepsilon_{P,}$ it should be calculated by

$$\varepsilon_P = \varepsilon^p = \int d\varepsilon^p = \int \dot{\varepsilon} dt \tag{a.3}$$

From Figure A.1 it can be shown that

$$d\alpha = d\varepsilon^p = d\varepsilon - d\varepsilon^e = \frac{d\sigma}{E^t} - \frac{d\sigma}{E} = (\frac{1}{E^t} - \frac{1}{E}) d\sigma \tag{a.4}$$

and in rate form

$$\dot{\alpha} = (\frac{1}{E^t} - \frac{1}{E}) \dot{\sigma} \tag{a.5}$$

Where E is the Young's modulus and $E^t$ is the tangent modulus at a given stress level. In the case of linear hardening, $E^t$ is a constant, but in the general non-linear case shown in Figure A.1, $E^t$ is a function of stress and plastic strain:

$$E^t = E^t(\sigma, \varepsilon^P) \tag{a.6}$$

Then the general form of equation a.4 becomes

$$\dot{\alpha} = \dot{\alpha}(\sigma, \dot{\sigma}, \alpha) \tag{a.7}$$

$\dot{\alpha}$ needs to be a linear , homogeneous function of $\dot{\sigma}$ in order to describe the rate-independent behavior. Equation a.7 should be written as

$$\dot{\alpha} = \dot{\alpha}(\sigma, \dot{\sigma}) \alpha \tag{a.8}$$

or equivalently

$$d\alpha = \alpha_1(\sigma, \alpha^p) d\alpha \tag{a.9}$$

where $\alpha_1$ is a non-linear function of $\sigma$ and $\alpha$ and represents experimental observations. Equation a.9 can be generalized for the three –dimensional case as

$$\dot{\alpha}_i = \phi_i(\boldsymbol{\sigma}, \alpha_i) : \boldsymbol{\sigma} \qquad \text{(a10)}$$

or equivalently

$$d\alpha_i = \phi_i(\sigma, \alpha^p) : d\sigma \qquad \text{(a.11)}$$

where $\phi_i$ , i = 1, 2,…..,n, are second-,third-, or fourth-order tensor –valued functions of $\boldsymbol{\sigma}$ and $\alpha_i$, depending on whether $\alpha_i$ is a scalar, vector, or second-order tensor-valued hardening parameter. Equation a.10/a.11 is the evolution or constitutive equation for the hardening parameters, $\alpha_i$. Once the current values of the three hardening parameters are determined from the evolution equation a.10/a.11 by the stress path or history, they can be substituted into the expression of the yield surface to obtain the current or subsequent yield surface

$$F(\boldsymbol{\sigma},\alpha_i) = 0 \text{ ( I=1,2…..,n)} \qquad \text{(a.12)}$$

During elastic deformation no plastic deformation will occur, and the yield surface will remain unchanged, with

$$\alpha_i = 0$$

3) Constitutive equations for plastic deformation

The process of formulation of constitutive equations for plastic deformation is central to plasticity theory. These equations should be in rate or increment form because of path dependence and rate in-sensitivity. After some mathematical steps the following relationship can be obtained

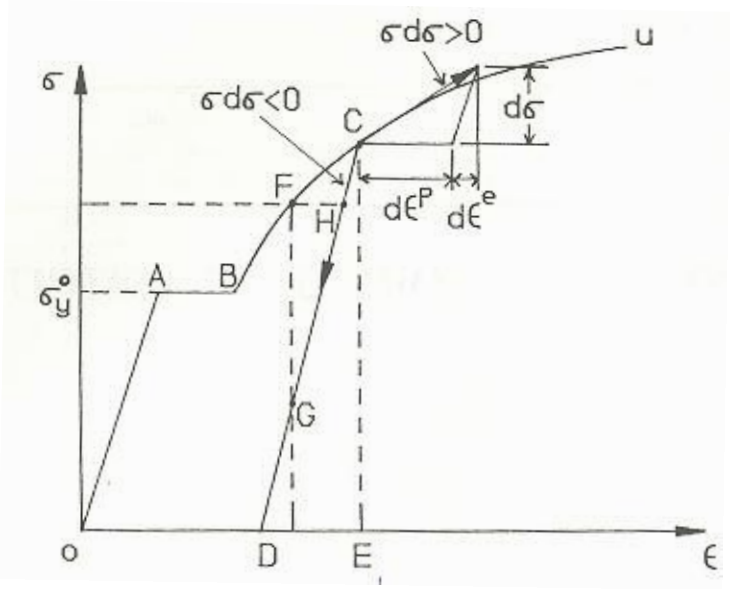


Figure A.1: Uniaxial true stress-strain curve [71]

The total strain rate is represented by

$$\dot{\varepsilon} = (\alpha^{p} + C^{-1}) : \dot{\sigma} \quad or \quad d\varepsilon = (\alpha^{p} + C^{-1}) : d\sigma \tag{a.13}$$

Inverting this relationship,

$$\dot{\sigma} = [\alpha^{p} + C^{-1}]^{-1} : \dot{\varepsilon} \quad or \quad d\sigma = [\alpha^{p} + C^{-1}]^{-1} : d\varepsilon \tag{a.14}$$

4) Loading-Unloading criteria

The loading –unloading criteria must be specified because the constitutive equations for hardening parameters and plastic strains are different for plastic loading and elastic loading and unloading. This is the main difference between nonlinear elasticity theory and plasticity theory. Therefore, to describe elastic-plastic behavior by the plasticity theory, it is necessary to identify the process as belonging to plastic loading or elastic unloading. Loading and unloading represent a deformation process starting from a plastic state and continuing to deform plastically and then returning to the elastic state and

continuing to deform plastically and then returning to the elastic region. A previous plastic state is always implied. For a hardening material under uniaxial loading, shown in Figure A.1, this means that the stress point is on the curve and satisfies the yield condition

$$\sigma_c - \sigma_Y(\varepsilon^p) = 0 \qquad \text{(a.15)}$$

Where $\sigma_c$ is the stress at point C (Figure A.1). The following equations represent the loading and unloading criterion:

$$d\sigma \geq 0 \quad \text{for loading} \qquad \text{(a.16)}$$

$$d\sigma \leq 0 \quad \text{for unloading} \qquad \text{(a.17)}$$

The four fundamental elements of plastic deformation discussed above constitute a theory of plasticity. Based on these elements material models like isotropic, kinematic or mixed hardening can be developed. Please read [71-77] for further details of those models.

# APPENDIX B

## B.1 Propagation velocity

Figure B.1 represents an element of a solid bar, of cross-sectional area A and density r, through which is propagating a stress wave. At the point x, the stress is s, but at a short distance, dx, further down the bar the stress is $(s+\frac{\partial u}{\partial x}dx)$. The strain in the element ε therefore equals

$$\frac{u+\frac{\partial u}{\partial x}\cdot dx-u}{\partial x}=\frac{\partial u}{\partial x} \qquad \text{(b.1)}$$

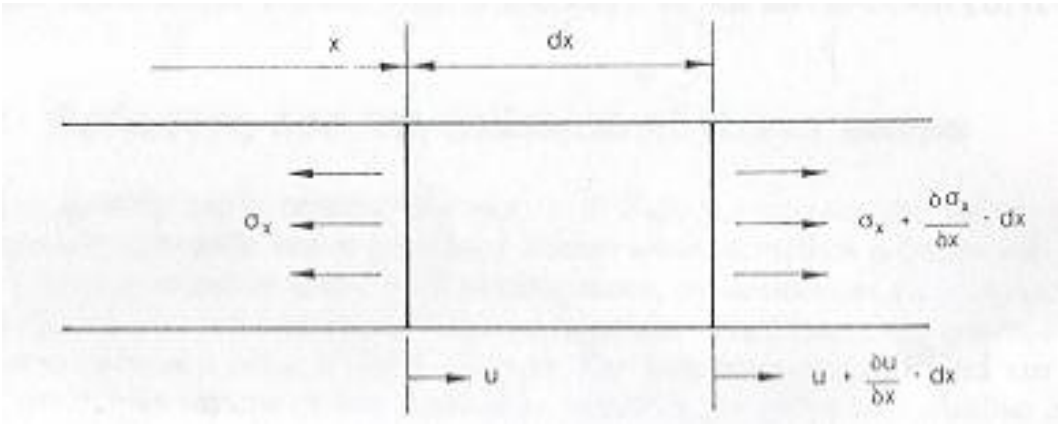


Figure B.1: Propagation of a stress wave in a solid bar [4]

Assuming that the bar remains within its elastic region in which σ=Eε, where E is Young's modulus for the material, the stress associated with the strain $\frac{\partial u}{\partial x}$ is $E\cdot\frac{\partial u}{\partial x}$

The resultant force on the element is $(A\frac{\partial \sigma}{\partial x}\cdot dx)$, which, on substitution from Equation b.1, becomes

$$AE\frac{\partial^2 u}{\partial x^2}dx \tag{b.2}$$

Newton's second law for the element gives

$$AE\frac{\partial^2 u}{\partial x^2}dx = \rho A dx.\frac{\partial^2 u}{\partial t^2} \tag{b.3}$$

i.e.,

$$\frac{\partial^2 u}{\partial t^2} = \frac{E}{\rho}\cdot\frac{\partial^2 u}{\partial x^2} \tag{b.4}$$

The solution for this equation is

$$u = a\sin b(x - \sqrt{\frac{E}{\rho}}\cdot t) \tag{b.5}$$

Where a and b are arbitrary constants. Equation b.5 describes the way in which the displacement u of a point varies with time and position. For example, if we take a 'snapshot' view at a particular value of t, u varies sinusoidally with x and similarly u varies sinusoidally with time at a particular location x. In order to determine how fast the wave is traveling, a relationship between x and t for a particular value of u is needed. For example, take the peak value for u. At this value u = a which requires that

$$b(x - \sqrt{\frac{E}{\rho}}\cdot t) = \frac{\pi}{2} + 2n\pi \qquad (\text{n = 1, 2……}) \tag{b.6}$$

Then

$$x = \frac{1}{b}(\frac{\pi}{2} + 2n\pi) + \sqrt{\frac{E}{\rho}}t \tag{b.7}$$

Therefore

$$\text{Speed of wave} = c = \frac{dx}{dt} = \sqrt{\frac{E}{\rho}} \tag{b.8}$$

**B.2 Particle velocity**

A compressive stress wave is suddenly applied to the left end of the bar of cross-sectional area A and density ρ. After time t, the wave front has traveled a distance of $\sqrt{E/\rho}\cdot t$ and after a time increment of $\delta t$, the extra distance traveled by the wave front is $\sqrt{E/\rho}\cdot\delta t$. The impulse delivered by a stress wave to the bar during this time increment is $\sigma A\delta t$. This impulse will cause an increase and in turn a change in moment of every particle in the region as shown in Figure B.2.

$$\sigma A\delta t = \text{m. } v = \rho A\sqrt{\frac{E}{\rho}\cdot\delta t\cdot v} \tag{b.9}$$

Where 'm' is the mass of the region and $v$ is the particle velocity acquired. So,

$$v = \frac{\sigma}{\sqrt{E\rho}} \tag{b.10}$$

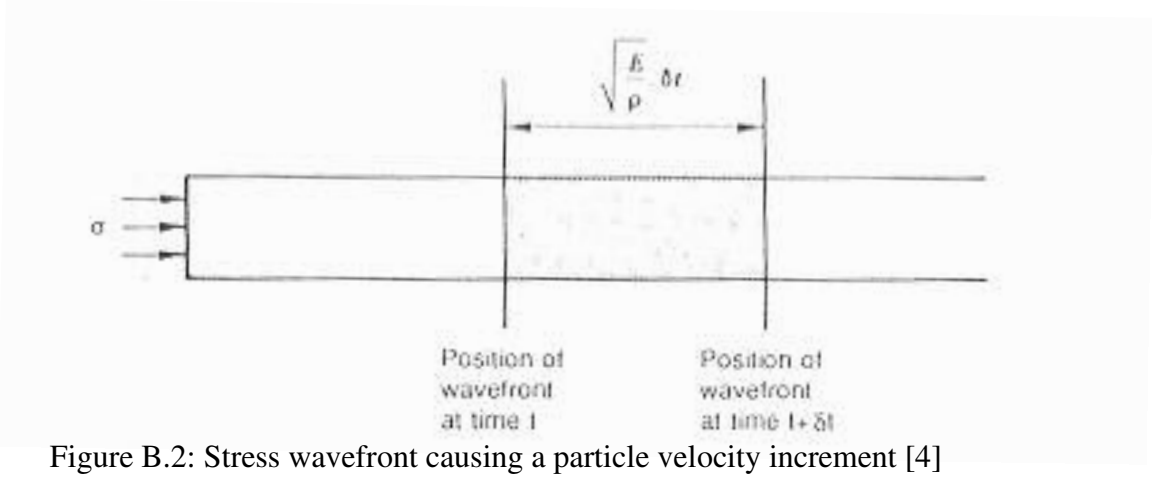


Figure B.2: Stress wavefront causing a particle velocity increment [4]

# APPENDIX C

## C.1 Effect of size on stiffness

In order to determine the effect of size on stiffness, a nine element 2D truss structure representing the shape of the cell found in a banana peel, was developed by writing finite element code in MATLAB. The output of that code with constant force is presented in Figures C.1-C.4.

Figure C.1 shows the variation in stiffness with respect to cell size. The cell size is expressed in terms of top or bottom (not used in code) element length. The length of the inclined element(s) is related to top or bottom element by a constant ratio found via raster image mapping. The figure shows that stiffness is inversely proportional to the size of the cell.

Figure C.2 shows the $10^{th}$ order polynomial curve approximating the stiffness-cell size curve. This numeric expression is useful if one wants to know how much the stiffness given the size of the cell.

Figure C.3 depicts almost a linear relationship between total nodal displacements of Nodes 2 and 3 in the Y direction versus the size of the cell. For small size, nodes 2 and 3 undergo smaller displacements. Under constant load the stiffness increases. Figure C.4 displays the effect of size on stiffness over the permissible cell size range.

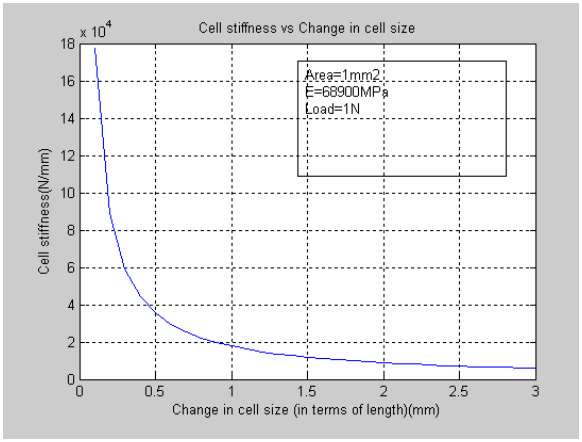


Figure C.1: Variation of cell stiffness w.r.t. cell size

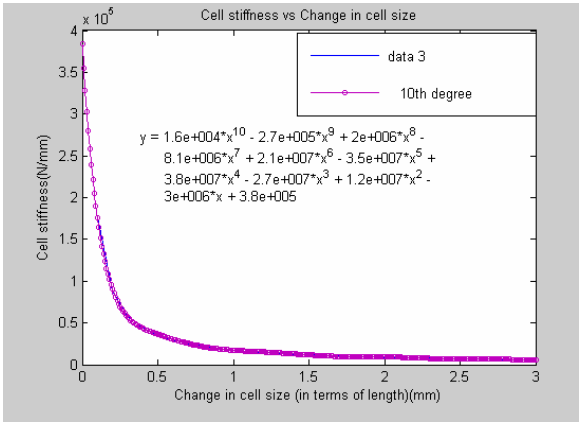


Figure C.2: $10^{th}$ order polynomial approximating stiffness vs. size curve

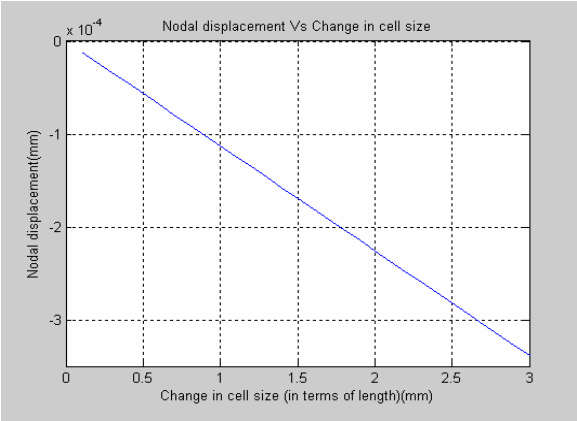


Figure C.3: Variation in nodal displacement w.r.t. cell size

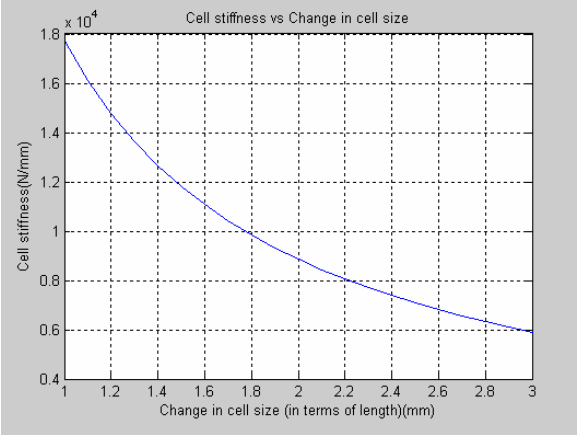


Figure C.4: Cell stiffness within the permissible cell size range

## C.2 MATLAB Code

```
clear all

close all

clc;

Length=3;
```

```
b=Length/1.5;

h=b;

g=1;

dL=0.1;

%Global loop for the whole program

while (Length>0)

%*********%define paramters*********%

%node 1 co-ordinates

x(1)=Length;

y(1)=0;

%node 2 co-ordinates

x(2)=Length+h;

y(2)=b/2;

%node 3 co-ordinates

x(3)=Length;

y(3)=b;

%node 4 co-ordinates

x(4)=0;

y(4)=b;

%node 5 co-ordinates

x(5)=0-h;

y(5)=b/2;

%node 5 co-ordinates

x(6)=0;

y(6)=0;
```

```
%calculate the length of elements
    for i=1:5
        Le(i) = sqrt((x(i+1)-x(i))^2+(y(i+1)-y(i))^2);
    end
%CENETERAL ELEMENTS LENGTHS
Le(6) = sqrt((x(2)-x(6))^2+(y(2)-y(6))^2);
Le(7) = sqrt((x(3)-x(6))^2+(y(3)-y(6))^2);
Le(8) = sqrt((x(4)-x(1))^2+(y(4)-y(1))^2);
Le(9) = sqrt((x(5)-x(1))^2+(y(5)-y(1))^2);
%define the area
A=1;
%define material properties
E=68900;
%***************develop element stiffness matrix**************%
%Develop direction cosines L and M for elements
for i=1:5
    L(i)=(x(i+1)-x(i))/Le(i);
    M(i)=(y(i+1)-y(i))/Le(i);
end
%initialize the 'Ke'array
for i=1:4
    for j=1:12
        for k=1:12
            Ke(i,j,k)=0;
        end
```

```
    end
end
%DEVELOP DIRECTION COSINES L AND M FOR CENTRAL ELEMENTS
  L(6)=(x(2)-x(6))/Le(6);
  M(6)=(y(2)-y(6))/Le(6);

  L(7)=(x(3)-x(6))/Le(7);
  M(7)=(y(3)-y(6))/Le(7);

  L(8)=(x(4)-x(1))/Le(8);
  M(8)=(y(4)-y(1))/Le(8);

  L(9)=(x(5)-x(1))/Le(9);
  M(9)=(y(5)-y(1))/Le(9);
%Element Stiffness Matrix
for i=1:9
            Ke(i,1,1)=  (A*E/Le(i))*  L(i)^2    ;
            Ke(i,1,2)=  (A*E/Le(i))*  L(i)*M(i) ;
            Ke(i,1,3)=  (A*E/Le(i))* -L(i)^2    ;
            Ke(i,1,4)=  (A*E/Le(i))* -L(i)*M(i) ;
            Ke(i,2,1)=  (A*E/Le(i))*  L(i)*M(i) ;
            Ke(i,2,2)=  (A*E/Le(i))*  M(i)^2    ;
            Ke(i,2,3)=  (A*E/Le(i))* -L(i)*M(i) ;
            Ke(i,2,4)=  (A*E/Le(i))* -M(i)^2    ;
            Ke(i,3,1)=  (A*E/Le(i))* -L(i)^2    ;
```

```
            Ke(i,3,2)=  (A*E/Le(i))* -L(i)*M(i) ;
            Ke(i,3,3)=  (A*E/Le(i))*  L(i)^2    ;
            Ke(i,3,4)=  (A*E/Le(i))*  L(i)*M(i) ;
            Ke(i,4,1)=  (A*E/Le(i))* -L(i)*M(i) ;
            Ke(i,4,2)=  (A*E/Le(i))* -M(i)^2    ;
            Ke(i,4,3)=  (A*E/Le(i))*  L(i)*M(i) ;
            Ke(i,4,4)=  (A*E/Le(i))*  M(i)^2    ;
end
%develop global stiffness matrix
K = zeros(12);
for i=1:4
    for j=1:4
        K(i,j)=Ke(1,i,j);
    end
end

for i=3:6
    for j=3:6
        K(i,j)=Ke(1,i,j)+Ke(2,i-2,j-2);
    end
end

for i=5:8
    for j=5:8
        K(i,j)=Ke(2,i-2,j-2)+Ke(3,i-4,j-4);
```

```
    end
end

for i=7:10
    for j=7:10
        K(i,j)=Ke(3,i-4,j-4)+Ke(4,i-6,j-6);
    end
end

for i=9:12
    for j=9:12
        K(i,j)=Ke(4,i-6,j-6)+Ke(5,i-8,j-8);
    end
end
%FILL THE GLOBAL STIFFNESS MATRIX FOR CENTRAL ELEMENTS
%ELEMENT 6
K(11,11)= K(11,11)+Ke(6,1,1);    K(11,12)= K(11,12)+Ke(6,1,2);
K(11,3) = K(11,3)+Ke(6,1,3);    K(11,4) = K(11,4)+Ke(6,1,4);
K(12,11)= K(12,11)+Ke(6,2,1);    K(12,12)= K(12,12)+Ke(6,2,2);
K(12,3) = K(12,3)+Ke(6,2,3);    K(12,4) = K(12,4)+Ke(6,2,4);
K(3,11) = K(3,11) +Ke(6,3,1);    K(3,12) = K(3,12) +Ke(6,3,2);
K(3,3)  = K(3,3) +Ke(6,3,3);    K(3,4)  = K(3,4) +Ke(6,3,4);
K(4,11) = K(4,11) +Ke(6,4,1);    K(4,12) = K(4,12) +Ke(6,4,2);
K(4,3)  = K(4,3) +Ke(6,4,3);    K(4,4)  = K(4,4) +Ke(6,4,4);
```

```
%ELEMENT 7
K(11,11)= K(11,11)+Ke(7,1,1);    K(11,12)= K(11,12)+Ke(7,1,2);
K(11,5) = K(11,5)+Ke(7,1,3);     K(11,6) = K(11,6)+Ke(7,1,4);
K(12,11)= K(12,11)+Ke(7,2,1);    K(12,12)= K(12,12)+Ke(7,2,2);
K(12,5) = K(12,5)+Ke(7,2,3);     K(12,6) = K(12,6)+Ke(7,2,4);
K(5,11) = K(5,11) +Ke(7,3,1);    K(5,12) = K(5,12) +Ke(7,3,2);
K(5,5)  = K(5,5) +Ke(7,3,3);     K(5,6)  = K(5,6) +Ke(7,3,4);
K(6,11) = K(6,11) +Ke(7,4,1);    K(6,12) = K(6,12) +Ke(7,4,2);
K(6,5)  = K(6,5) +Ke(7,4,3);     K(6,6)  = K(6,6) +Ke(7,4,4);

%ELEMENT 8
K(1,1)  = K(1,1)+Ke(8,1,1);      K(1,2)  = K(1,2)+Ke(8,1,2);
K(1,7)  = K(1,7)+Ke(8,1,3);      K(1,8)  = K(1,8)+Ke(8,1,4);
K(2,1)  = K(2,1)+Ke(8,2,1);      K(2,2)  = K(2,2)+Ke(8,2,2);
K(2,7)  = K(2,7)+Ke(8,2,3);      K(2,8)  = K(2,8)+Ke(8,2,4);
K(7,1)  = K(7,1)+Ke(8,3,1);      K(7,2)  = K(7,2)+Ke(8,3,2);
K(7,7)  = K(7,7)+Ke(8,3,3);      K(7,8)  = K(7,8)+Ke(8,3,4);
K(8,1)  = K(8,1)+Ke(8,4,1);      K(8,2)  = K(8,2)+Ke(8,4,2);
K(8,7)  = K(8,7)+Ke(8,4,3);      K(8,8)  = K(8,8)+Ke(8,4,4);

%ELEMENT 9
K(1,1)  = K(1,1) +Ke(9,1,1);     K(1,2)  = K(1,2) +Ke(9,1,2);
K(1,9)  = K(1,9) +Ke(9,1,3);     K(1,10) = K(1,10) +Ke(9,1,4);
K(2,1)  = K(2,1) +Ke(9,2,1);     K(2,2)  = K(2,2) +Ke(9,2,2);
K(2,9)  = K(2,9) +Ke(9,2,3);     K(2,10) = K(2,10) +Ke(9,2,4);
```

```
K(9,1)  = K(9,1) +Ke(9,3,1);     K(9,2)  = K(9,2) +Ke(9,3,2);
K(9,9)  = K(9,9) +Ke(9,3,3);    K(9,10) = K(9,10) +Ke(9,3,4);
K(10,1) = K(10,1)+Ke(9,4,1);     K(10,2) = K(10,2)+Ke(9,4,2);
K(10,9) = K(10,9)+Ke(9,4,3);    K(10,10)= K(10,10)+Ke(9,4,4);
%develop reduced stiffness matrix
 Kr = K(3:10,3:10);
% Krr = K(6:8,6:8);
f4=1;
f5=1;
%develop element force vector
F=[0;0;0;-f4;0;-f5;0;0];
X(:,g) =(inv(Kr)*F);
Length=Length-dL;
b=Length/1.5;
h=b;
g=g+1;
end
z=[-3:dL:-.1];
 figure (1)
 subplot(2,2,1)
 plot(-z,(-(X(4,:)+X(2,:))/(f4+f5)).^-1);
 grid;
 title('Cell stiffness vs Change in cell size');
 xlabel('Change in cell size (in terms of length)(mm)');
 ylabel('Cell stiffness(N/mm)');
```

```
%legend('Q3','Q4','Q5','Q6');
%figure (2)
subplot(2,2,2)
plot(-z,(X(4,:)+X(2,:)));
grid;
title('Nodal displacement Vs Change in cell size');
xlabel('Change in cell size (in terms of length)(mm)');
ylabel('Nodal displacement(mm)');
 subplot(2,2,3)
plot(-z,(-(X(4,:)+X(2,:))/(f4+f5)).^-1);
%grid;
title('Cell stiffness vs Change in cell size');
xlabel('Change in cell size (in terms of length)(mm)');
ylabel('Cell stiffness(N/mm)');


subplot(2,2,4)
plot(-z,(-(X(4,:)+X(2,:))/(f4+f5)).^-1);
grid;
title('Cell stiffness vs Change in cell size');
xlabel('Change in cell size (in terms of length)(mm)');
ylabel('Cell stiffness(N/mm)');

figure(2)
Length=3;
```

```
 b=Length/1.5;
 h=b;
%node 1 co-ordinates
 x1=Length;
 y1=0;
%node 2 co-ordinates
 x2=Length+h;
 y2=b/2;
%node 3 co-ordinates
 x3=Length;
 y3=b;
%node 4 co-ordinates
 x4=0;
 y4=b;
%node 5 co-ordinates
 x5=0-h;
 y5=b/2;
%node 5 co-ordinates
 x6=0;
 y6=0;

 XX1 =[x1 x2];
 YY1 =[y1 y2];

 XX2 =[x2 x3];
```

```
YY2 =[y2 y3];


XX3 =[x3 x4];

YY3 =[y3 y4];


XX4 =[x4 x5];

YY4 =[y4 y5];


XX5 =[x5 x6];

YY5 =[y5 y6];

plot(XX1,YY1,XX2,YY2,XX3,YY3,XX4,YY4,XX5,YY5);
```

# APPENDIX D

## D.1 Explicit method

Analytical solutions of the equations of motion are not possible if the excitation changes arbitrarily or the system is nonlinear. In such situations, numerical integration methods are useful. Numerical integration methods are used to solve differential equations using small time steps, explicitly or implicitly. Both dynamic and static problems can be solved by explicit or implicit methods.

The differences between the explicit and implicit methods make them suitable for different situations. Explicit methods use less memory (storage) and have low computational cost over implicit methods because

- Explicit methods use diagonal, lumped mass matrices so that the system to be solved is uncoupled
- In explicit methods, no equilibrium iterations like Newton- Raphson are needed

The convergence problems that arise in implicit methods can be avoided using explicit methods; however, stability could be an issue. Implicit methods are suitable for high-speed dynamic and non-linear analysis such as crash simulations.

## D.2 Central difference method

As explained earlier in the section 3.3, ABAQUS uses a central difference method to solve differential equations numerically. Equilibrium is expressed at an instant where displacements are known. Using this information, new equilibrium data is calculated for the next time step. The implication of the method is that known information between the

previous time step and the current one are used to calculate equilibrium for the current time step. The solution of second order equation of motion is presented below

The equation of motion can be written as

$$m\ddot{u}_i + c\dot{u}_i + ku_i = p_i \tag{d.1}$$

Where m , c and k are mass, damping and stiffness constant respectively. $p$ is an applied force vector, and $u$, $\dot{u}$ and $\ddot{u}$ are displacement, velocity and acceleration vectors respectively. For the next step the equation becomes:

$$m\ddot{u}_{i+1} + c\dot{u}_{i+1} + ku_{i+1} = p_{i+1} \tag{d.2}$$

This method is based on a finite difference approximation of the time derivatives of displacement ( $\dot{u}$ and $\ddot{u}$ .) Taking constant time steps, $\Delta t_i = \Delta t$ , the central difference expression for velocity and acceleration at time i are

$$\dot{u}_i = \frac{\dot{u}_{i+1} - \dot{u}_{i-1}}{2\Delta t} \tag{d.3}$$

$$\ddot{u}_i = \frac{\dot{u}_{i+1} - 2u_i + \dot{u}_{i-1}}{(\Delta t)^2} \tag{d.4}$$

Putting these approximate velocity and acceleration expressions into Equation d.1gives

$$m\frac{\dot{u}_{i+1} - 2u_i + \dot{u}_{i-1}}{(\Delta t)^2} + c\frac{\dot{u}_{i+1} - \dot{u}_{i-1}}{2\Delta t} + ku_i = p_i \tag{d.5}$$

In this equation $u_i$ and $u_{i-1}$ are known from the last step. Rearrangement of equation d.5 by transferring unknown quantities on right hand side gives

$$\left[\frac{m}{(\Delta t)^2} + \frac{c}{2\Delta t}\right]u_{i+1} = p_i - \left[\frac{m}{(\Delta t)^2} - \frac{c}{2\Delta t}\right]u_{i-1} - \left[k - \frac{2m}{(\Delta t)^2}\right]u_i \tag{d.6}$$

or

$$\hat{k}u_{i+1} = \hat{p}_i \quad \Rightarrow \quad u_{i+1} = \hat{p}_i.\hat{k}^{-1} \tag{d.7}$$

The solution for $u_{i+1}$ at time i+1 is determined from the information at time i without using equilibrium, Equation d.2, at time i+1. Such a method is called an explicit method. Other methods used in numerical integration are theta, Wilson theta and Newmark method etc.

As can be seen during the time step, the velocity and acceleration remain constant, error (as well stability) caused by this approximation directly depends upon the size of the time step. In ABAQUS, additional error will appear if the time step is larger than the time for a dilatational wave to cross any of the elements. If the error goes in to an unbounded phase, simulation stops. Hence the mesh density plays an important role in the stability of a solution and the computational cost. Smaller element sizes lead to smaller time steps thus a large number of increments and a higher computational cost [22, 78].

# APPENDIX E

## E.1 Contact pair

ABAQUS/Standard defines contact between two bodies in terms of two surfaces that may interact; these surfaces are called a “contact pair.” ABAQUS/Standard defines “self-contact” in terms of a single surface.

The order in which the two surfaces are specified on the contact pair option is critical because of the manner in which surface interactions are discretized. For each node on the first surface (the “slave” surface) ABAQUS/Standard attempts to find the closest point on the second surface (the “master” surface) of the contact pair where the master surface's normal passes through the node on the slave surface as shown in Figure E.1 . The interaction is then discretized between the point on the master surface and the slave node.

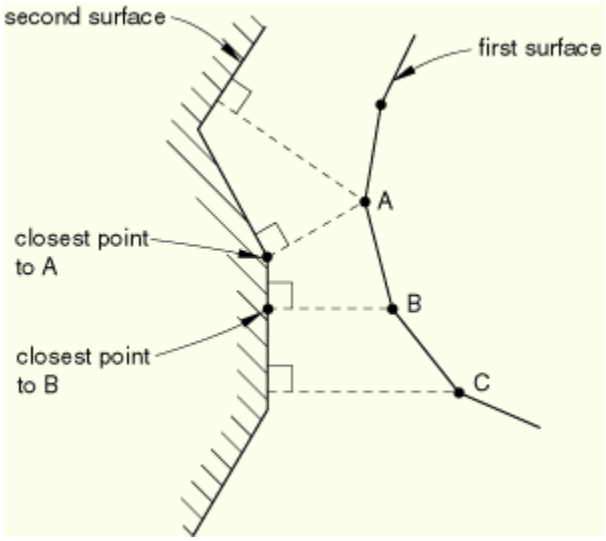


Figure E.1: Methodology of finding the contact node on the slave surface [22]

Slave surfaces must always be attached to deformable bodies. Rigid surfaces must always be the master surface in the contact pair. Both surfaces in a contact pair cannot be rigid surfaces. A node-based surface must always be the slave surface.

### E.2 Constraint enforcement method

The contact formulation for the contact pair algorithm in ABAQUS implements two types of constraint enforcing methods, kinematic and penalty.

#### E.2.1 Kinematic contact constraints

The kinematic method enforces strict contact conditions e.g. no penetration is allowed. In a pure master-slave contact, in each increment of the analysis ABAQUS/Explicit first advances the kinematic state of the model into a predicted configuration without considering the contact conditions. ABAQUS/Explicit then determines which slave nodes in the predicted configuration penetrate the master surface. The depth of each slave node's penetration, the mass associated with it, and the time increment are used to calculate the resisting force required to oppose penetration. For hard contact, this is the force which, had it been applied during the increment, would have caused the slave node to exactly contact the master surface. The next step depends on the type of master surface used.

- When the master surface is formed by element faces, the resisting forces of all the slave nodes are distributed to the nodes on the master surface. The mass of each contacting slave node is also distributed to the master surface nodes and added to their mass to determine the total inertial mass of the contacting interfaces.

ABAQUS/Explicit uses these distributed forces and masses to calculate an acceleration correction for the master surface nodes. Acceleration corrections for the slave nodes are then determined using the predicted penetration for each node, the time increment, and the acceleration corrections for the master surface nodes. ABAQUS/Explicit uses these acceleration corrections to obtain a corrected configuration in which the contact constraints are enforced.

- In the case of an analytical rigid master surface, the resisting forces of all slave nodes are applied as generalized forces on the associated rigid body. The mass of each contacting slave node is added to the rigid body to determine the total inertial mass of the contacting interfaces. The generalized forces and added masses are used to calculate an acceleration correction for the analytical rigid master surface. Acceleration corrections for the slave nodes are then determined by the corrected motion of the master surface [22]

The kinemetic method for other types of surface pairs is beyond the scope of this report . Please consult ABAQUS theory manual for further details [22]

**E.2.2 Penalty contact constraints**

The penalty contact results in less stringent enforcement of contact constraints than the kinematic contact method, but the penalty method allows for treatment of more general types of contact (for example, contact between two rigid bodies). When the penalty method is chosen for enforcing contact constraints in the normal direction, it is also used to enforce sticking friction. Since the penalty algorithm introduces additional stiffness behavior into a model, this stiffness can influence the stable time increment. ABAQUS/Explicit

automatically accounts for the effect of the penalty stiffnesses in the automatic time incrementation, although this effect is usually small.

In a pure master-slave contact, the penalty contact algorithm searches for slave node penetrations in the current configuration. Contact forces that are a function of the penetration distance are applied to the slave nodes to oppose the penetration, while equal and opposite forces act on the master surface at the penetration point. When the master surface is formed by element faces, the master surface contact forces are distributed to the nodes of the master faces being penetrated. In the case of an analytical rigid master surface, the master surface forces are applied as forces and moments on the associated rigid body.

The “spring” stiffness that relates the contact force to the penetration distance is chosen automatically by ABAQUS/Explicit for hard penalty contact, such that the effect on the time increment is minimal yet the allowed penetration is not significant in most analyses. The penetration distance will typically be an order of magnitude greater than the parent elements' elastic deformation normal to the contact interface. In purely elastic problems this penetration can affect the stress solution significantly. The user can specify a factor by which to scale the default penalty stiffnesses. This scaling may affect the automatic time incrementation. Use of a large-scale factor is likely to increase the computational time required for an analysis because of the reduction in the time increment that is necessary to maintain numerical stability.

Penalty method for other types of surface pairs is beyond the scope of this report. Please consult ABAQUS theory manual for further details [22]

# APPENDIX F

## F.1 C3D8R Element

C3D8R is a three-dimensional eight-node linear brick element with reduced integration and hourglass control. Eight-node element means that each element has 8 nodes as in Figure F.1.

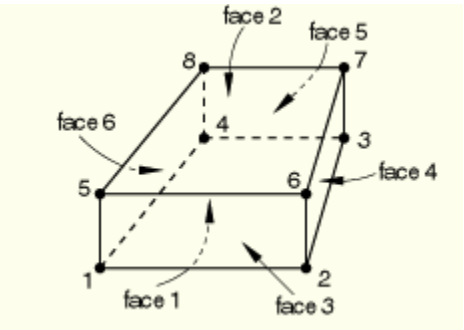


Figure F.1: C3D8R Element [22]

Reduced integration means that the order of integration is lower than that of full integration. The order of integration in this element is only one point that is located in the center of the element (centroid.) This could result in spurious zero-energy modes that destroy the FE solution.

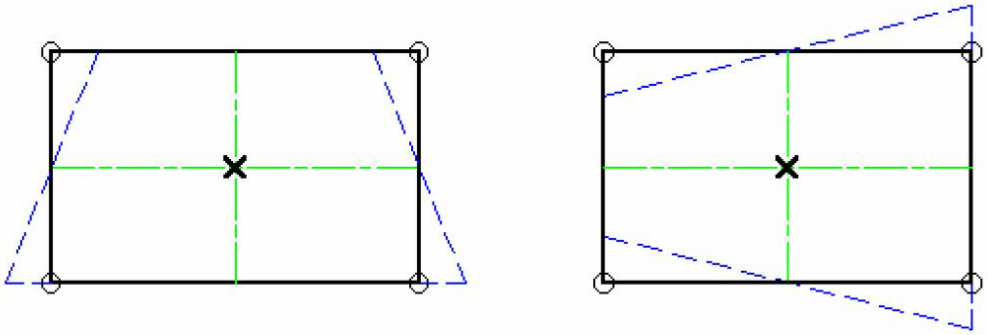

Figure F.2: Deformation (dashed lines) in element but the integration point (cross) is not moving

Figure F.2 shows deformation of a C3D8R element undergoing hourglassing. As the element deforms, neither of the dotted visualization lines change in length nor the angle between them. Therefore, all components of stress and strain at the integration point are zero. This deformation mode is a zero energy mode because no strain energy is registered by distorting the element in this manner. The element is unable to resist this type of deformation because it has no stiffness in this mode. In coarse mesh, this zero-energy mode can propagate through the mesh, producing incorrect results. If this zero-energy mode is not created, reduced integration may increase the accuracy of the FE solution, since it tends to soften the stiffness of the model [22, 79]. Hourglass control is a control of these zero-energy modes.

# APPENDIX G

## G.1 Young's modulus of hexagonal honeycombs

Figure G.1 shows the cell under compression in the Y –direction. Inclined walls tend to deform under load 'P'. Figure G.2 depicts an enlarged view of one of the inclined walls. Equilibrium requires that the component of force 'P' acting along the X-direction be zero. The moment *M* tending to bend the cell wall (which is a beam of length *l,* thickness *d*, depth *b*, and Young's modulus E) is

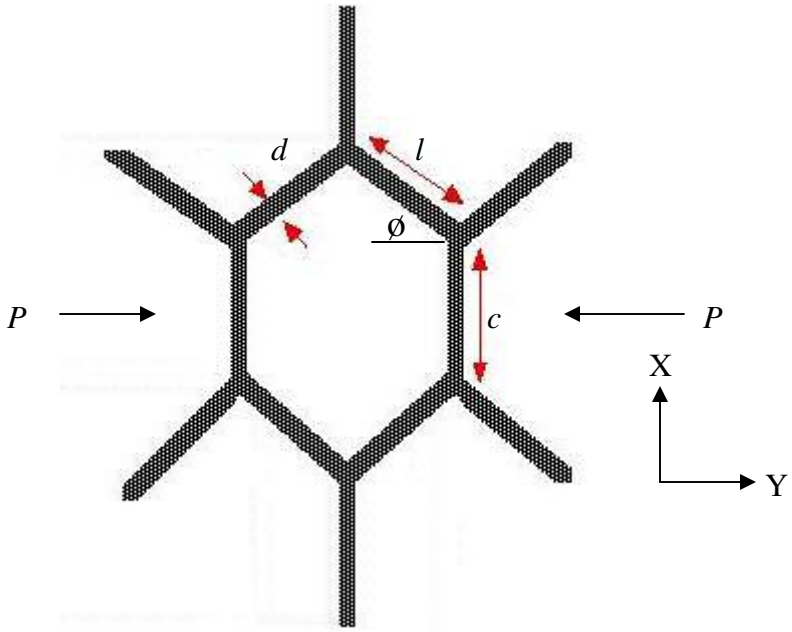


Figure G.1: Unit cell under compression in the Y direction

$$M = \frac{Plsin\phi}{2} \tag{g.1}$$

where

$$P = \sigma_p (c + l\sin\phi)b \tag{g.2}$$

From standard beam theory [80], the wall deflects by:

$$\Delta = \frac{Pl^3 \sin\phi}{12EI} \tag{g.3}$$

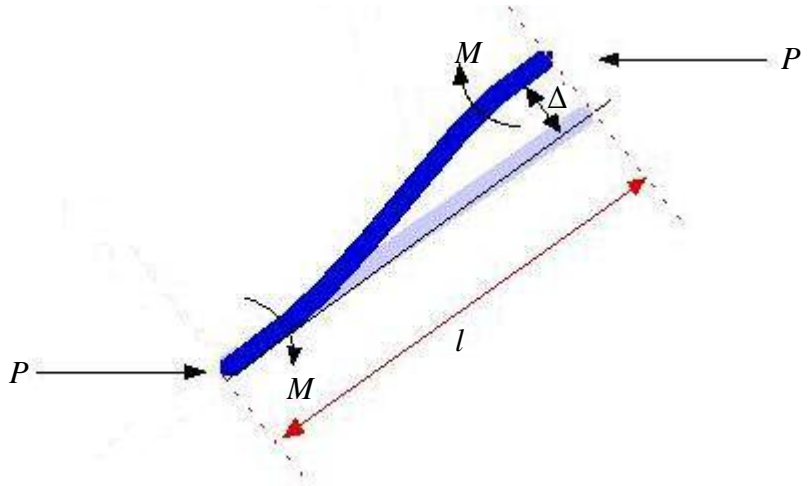


Figure G.2: Forces and bending moments on inclined walls

where E is the Young's Modulus of the material of cell wall and 'I' is the second moment of inertia of the cell wall cross-section. The strain due to the component of deflection along the Y direction is given by

$$\varepsilon_1 = \frac{\Delta \sin\phi}{l\cos\phi} = \frac{\sigma_p (c + l\sin\phi) bl^2 \sin^2\phi}{12EI\cos\phi} \tag{g.4}$$

The Young's modulus parallel to the Y direction is

$$E_1 = \frac{\sigma_p}{\varepsilon_1} = \left(\frac{d}{l}\right)^3 \frac{\cos\phi}{\left(\frac{c}{l} + \sin\phi\right)\sin^2\phi} E \tag{g.5}$$

Following the same procedure for loading in the X-direction, the strain and the modulus of elasticity are

$$\varepsilon_2 = \frac{\sigma_p' bl^4 \cos^3\theta}{12EI(c + l\sin\theta)} \tag{g.6}$$

$$E_2 = \frac{\sigma_p^{'}}{\varepsilon_2} = \left(\frac{d}{l}\right)^3 \frac{\left(\frac{c}{l} + \sin\phi\right)}{\cos^3\phi} E \qquad \text{(g.7)}$$

The Poisson's ratio is calculated by taking the negative ratio of the strains normal to, and parallel to, the loading direction. For X-direction loading

$$v_{12} = -\frac{\varepsilon_2}{\varepsilon_1} = \left( \frac{\cos^2\theta}{\left(\frac{c}{l} + \sin\theta\right)\sin\theta} \right) \qquad \text{(g.8)}$$

**G.2 Shear modulus of hexagonal honeycombs**

Figure G.3 shows a portion of honeycomb loaded in shear. Points A, B and C do not move relative to each other and shear deflection, $\Delta_s$, is totally due to the bending of beam BD and its rotation about the point B. Figure G.4 shows the forces acting on point B. Equilibrium at B gives

$$M = \frac{Pc}{4} \qquad \text{(g.9)}$$

From standard beam theory, the deflection and rotation are

$$\delta = \frac{Md^2}{6EI} \qquad \text{(g.10)}$$

$$\psi = \frac{Pcl}{24EI} \qquad \text{(g.11)}$$

The shearing deflection, $\Delta_s$, of the point D with respect to B is

$$\Delta_s = \frac{1}{2}\psi\delta + \frac{P}{3EI}\left(\frac{c}{2}\right)^3 \qquad \text{(g.12)}$$

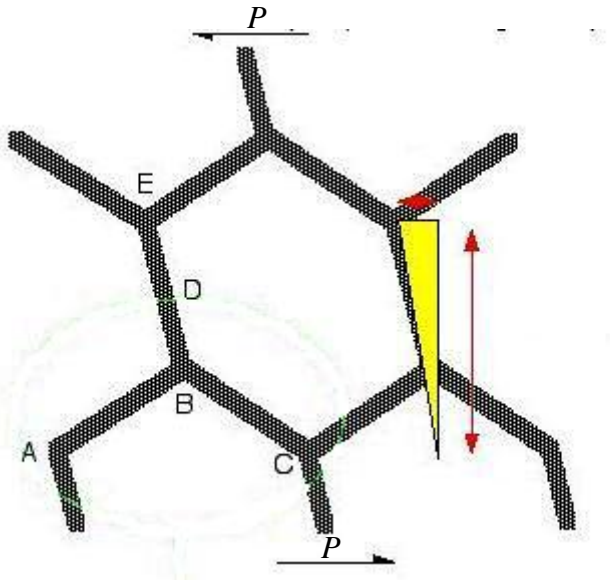


Figure G.3: Unit cell loaded in shear

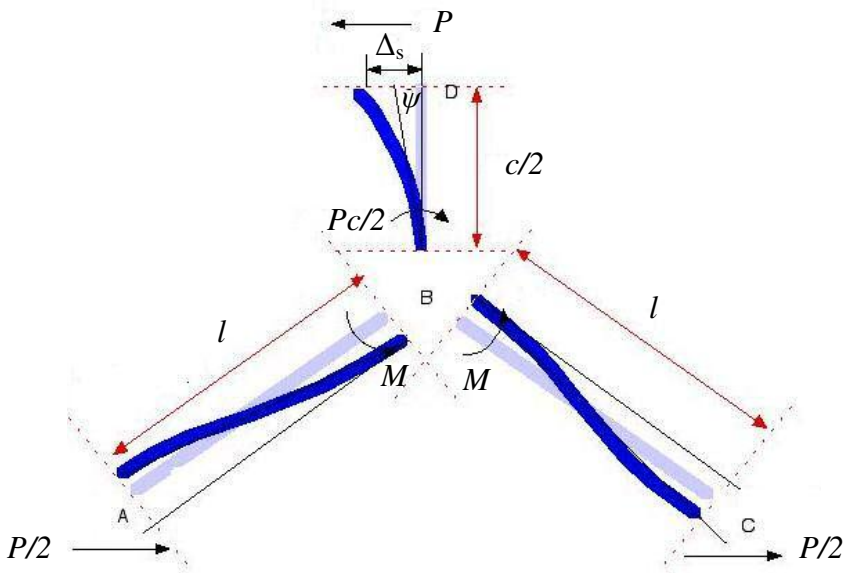


Figure G.4: Forces acting on point B

The shear strain $\gamma$ is given by:

$$\gamma = \frac{2\Delta_s}{(c + l\sin\phi)} = \frac{Pc^2}{24EI}\left(\frac{l + 2c}{c + l\sin\phi}\right) \tag{g.13}$$

The remote shear stress $\tau$ is $\frac{P}{2lb\cos\theta}$, giving the shear modulus $G_1 = \frac{\tau}{\gamma}$, or:

$$G_1 = \left(\frac{d}{l}\right)^3 \frac{\left(\frac{c}{l} + \sin\phi\right)}{\left(\frac{c}{l}\right)^2\left(1 + \frac{2c}{l}\right)\cos\phi} E \tag{g.14}$$

These expressions were derived by Gibson and Ashby [27].

## REFERENCES

[1] Alghamdi A. A., EL-Kalay A. K., Mansour T. M., and Akyurt M., "Absorption of energy by frusta," Journal of Islamic Academy of Sciences, pp.14-20, 1992.

[2] Lu G., and Yu T., "Energy Absorption of structures and materials," Woodhead Publishing Limited & CRC Press, 2003.

[3] Kojic M., and Bathe K.J., "Inelastic analysis of solids and structures" Springer-Verlag, 2005.

[4] Smith P.D., and Hetherington J.G., "Blast and ballistic loading of structures" Butterworth-Heinemann, 1994.

[5] Miyamoto Y., Kaysser W. A., Rabin B. H., Kawasaki A., and Ford R. G., "Functionally graded materials: design, processing and applications" Material technology series, 1999.

[6] Easterling K.E., Harrysson R., Gibson L. J., and Ashby M. F., "Proc. Roy. Soc.", 1982, A383, 3I.

[7] Bitzer T. "Honeycomb Technology: Materials, design, manufacturing, applications and testing" Chapman and Hall, 1st edition, 1997.

[8] Koch J.C., "The laws of bone architecture," American Journal of Anatomy, vol. 21, pp. 177-98, 1917.

[9] Martin R. B., "The effects of geometric feedback in the development of osteoporosis" Journal of Biomechanics, vol. 5, pp. 447-455, 1972.

[10] Gjelsvik A., "Bone remodeling and piezoelectricity-I," Journal of Biomechanics, vol. 6, pp. 69-77, 1973.

[11] Cowin S. C., and Hegedus D. H., "Bone remodeling I: theory of adaptive elasticity," Journal of Elasticity, vol. 6, pp. 313-26, 1976.

[12] Cowin S. C., and Bushkirk W. C. V., "Internal bone remodeling induced by medullary pin," Journal of Biomechanics, vol. 11, pp. 269-75, 1978.

[13] Przemieniecki K.S., "Theory of matrix structural analysis" McGraw-Hill, Inc. 1968

[14] Westerberg C., Thesis: "Finite element simulation of crash testing of self-piercing, rivet joint, peel specimen" 2002.

[15] Ottosen N., Petersson H., "Introduction to the finite element method" Prentice Hall, 1992.

[16] Chandrupatla T. R., and Belegundu A. D., "Introduction to finite elements in engineering" Prentice Hall, 1991.

[17] Zienkiewicz O. C., "The finite element method in Engineering Science" McGraw-Hill, Inc., 1971.

[18] John R. B., " What every engineer should know about finite element analysis" 2nd Ed. Marcel Dekker Inc., 1993.

[19] Stasa F. L., "Applied finite element analysis for engineers" Holt, Rinehart and Winston, 1985.

[20] Zhong Z. H., " Finite element procedures for contact-impact problems" Oxford Science Publications, 1993.

[21] Kalpakjian S., and Steven R. S., "Manufacturing processes for engineering materials" Prentice Hall, 4th edition, 2003.

[22] ABAQUS/Explicit, version 6.4-2, Hibbitt, Karlsson & Sorensen, Inc. 2003.

[23] Nokes L. D. M., Roberts A. M., and Knight B.H., "Use of the Gadd severity index in forensic medicine: a case study" Forensic Science International, vol. 76, pp. 85-90, 1995.

[24] Brian G. M., "Head injury criterion and the ATB" ATB User's Group 2004, pp. 1-8.

[25] Gadd C. W., "Criteria for injury potential" Impact Acceleration Stress Symposium, National Research Council Publications No. 977, National Academy of Sciences, Washington DC, pp. 141-144, 1961.

[26] Versace J., "A Review of the Severity Index", Proceedings 15th Stapp Car Crash Conference, SAE paper 710881, pp. 771-796.

[27] Gibson L. J., and Ashby M. F., "Cellular Solids; Structures and Properties" Cambridge University Press, 2nd edition 1997.

[28] Ali. M, Qamhiya A., Flugrad D., and Shakoor M., "Compact Energy Absorbing Structure: A Finite Element Study," 32nd Northeast Bioengineering Conference Proceedings, Easton, PA, USA, 12, 2006.

[29] Ali. M, Qamhiya A., Flugrad D., and Shakoor M., "Compact Energy Absorber," 18th annual ABAQUS User's Conference, Boston, MA, USA, in press, 2006.

[30] Ali. M, Qamhiya A., Flugrad D., and Shakoor M., "Compact Energy Absorbing Cellular Structure," Ninth International Conference on Structures Under Shock and Impact, New Forest, UK , in press, 2006.

[311 Sayed A. E., Jones, F. K., and Burgess I. W., "Composites", vol. 10, pp. 209-214.

[32] Papka SD., and Kyriakides S., "In-plane compressive response and crushing of honeycombs," Journal of the Mechanics and Physics of Solids, vol. 42, pp.1499-1532, 1994.

[33] Papka SD., and Kyriakides S., "Experiments and full-scale numerical simulations of In-plane crushing of a honeycombs," Acta Mater, vol. 46, pp. 2765-76, 1998.

[34] Papka SD., and Kyriakides S., "Biaxial crushing of honeycombs. Part I: Experiments," International Journal of Solids and Structures, vol. 30, pp. 4367-96, 1998.

[35] Papka SD., and Kyriakides S., "In-plane biaxial crushing of honeycombs.Part II: Analysis," International Journal of Solids and Structures, vol. 30, pp. 4397-4423, 1998.

[36] Silva M. J., Hayes W. C., and Gibson L. J., "The effects of non-periodic microstructure on the elastic properties of two-dimensional cellular solids," International Journal of Mechanical Sciences, vol. 37, pp. 1161-77, 1995.

[37] Hayes W. C., and Gibson L. J., "The effects of non-periodic microstructure and defects on the compressive strength of two-dimensional cellular solids," International Journal of Mechanical Sciences, vol. 39, pp. 549-63, 1997.

[38] Prager W., and Hodge Jr. P.G., "Theory of perfectly plastic solids," John wiley, NY. Ory,1951.

[39] Yu T. X., and Zhang L. C., "Plastic bending: Theory and applications," Series of Engineering Mechanics, vol. 2, 1996.

[40] Gere J. M., and Timoshinko P. S., "Mechanics of materials," 2nd edition, 1994.

[41] Gibson L. J., "Biomechanics of cellular solids," Journal of Biomechanics, vol. 38, pp. 377-99, 2005.

[42] Gibson L. J., "The elastic and plastic behaviour of cellular materials," Ph. D. Thesis, Engineering Department, Cambridge University, pp. 11-49, 1981.

[43] Redwood R. G., "Discussion of (DeReuntz JA & Hodge PG 1963)," ASME Journal of applied mechanics, vol. 31, pp. 357, 1964.

[44] Karagiozova D., and Yu T. X., "Plastic deformation modes of regular hexagonal honeycombs under in-plane biaxial compression," International Journal of Mechanical Sciences, vol. 46, pp.1489-1515, 2004.

[45] Binci B., and Ozcebe G., "Analysis methods for seismic evaluation of in filled reinforced concrete frames strengthened with FRPS," Dept. of civil engineering, Middle East Technical University.

[46] Hibbitt, Karlsson & Sorensen Inc., "ABAQUS/Explicit," ver. 6.4-2, 2003.

[47] Kojic M., and Bathe K. J., "Inelastic analysis of solids and structures," 2005.

[48] Khan A. S., and Haung S., "Continuum theory of plasticity"1995.

[49] Honig A., and Stronge W. J., "In-plane dynamic crushing of honeycombs. Part I: crush band initiation and wave trapping," International Journal of Mechanical Sciences, vol. 44, pp. 1665-96, 2002.

[50] Honig A., and Stronge W. J., "In-plane dynamic crushing of honeycombs. Part II: application to impact," International Journal of Mechanical Sciences, vol. 44, pp. 1697-1714, 2002.

[51] Ruan D., Lu G., Wang B., and Lu T.X. " In-plane dynamic crushing of honeycomb a finite element study" International Journal of Impact Engineering, Vol. 28, pp.161-182, 2003.

[52] Zhao H., and Gary G., "Crushing behavior of aluminum honeycombs under impact loading," International Journal of Impact Engineering, vol. 21, pp. 827-836, 1998.

[53] Reid S. R., and Reddy T. Y., "Experimental investigation of inertia effects in one-dimensional metal ring systems subjected to impact – I: Fixed ended system" International Journal of Impact Engineering, vol. 1, pp. 85-106, 1983.

[54] Reid S. R., Bell W. W., and Barr R., A., "Structural plastic shock model for one-dimensional ring systems" International Journal of Impact Engineering, vol. 1, pp. 175-191, 1983.

[55] Reid S. R., and Bell W. W., "Response of one dimensional ring systems to end impact" In: Mechanical Properties of Materials at High Rates of Strain, J. Harding edition, Inst. Phys. Conf. Series, No. 70, Bristol, pp. 471-478, 1984.

[56] Jahsman W. E., "Static and dynamic material behavior of syntactic foam" In: Mechanical Behavior of Materials under Dynamic Loads, U.S. Lindholm ed. Springer-Verlag, pp. 365-387, 1968.

[57] Zaretsky E., and Ben-dor G., "Compressive stress-strain relations and shock Hugoniot curves of flexible foams" Journal of Applied Mechanics, vol. 21, pp. 63-70, 1954.

[58] Lee E. H., and Wolf H., "Plastic wave propagation effects in high-speed testing" Journal of Applied Mechanics, vol. 17, pp. 379-386, 1951.

[59] Lee E. H., and Tupper S. J., "Analysis of plastic deformation in a steel cylinder striking a rigid target" Journal of Applied Mechanics, vol. 21, pp. 63-70, 1954.

[60] Reid S. R., Reddy T. Y., and Austin C. D, "Dynamic deformation of tube and ring systems" Proc. 5$^{th}$ Symp. Engng., Applications of Mechanics, Ottawa, pp. 301-305, 1980.

[61] Reid, S. R., and Peng C., "Dynamic Uniaxial Crushing of Wood," International Journal of Impact Engineering, vol. 19, pp. 531-570, 1997.

[62] Macaulay M., “Introduction to impact engineering” Chapman and Hall, 1987.

[63] Kolsky H., “Stress waves in solids” Clarendon Press, 1953.

[64 Isbell W. M., “Shock waves: Measuring the dynamic response of materials”, Imperial College Press, 2005.

[65] Calladine C. R., and English R. W., “Strain-rate and inertia effects in the collapse of two types of energy absorbing structure” International Journal of Mechanical Sciences”, vol. 26, pp. 689-701, 1984.

[66] Zhang, T. G., and Yu T. X., “A note on a ‘velocity sensitive’ energy absorbing structure” International Journal of Impact Engineering, vol. 8, pp. 43-51, 1989.

[67] Tam L. L., and Calladine C. R., “Inertia and strain-rate effects in a simple plate-structure under impact loading” International Journal of Impact Engineering, vol. 11, pp. 349-377, 1991.

[68] Su X. Y., Yu T. X., and Reid S. R., “Inertia-sensitive impact energy absorbing structures, Part I: Effects of inertia and elasticity” International Journal of Impact Engineering, vol. 16, pp. 651-6721995.

[69] Su X. Y., Yu T. X., and Reid S. R., “Inertia-sensitive impact energy absorbing structures, Part II: Effects of inertia and elasticity” International Journal of Impact Engineering, vol. 16, pp. 673-689, 1995.

[70] Karagiozova D., and Jones N., “A note on the inertia and strain-rate effects in the Tam and Calladine model” International Journal of Impact Engineering, vol. 16, 637-649, 1995.

[71] Khan A.S., and Huang S., “Continuum theory of plasticity” John Wiley & Sons, 1995.

[72] Chakrabarty J. “Applied plasticity” Springer, 2000.

[73] Blazynski T.Z, “Plasticity and modern metal-forming technology” Elsevier Applied Science, 1989.

[74] Hoffman O., and Sachs G., “Theory of plasticity”, McGraw-Hill, Inc., 1953.

[75] Hill R., “The mathematical theory of plasticity”Oxford, Clarendon, 1950.

[76] Sawczuk A., “Mechanics and plasticity of structures” Chichester, West Sussex, England : E. Horwood ; New York : Halsted Press, 1989.

[77] Doltsinis I., “Elements of plasticity” WIT press, 2000.

[78] Reddy J. N., “An introduction to the finite element method” McGraw-Hill, 2nd edition, 1993.

[79] White R. E., “An introduction to the finite element method with applications to non-linear problems” Wiley, 1985.

[80] Roark R. J., and Young W. C., “ Forumlas for stress and strain” 5th ed. McGraw-Hill, London, 1976.